Magnetic characteristics of metal organic low-dimensional quantum spin systems at low temperatures

Dissertation

zur Erlangung des Doktorgrades

der Naturwissenschaften

vorgelegt beim Fachbereich Physik

der Johann Wolfgang Goethe-Universität

in Frankfurt am Main

von

Katarina Remović-Langer

aus Belgrad

Frankfurt am Main 2010

(D30)

Vom Fachbereich Physik der

Johann Wolfgang Goethe-Universität als Dissertation angenommen.

Dekan: Prof. Dr. Dirk-Hermann Rischke

Gutachter: Prof. Dr. M. Lang

              Prof. Dr. W. Aßmus

Datum der Disputation: 14.01.2011

Kurzfassung

In dieser Arbeit wurden neue Klassen von niedrigdimensionalen metallisch-organischen Materialien untersucht, die es ermöglichen interessante quantenkritische Phänomene (*quantum critical phenomena, QCP)* wie die Bose-Einstein-Kondensation (*Bose-Einstein condensation, BEC)* der magnetischen Anregung in gekoppelten Spin-Dimer-Systemen, den Berezinskii-Kosterlitz-Thouless Übergang (*Berezinskii-Kosterlitz-Thouless transition,* BKT) und die Divergenz des magnetokalorischen Effekts (*magnetocaloric effect*, MCE) in Quanten-Spinsystemen beim Anlegen eines magnetischen Feldes zu beobachten.

Die Niedrigdimensionalität der untersuchten Systeme war sowohl für die theoretische Beschreibung, als auch für die experimentelle Beobachtung der Phänomene von großer Bedeutung. Aus theoretischer Sicht eröffnet die Beschäftigung mit diesen Systemen die Möglichkeit, einfache Modelle zu entwickeln, die exakt lösbar sind und erlaubt somit ein qualitatives Verständnis der magnetischen Phänomene. Von experimenteller Seite ist es von größtem Interesse, dass durch das Zusammenspiel von Niedrigdimensionalität, konkurrierenden Wechselwirkungen und starker Quantenfluktuation exotische und aufregende magnetische Phänomene (quantenkritische Phänomene) entstehen, die mit verschiedenen experimentellen Methoden untersucht werden können. Um die intrinsischen Eigenschaften der quantenkritischen Phänomene zu verstehen ist es wichtig, die Phänomene an einfachen und gut kontrollierbaren niedrigdimensionalen Modellsystemen wie ein- oder zweidimensionalen Systemen zu untersuchen.

In dieser Arbeit wurde der Fokus auf Substanzen mit moderater oder mittelstarker Austauschwechselwirkung J zwischen magnetischen Ionen (J reicht von einigen Kelvin bis zu einigen 10 Kelvin) gelegt. Dies ermöglicht experimentelle Untersuchungen im Labormaßstab. Gute Kandidaten für solche Modellsysteme sind metallisch-organische Verbindungen, bei denen die Dimensionalität und die Größe der magnetischen Wechselwirkung durch die Wahl und Anordnung der organischen Liganden eingestellt werden kann. Metallisch-organische Verbindungen sind Materialien, die aus magnetischen Zentren bestehen (intermetallische Ionen oder organische Radikale), die über Brückeneinheiten (wie Carboxylat-Gruppen, Diamin- oder Chinon-Gruppen) verbunden sind. Die Hauptbausteine der Verbindung sind das magnetische Zentrum, die Brückeneinheit und der Ligand.

Es wurden verschiedene experimentelle Techniken benutzt, um die magnetischen Eigenschaften zu bestimmen (DC- und AC-Magnetisierung, ESR-Spektroskopie, spezifische Wärme und magnetokalorischer Effekt). Durch den Einsatz dieser Techniken in einem weiten Temperatur- (0.015-300K) und magnetischen Feldbereich (0-17T) eröffnet sich die Möglichkeit, die Niedrigdimensionalität und den Phasenübergang nachzuweisen. Mittels hochauflösender AC-Magnetisierungsmessungen und des magnetokalorischen Effekts konnten detaillierte Phasendiagramme der untersuchten Systeme aufgenommen werden.

Drei verschieden Gruppen metallisch-organischer Materialien wurden untersucht:

1. Betaine,
2. Hydrochinone und,
3. Oxalat-Brücken-Systeme.

Kurzfassung

1. Betain-Verbindungen sind weit verbreitet und werden vielfältig in Medizin und Pharmazie benutzt. Diese Materialfamilie ist Bestandteil in allen biologischen Systemen und spielt eine wichtige Rolle in vielen interzellularen Prozessen. In der Physik haben diese Verbindungen großes Interesse ausgelöst nachdem bei einigen Betain-Salzen und -Addukten ferroelektrische und antiferroelektrische Ordnung bei tiefen Temperaturen entdeckt wurde. In dieser Arbeit wurden vier verschiedene Betain-Verbindungen untersucht: $((CH_3)_3NCH_2COO)_3MnMCl_4$ mit $M = Mn^{2+}$, Co^{2+}, Zn^{2+} und $((CH_3)_3NCH_2COO)_2 \cdot 3CuCl2 \cdot 2H_2O$.

$((CH_3)_3NCH_2COO)_3MnMCl_4$ mit $M = Mn^{2+}$, Co^{2+}, Zn^{2+}

Drei verschiedene Verbindungen mit Mangan(II)-, Kobalt(II)- und Zink(II)-chlorid, $3b \cdot 2MnCl_2$ (BMM), $3b \cdot MnCl_2 \cdot CoCl_2$ (BMC) und $3b \cdot MnCl_2 \cdot ZnCl_2$ (BMZ), wurden in der Gruppe für Kristallografie des Institutes für Geowissenschaften der Universität Frankfurt am Main synthetisiert. Aus struktureller Sicht sind alle drei Verbindungen isomorph und bestehen aus MnO_6-Polymerketten die über Carboxyl-Gruppen mit den Betain-Molekülen verbunden sind, während die anderen metallischen Ionen ($M = Mn^{2+}$ (Spin 5/2), Co^{2+} (Spin 3/2), Zn^{2+} (Spin 0)) leicht verzerrte tetraedrische MCl_4-Plätze besetzen, die zwischen den Ketten lokalisiert sind, und Löcher zwischen den Trimethylammonium-Gruppen der Betain-Moleküle ausfüllen. BMM, BMC und BMZ repräsentieren 1D magnetische Systeme, bei denen eine magnetische Wechselwirkung zwischen den Mn^{2+}-Ionen (Spin 5/2) innerhalb der Kette erwartet wird. Mittels Messungen an einem hochauflösenden SQUID im Temperaturbereich zwischen 2K und 300K und Feldern bis zu 5T, sowie mittels Messungen der AC-Suszeptibilität in einem $^3He/^4He$-Mischkyrostat für Temperaturen unter 2.5K bis zu 0.1K wurde die magnetische Suszeptibilität bestimmt. Die magnetischen Eigenschaften aller drei untersuchten Verbindungen BMM, BMC und BMZ bestätigten den niedrigdimensionalen Charakter und zeigten keine Phasentransformation bis zur tiefsten gemessenen Temperatur. Die magnetischen Eigenschaften aller drei Verbindungen können gut durch eine unabhängige Heisenberg-Spin-Kette beschrieben werden, bei der die Kettenglieder durch angeordnete Mn^{2+}-Ionen mit $S = 5/2$ gebildet werden. Für alle drei Verbindungen wurde eine schwache antiferromagnetische *intra*-Ketten Kopplung $J/k_B = -3K$ aus den Suszeptibilitätsmessungen bestimmt. Nur in der BMZ-Verbindung konnten die magnetischen Eigenschaften der Kette unmittelbar beobachtet werden. Im Gegensatz dazu konnten in BMM und BMC die Beiträge der Kette erst nach Abzug des paramagnetischen Anteils der isolierten Spins in den MCl_4-Tetraedern bestimmt werden.

$((CH_3)_3NCH_2COO)_2 \cdot 3CuCl_2 \cdot 2H_2O$ or $2b \cdot 3CuCl_2 \cdot 2H_2O$
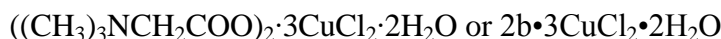
$2b \cdot 3CuCl_2 \cdot 2H_2O$ ist eine trinukleare Kupfer-Verbindung, die die Realisation eines geschichtete quasi 2D-Systems darstellt. Die geschichtete Struktur wird aufgebaut von magnetischen Cu^{2+}-Ionen, die über ein starkes Netzwerk mit O-H⋯Cl-Wasserstoff-Bindungen gekoppelt sind. Suszeptibilitätsmessungen und isothermale Magnetisierung zeigen den niedrigdimensionalen magnetischen Charakter dieses Spinsystems. Mit der Annahme eines theoretischen Modells von 2D gekoppelten Trimeren wurden die antiferromagnetische *intra*-Trimer Kopplungskonstante mit $J/k_B = -15K$ und die *inter*-Trimer Kopplungskonstante

mit $J_{a,b}/k_B$ = -4K bestimmt. Diese überraschend kleine antiferromagnetische *intra*-Trimer Kopplungskonstante für Cu^{2+}-Ionen kann verstanden werden, da die Cu-Koordinationsebenen gegeneinander gekippt sind und deswegen eine deutliche Erniedrigung der magnetischen Kopplungskonstante erwartet wird. Andererseits kann der unerwartet hohe Wert der antiferromagnetische *inter*-Trimer Kopplungskonstante unter der Annahme verstanden werden, dass die Wasserstoff-Bindungen als eine chemische und magnetische Verbindung zwischen den Spin-Trägern fungieren. Theoretische Rechnung zeigten, dass die effektive *inter*-Trimer Kopplung J_{eff} ferromagnetisch wird, wenn $J_b < J_a/2$. Das Modell legt nah, dass in einem bestimmten Bereich des Verhältnisses J_b/J_a, nicht triviale Vier-Spin-Austausch-Prozesse über die üblichen nächsten Nachbarn Austauschwechselwirkung dominieren.

Es bleibt noch zu zeigen, inwieweit das Verhältnis J_b/J_a in 2b•3CuCl$_2$•2H$_2$O durch chemische Substitution und/oder hydrostatischen Druck so beeinflusst werden kann, dass Ring-Austausch-Prozesse relevant werden.

2. Zur zweiten Gruppe der untersuchten metallisch-organischen Materialien gehören Hydrochinon-Brücken-Systeme. Im Rahmen dieser Arbeit haben G. Margraf und Kollegen vom Institut für Inorganische Chemie der Universität Frankfurt am Main neuartige Cu beinhaltende Koordinationspolymere synthetisiert, indem sie von Hydrochinon abgeleitete *Linker* als Verbindung zwischen magnetischen Cu(II)-Ionen benutzten. Indem sie verschiedene Liganden an die „Seitenarme" der Kernstruktur der Hydrochinon-Derivate brachten, schafften sie es, die magnetischen Eigenschaften des Systems zu verändern. Unter Ausnutzung dieser Strategie wurde eine ganze Familie neuartiger Spin-Dimer-Systeme mit unterschiedlichen magnetischen Eigenschaften realisiert. Das zu dieser Familie gehörende $C_{36}H_{48}Cu_2F_6N_8O_{12}S_2$ (im folgenden TK91 genannt) wurde aufgrund seiner interessanten Eigenschaften in dieser Arbeit näher untersucht.

$C_{36}H_{48}Cu_2F_6N_8O_{12}S_2$ – TK91

$C_{36}H_{48}Cu_2F_6N_8O_{12}S_2$ – TK91 stellt eine gute Realisation eines 2D gekoppelten Spin-Dimer-Systems dar. TK91 ist eine metallisch-organische Verbindung, bei der die Cu^{2+}-Ionen über Hydrochinon-Brücken verbunden sind, um Dimere zu formen. Das Dimer ist über Wasserstoffbrücken mit den benachbarten Dimeren verbunden. Messungen der DC-Suszeptibilität ergaben eine *intra*-Dimer Wechselwirkung von J/k_B = 9.4(2)K. Isothermische Magnetisierung zeigten, dass das Spinsystem nicht hinreichend mit einem isolierten Dimer-Modell beschrieben werden kann. Begleitende theoretische *ab-initio* Rechnungen ergaben, dass T91 ein 2D gekoppeltes Dimer-System mit *intra*-Dimer Wechselwirkung J_1/k_B ~ 13.4K und schwacher *inter*-Dimer Wechselwirkung J_1/k_B = 1.7K and J_2/k_B = 1.4K ist. Gleichzeitig zeigten Messungen der spezifischen Wärme eine signifikante Abweichung vom isolierten Dimer-Verhalten. Um zu überprüfen, ob TK91 überhaupt eine feldinduzierten Umwandlung durchmacht, wurde die AC-Suszeptibilität als Funktion des Feldes gemessen. Es wurde keine Hysterese bei ansteigenden und abfallenden Feld für $T \geq 0.2$K gefunden. Die Daten zeigten ein einzelnes breites Maximum um B = 6.2T. Für $T \leq 0.2$K wird das Maximum schmaler und zwei scharfe Spitzen werden auf der Flanke für niedriges und hohes Feld sichtbar. Diese Maxima wurden als obere und untere Grenze eines neuen feldinduzierten Zustands gedeutet. Die Spitze bei niedrigen Feldern beschreibt das Feld (B_{c1}) , bei dem die Spin-Lücke sich

schließt, während die Spitze bei hohen Feldern das Feld (B_{c2}) beschreibt, bei dem das System in den vollständig polarisierten Zustand übergeht. Aus diesen Daten wurde die kritischen Felder bei 0K mit B_{c1} = 5.9T und B_{c2} = 6.5T abgeschätzt.

Quanten-Monte-Carlo-Rechnungen ergaben, dass dieses System gut mit einem 2D Heisenberg-Modell schwach gekoppelter Dimere beschrieben werden kann. Das Phasendiagramm von TK91 bei niedrigen Temperaturen zeigt, dass für $50mK < T < 120mK$ der neue Zustand des Systems als kollektiv gekoppelter 2D-Dimer Zustand beschrieben werden kann, bei dem Vortizes und Antivortizes anfangen sich zu entwickeln. Unterhalb von 50mK geht das System in einen Zustand der Berezinskii-Kosterlitz-Thouless topologische Orientierung über, bei der sich Vortizes-Antivortizes-Paare formieren.

Diese Entdeckung muss noch mit weiteren experimentellen Methoden untermauert werden. Nächste Schritte wären hochauflösende Messungen der spezifische Wärme und magnetokalorische Messungen bei niedrigen Temperaturen $T < 150mK$.

3. Die dritte Gruppe der untersuchten metallisch-organischen Materialen umfasst Oxalat-Brücken-Systeme. Die Möglichkeit dieser Liganden elektronische Effekte zwischen paramagnetischen Metallionen, die mehr als 5Å voneinander entfernt sind zu vermitteln macht sie sehr attraktiv im Molekularmagnetismus. In der Literatur wurden viele eindimensionale Oxalat-Brücken-Systeme $[Cu(\mu\text{-}ox)(L)_x]$ (L = Stickstoff Donator-Ligand oder Wassermolekül) beschrieben. Die Kopplungsstärke reicht von mittleren bis zu schwacher antiferromagnetischer oder sogar ferromagnetischer Kopplung. Es wurde auch gezeigt, dass es mit Oxalat-Liganden möglich ist, zwei- und dreidimensionale Homo- und Hetero-Übergangsmetall-Netzwerke auszubilden, die eine große Vielfalt magnetischen Verhaltens zeigen (ferro-, ferri-, oder antiferromagnetische langreichweitige Ordnung). Es stellte sich heraus, dass Oxalat-Moleküle eine besonders geeignete Brückeneinheit sind, um die magnetische Wechselwirkung zu vermitteln. In dieser Arbeit wurden zwei Systeme untersucht: $Cu(ox)(pyOH) \cdot H_2O$ und $[Cu(\mu\text{-}C_2O_4)(4\text{-aminopyridine})_2(H_2O)]_n$.

$Cu(ox)(pyOH) \cdot H_2O$

$Cu(ox)(pyOH) \cdot H_2O$ mit ox-oxalate $(C_2O_4)^{2-}$ und pyOH-hydroxypyridine (C_5H_5NO) wurden von L. Wiehl am Institut für Geowissenschaften der Universität Frankfurt am Main synthetisiert. Die magnetische Cu^{2+}-Ionen ($S = \frac{1}{2}$) sind über Oxalat-Moleküle miteinander verbunden und formen Ketten entlang der b-Achse. Die Ketten sind über Sauerstoffatome miteinander verbunden und bilden quasi 2D Strukturen in der bc-Ebene. Da es keine direkte Bindung zwischen den Ketten gibt, wird erwartet, dass die *inter*-Ketten-Kopplung über die Sauerstoffatome entlang der c-Achse sehr schwach ist. Die Hydroxypyridin-Ringe ober- und unterhalb der 2D Schichten separieren die Schichten entlang der a-Achse. Die neue und wichtige strukturelle Eigenschaft dieser Materialien ist, dass die Oxalat-Moleküle innerhalb der Kette zwei verschiedene Anordnungen haben, die entlang der Kette alternieren. Aus der Gruppe der polymeren Oxalat-Ketten ist dies das erste berichtete Beispiel einer Cu^{2+}-Oxalat-Kette mit alternierender „koplanarer" und „planarer" Topologie entlang der Kette. Messungen der DC-Suszeptibilität im Temperaturbereich 2-300K und in Feldern bis zu 5T bestätigten die Niedrigdimensionalität dieses Systems. Wegen dieser speziellen strukturellen Eigenschaften wurden die magnetischen Eigenschaften im Rahmen einer alternierenden Austausch Spin-

Kette behandelt. Wird das Model einer antiferromagnetischen $S = \frac{1}{2}$ alternierenden Heisenberg-Kette benutzt, so ergeben sich die Austauschkopplungskonstante $J/k_B = -(442 \pm 5)$K und ein alternierender Parameter $\alpha = 0.13 \pm 0.06$. Auf Grund einer koplanaren Cu-Koordination war es das erste Mal, dass so eine starke antiferromagnetische Wechselwirkung in Cu^{2+} basierten polymeren Oxalat-Ketten beobachtet wurde. Diese starke antiferromagnetische Wechselwirkung klassifiziert $Cu(ox)(pyOH) \cdot H_2O$ als starke dimerisierte Spin-Kette, in der das magnetische Verhalten im Wesentlichen durch die Verschiebung von Cu^{2+}-Ionen in Bezug zur basalen Ebene der lokalen Umgebung bestimmt wird.

$$[Cu(\mu-C_2O_4)(4\text{-aminopyridine})_2(H_2O)]_n$$
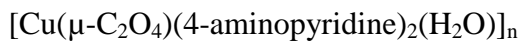
$[Cu(\mu-C_2O_4)(4\text{-aminopyridine})_2(H_2O)]_n$ Einkristalle wurden von A. V. Prokofiev vom Institüt für Physik der Universität Frankfurt am Main synthetisiert. Nach der strukturellen Analyse besteht $C_{12}H_{14}CuN_4O_5$ aus polymerischen neutralen $[Cu(\mu\text{-ox})(H_2O)(4\text{-apy})_2]$ Ketten, die entlang der c-Achse liegen. Der intra-Ketten Abstand Cu-Cu über die Oxalat-Liganden ist 6.752(1)Å und damit signifikant länger als der publizierte für dimerische und polynukleare Komplexe [< 6.0Å], aber innerhalb des Bereichs [6.5-8.1Å], der in andere Verbindungen mit Oxalat-Brücken gefunden wird. Der Oxalat-Ligand ist nicht planar, sondern die zwei CO_2-Einheiten sind um 28° um die C-C Bindung zueinander gedreht. Jedes Wassermolekül bildet zwei Wasserstoffbindungen mit der benachbarten Kette. Die O_W-H-O Wechselwirkung führt zur Ausbildung von sauerstoffgebundenen Schichten parallel zur (100) Ebenen. Von struktureller Seite sollte sich die $[Cu(\mu\text{-ox})(H_2O)(4\text{-apy})_2]_n$ Verbindung genauso wie eine $S = \frac{1}{2}$ Heisenberg-Kette verhalten. Dieses Polymer ist das erste Beispiel einer Übergangsmetal-Polymer-Struktur, bei der die Brückenbindung der Metallionen über Oxalat-Moleküle nur durch ein Sauerstoffatom realisiert wird, während das zweite frei bleibt. Wegen dieser außergewöhnlichen Konfiguration der Oxalat-Brücken wird eine moderate antiferromagnetische Austauschwechselwirkung zwischen den Cu^{2+}-Ionen innerhalb der Kette erwartet. Messung der DC-Suszeptibilität bestätigen, dass das Modell der antiferromagnetischen Heisenberg-Kette angewandt werden kann. Es wurde eine moderate antiferromagnetische intra-Ketten Austauschwechselwirkung $J/k_B = 3.2(1)$K bestimmt. ESR-Messungen bei einer Frequenz von $\nu = 56.039$GHz, einer Temperatur $T = 1.54$K und im Feld bis zu 2.5T deuten auf eine vernachlässigbare magnetische Anisotropie um die Cu^{2+}-Ionen mit g-Tensor Werten $g_b = 2.33$, $g_c = 2.08$, $g_{a*} = 2.01$ und $<g> = 2.14$ hin. Messungen der AC-Suszeptibilität bei Temperaturen bis hinunter zu 0.055K und in magnetischen Feldern bis zu 8.5T ergaben ein Sättigungsfeld um $B_s = 4.1$T. Messungen der spezifischen Wärme im Temperaturbereich 0.2-4K und in magnetischen Feldern bis zu 7.2T stützen die Schlussfolgerung, dass $[Cu(\mu\text{-ox})(H_2O)(4\text{-apy})_2]_n$ eine sehr gute Realisation einer uniformen $S = \frac{1}{2}$ antiferromagnetisch Heisenberg-Kette darstellt. Die moderate Sättigungsmagnetisierung von $B_s = 4.1$T ermöglicht es, das quantenkrische Verhalten des Systems zu untersuchen. Wird das magnetische Feld als externer Einstellparameter benutzt, konnte das System an den Quantenkritischen-Punkt gebracht werden und es wurde die vorhergesagte Divergenz des magnetokalorischen-Effekts im B-Feld induzierten Quantenkritischen-Punkt beobachtet. Dies war der erste experimentelle Nachweis des kritischen Verhalten im MCE in einer uniformen $S = \frac{1}{2}$ antiferromagnetisch Heisenberg-

Kette. MCE-Messungen zusammen mit den oben aufgeführten Messungen zeigen dass [Cu(μ-ox)(H$_2$O)(4-apy)$_2$]$_n$ ein gutes Modellsystem einer uniformen $S = \frac{1}{2}$ antiferromagnetisch Heisenberg-Kette darstellt.

Mit hochauflösenden Messungen der AC-Suszeptibilität im Nullfeld bleibt noch nachzuweisen, ob eine logarithmische Singularität für $T \rightarrow 0K$ gezeigt werden kann oder nicht. Des Weiteren ist die Existenz einer Dzyaloshinskii-Moriya-Wechselwirkung zu prüfen.

Contents

1. Introduction

The first written evidence about a 'scientific discussion' on the item magnetism dates from the ancient Greeks and is attributed to Aristotle and Thales [1]. In the 4th century BC, the earliest literary reference to magnetism (found in China) appears in a book called *Book of the Devil Valley Master*: "The lodestone makes iron come or it attracts it." [2] The earliest mention of the attraction of a needle appears in a work written between 20 and 100 AC (*Louen-heng*): "A lodestone attracts a needle."[3] The ancient Chinese scientist Shen Kuo (1031-1095) was the first person to refer to the magnetic needle compass. By 1187, Alexander Neckham was the first in Europe to describe the compass and its use for navigation. In 1269 Peter Peregrinus de Maricourt wrote the *Epistola de magnete*, the first extant treatise describing the properties of magnets. In 1600 William Gilbert published his *On the Magnet and Magnetic Bodies, and on the Great Magnet the Earth*. From his experiments, he concluded that the Earth was itself magnetic and that this was the reason compasses pointed north (previously, some believed that it was the pole star (Polaris) or a large magnetic island on the north pole that attracted the compass).

Further development in the field of magnetism, made possible after the relationship between electricity and magnetism was understood, began in 1819 with the work of Hans Christian Oersted. Several other discoveries followed, made by Ampère, Gauss, Faraday and others, where links were found between magnetism and electricity. James Clerk Maxwell synthesized and expanded links between magnetism and electricity into Maxwell's equations, unifying electricity, magnetism, and optics into the field of electromagnetism. In 1905, Einstein used these laws to promote his theory of special relativity [4], requiring that the laws held true in all inertial reference frames. Electromagnetism has continued to develop into the twentieth century, being incorporated into the more fundamental theories of gauge theory, quantum electrodynamics, electroweak theory, and finally the standard model.

In the 20th century, magnetism experienced a renaissance, one of the fields which developed and bloomed being condensed matter physics. One of the disciplines, which has attracted much interest recently, has been molecule-based magnetism. Molecule-based magnets are classes of magnetic materials that expand the materials' properties typically associated with conventional transition-metal and rare-earth-based magnets and differ from conventional magnets in one of several ways [5]:

1. Most traditional magnetic materials are comprised purely of metals (Fe, Co, Ni) or metal oxides such as CrO_2. In molecule-based magnets, the structural building blocks are molecular in nature. These building blocks are either purely organic molecules, coordination compounds or a combination of both. In this case, the unpaired electrons may reside in *d* or *f* orbitals on isolated metal atoms, but may also reside in localized *s* and *p* orbitals on the purely organic species.

2. Molecule-based magnets are prepared via different techniques and the most favorable ones are techniques which enable a chemical tailoring of the molecular building blocks and tuning of the magnetic properties. Specific materials include purely organic magnets made of organic radicals [6], mixed coordination compounds

with bridging organic radicals [7], Prussian Blue-related compounds [8], and charge-transfer complexes [9].

Molecule-based magnets derive their net magnetic moment from the cooperative effect of the spin-bearing molecular entities, and can display bulk ferromagnetic and ferrimagnetic behaviour with a true critical temperature. The first synthesis and characterization of molecule-based magnets was accomplished by Wickman and co-workers, this was a diethyldithiocarbamate-Fe(III) chloride compound [10,11].

The mechanism by which molecule-based magnets stabilize and display a net magnetic moment is quite different from that present in traditional metal and ceramic-based magnets. The magnetic moment in molecule-based magnets is typically stabilized by one or more of three main mechanisms:

1. Through space or dipolar coupling.
2. Exchange between orthogonal (non-overlapping) orbitals in the same spatial region.
3. Net moment via antiferromagnetic coupling of non-equal spin centers (ferrimagnetism).

In general, molecule-based magnets tend to be of low dimensionality. Low-dimensional materials became the impetus for the science after discovery of the first high-temperature superconductor by Bednorz and Müller in 1986 [12]. In these materials, the electronic motion predominantly occurs in two-dimensional CuO_2 layers and the compounds show effects of strong electronic correlations and magnetism in low dimensions. In order to understand the quantum correlations of such 2D systems, the theory refers first to systems with a lower dimensionality. A well-known example of a superconductor with low dimensionality is the 2D doped La_2CuO_4 [13]. Strong electronic correlations in low-dimensional quantum spin systems lead to pronounced quantum many-body effects and thus to radically different properties of matter, e.g. high-T_c superconductivity, spintronic materials, Mott insulators, spin-Peierls materials, heavy-fermion materials, quasi low-dimensional materials. A number of unusual physical phenomena, which exist in these materials, are thought to be quantum critical phenomena and to be a manifestation of the proximity to quantum-critical point. To understand the intrinsic properties of quantum criticality it is important to explore its phenomenology in simple and well-controlled model systems.

In the search for such systems, one focus is directed towards substances with moderate or intermediately strong exchange interactions J between the magnetic ions (J values ranging from a few Kelvin up to several tens of Kelvin), which enable experimental investigations to be performed in laboratory accessible conditions. Good candidates for such a type of model systems are metal–organic compounds [14-16] where the dimensionality and magnitude of the magnetic interactions can be tuned by choice and arrangement of the organic ligands [17,18]. Metal–organic compounds are materials composed of magnetic centers (intermetallic ions or organic radicals) connected via the bridging unit (such as carboxylate group, diamine group or quinon group), which is a part of the organic molecule and contains large organic ligands as spacer/connection between bridged entities [19-25]. In this building block scheme, the main components of the compound are the magnetic center, the bridging unit and the ligand. However, most flexibility is obtained by designing different low-dimensional structures to enable the combination of two different organic molecules, a large one as ligand and a small one as bridging unit.

Among the large choice of low-dimensional systems, one of the simplest quantum critical many-body systems is a linear chain of antiferromagnetically coupled $S = \frac{1}{2}$ objects. It is of great interest, since it is one of a few interacting quantum many body systems, which analytically are exactly solvable. Quantum criticality in this system is particularly interesting because it is possible to continuously tune the critical exponents by the application of a magnetic field. Over the past thirty years, a number of anisotropic materials have been found that constitute a very good realization of the one-dimensional antiferromagnetic Heisenberg model (AFHC), *e.g.*, $SrCuO_2$ [26], Sr_2CuO_3 [27,28], $KCuF_3$ [29-31], $CsCuCl_4$ [32] or $Cu(C_4H_4N_2)(NO_3)_2$ [33]. Their ordering temperatures are very small compared to that of the exchange coupling constant along the chain direction, indicating a highly one-dimensional character where *inter*-chain interactions can safely be neglected.

Isotropic $S = \frac{1}{2}$ AFHCs, where uniform nearest-neighbor exchange interactions give rise to a singlet ground state with triplet excitations, is not magnetically ordered and the excitation spectrum is gapless. The spin dynamics are not described by magnons (bosons) as is the case for 3-dimensional ordered magnets, but as massless $S = \frac{1}{2}$ spinons (fermions), which are always created in pairs. The excitation spectrum is governed by a gapless two-particle continuum restricted by a lower and an upper dispersing boundary and has experimentally been verified in several one-dimensional quantum spin chains, [30,34,35]. While some of the physical properties of the $S = \frac{1}{2}$ AFHC may be computed exactly using the Bethe ansatz, it is also very helpful to map, by using the Wigner-Jordan transformation, the spin chain onto a one-dimensional system of interacting fermions. This gives important insight into the spinon continuum, which may be viewed as the particle-hole continuum of the fermion model, and has consequences for the thermodynamic properties of the system such as the magnetization and the specific heat.

Moreover, the $S = \frac{1}{2}$ AFHC is unique due to its criticality to even small perturbations. It is therefore often referred to as a critical spin liquid, which is associated with a rich phase diagram and a modification of the low-energy excitations of isotropic spin chains. In this case, the external parameters for studying the phase diagram are pressure, frustration or the application of a magnetic field, the latter causing a substantial rearrangement of the excitation spectrum, making the soft modes incommensurate [35,36], although the spinon continuum remains gapless.

The theory of critical phenomena has quite a long history dating from the 19th century when Andrews [37] discovered a peculiar point in the *P-T* phase diagram of carbon dioxide, where the system shows critical opalescence and the properties of the liquid and of the vapor become indistinguishable. Thirty years later, Pierre Curie [38] discovered the ferromagnetic transition in iron and realized the similarities of the two phenomena. However, a quantitative theory appears with Landau [39] some years later, which corresponds to the mean-field approximation, a good qualitative description of the transitions in fluids and magnets. However, Onsager [40] and Guggenheim [41] showed that Landau's model is not quantitatively correct. In the early 60's, the modern notations were introduced by Fisher [42] and a more general framework was introduced by Kadanoff [43]. Satisfactory understanding was reached when the scaling ideas were reconsidered in the general renormalization-group (RG) framework by Wilson [44-46]. Within the new framework, it was possible to explain the

critical behaviour of most of the systems and their universal features; for instance, why fluids and uniaxial antiferromagnets behave quantitatively in an identical way at the critical point.

Magnetic insulators, composed of weakly interacting pairs (dimers) of antiferromagnetically coupled $S = ½$ spins, offer exciting possibilities for studying at finite temperature critical phenomena under well-controlled conditions [47]. The possibility of coupled-dimer systems to build versatile crystalline networks of antiferromagnetically interacting $S = ½$ spins, enlarge the chance of studing the behaviour of interacting quantum particles in 3D, 2D and very interesting and sensational effects of reduced dimensionality (dimensional crossover [48,49]). The ground state of each dimer is a spin singlet $S = 0$ separated from the excited triplet by an energy gap Δ. Due to the finite dimer-dimer interaction, the triplets can delocalize by hopping to neighbouring dimer sites, leading to a considerable dispersion of the excitations with a bandwidth defined by the *inter*-dimer coupling strength. These coupled-dimer systems have become interesting research objects due to the ability of a magnetic field to generate an ensemble of $S_z = +1$ spin-triplet states, which can be regarded as forming a gas of Bosons with hard-core repulsion that carry a magnetic moment, but no mass or charge. The repulsion is generated by the z (Ising)-component of the exchange interaction which prevents more than one triplet from being present on a single dimer site. The ground state of the system of interacting bosons thus depends on the balance between the Bosons' kinetic energy, associated with the transverse component of the *inter*-dimer exchange coupling $J_\perp$, and their repulsive interactions given by $J_{//}$. When the latter dominates, as in the 2D dimer system $SrCu_2(BO_3)_2$, the excited triplets may form commensurate superlattices, accompanied by distinct plateaus in the magnetization [50]. On the other hand, if the kinetic energy of the magnons dominates, the delocalized bosons may undergo a phase transition into a long-range magnetically-ordered state with a staggered magnetisation perpendicular to the applied field. At a critical field B_{c1}, the Zeeman split $S_z = +1$ branch intersects with the singlet ground-state, and a canted *XY* antiferromagnetic phase is observed between B_{c1} and B_{c2}, where B_{c2} denotes the saturation field. As has been suggested theoretically [51,52,53], the 3D magnetic ordering can be described as a Bose-Einstein condensation (BEC) of triplet magnetic excitations. In the BEC terminology, the excited spin-triplets correspond to massless bosons, the density of which is controlled by the strength of the external magnetic field acting as a chemical potential $\mu = g\mu_B(B-B_{c1})$. Under such conditions, BEC is expected above $B_{c1}(T)$, where $B_{c1}(T = 0)$ represents a quantum-critical point. Predicted theoretically, the critical magnetic field or the phase boundary of the long-range antiferromagnetic order follows a power-law behaviour $[B_c(T)-B_c(0)] \propto T^\phi$ with an exponent $\phi = 3/2$ for the 3D and $\phi = 1/2$ in the case of 2D BEC [54].

The concept of BEC has been applied first to the field-induced phase transition found in $TlCuCl_3$ [54]. A magnetic field-induced phase transition, indicative of a condensation of magnetic triplets, has been observed also for the ancient pigment $BaCuSi_2O_6$ [49,55,56,], where the particularly interesting aspect is the effect of dimensionality on the BEC, in particular the crossover from 3D to 2D. Another class of materials, where BEC is possible, concerns easy-plane antiferromagnets, and the complex Cs_2CuCl_4 [57,58] falls into this class of easy-plane antiferromagnets. A different situation is encountered for the related Cs_2CuBr_4 compound which has been described as an $S = ½$ quasi-2D frustrated antiferromagnet [59]. At present, for the border cases of Cs_2CuBr_4 and Cs_2CuCl_4, which reflect dominant repulsive and

kinetic energy of the magnetic excitations, no investigation exists on the interesting crossover regime.

With the help of chemical-engineering, it is possible but very hard, to make properly a combination of dimers forming multilayer system, which can be used to understand phenomena restricted to 2D. For interacting particles in 2D, long-range magnetic order and BEC are destroyed by thermal fluctuations, as was rigorously shown by Mermin and Wagner more than forty years ago [60]. Instead, according to the Berezinskii-Kosterlitz-Thouless (BKT) theory, a topological order may occur resulting from the binding of vortex-antivortex pairs [61-63]. The BKT theory has been applied to a variety of 2D phenomena in thin films, specially-designed heterogeneous systems [64-68] and trapped atomic gases [69]. However, evidence for a BKT transition in bulk magnetic materials has remained elusive [70,71].

The main objectives of the study in this thesis have been directed at a search for a new class of materials where it is possible to study magnetic field-induced quantum critical phenomena (QCP) such as BEC, BKT and magnetocaloric effect (MCE) in quantum-spin system by the application of a magnetic field. We identified a coordination polymer consisting of hydroquinone-bridged Cu^{II} ions that has been shown to represent a promising prototype material to experimentally study a field-induced QCP.

The outline of this thesis is as follows:

In Chapter 2 an introduction on the issues associated with isolated and coupled dimers systems, trimer systems and the effect of frustration is presented. In addition, the uniform and alternating $S = ½$ antiferromagnetic Heisenberg chain will be introduced. It includes a brief overview of Berezinskii-Kosterlitz-Thouless transition as well as the main magnetic features connected with BKT quantum phase transition. The quantum criticality of the $S = ½$ AFHC will be discussed and the magnetocaloric effect connected with it.

Chapter 3 provides a survey of the experimental techniques used in this work, *i.e.*, DC and AC magnetization, ESR spectroscopy, specific heat and the magnetocaloric effect.

Chapter 4 will provide the magneto-structural characterization of the investigated samples, including their crystallographic structure as well as the results of diverse magnetic measurements.

The betaine compounds with low-dimensional character will be discussed starting from the chain $S = 5/2$ compounds and ending with the coupled $S = ½$ trimer system.

An overview of the antiferromagnetic dimer systems on the basis of the hydroquinone-derived organic linker will be given. The coupled 2D dimer compound TK91 will be discussed in a frame of the magneto-structural investigations, which enable the extraction of the *intra*-dimer coupling constant. The *B-T* phase diagram established with the susceptibility measurements will be discussed in the frame of 2D BKT transition as well as the first magnetocaloric effect measurements.

The different oxalate-bridged systems, which have been studied up to now, will be presented. Special emphasis will be placed on the Cu coordination polymer which could be interpreted as a very good realization of the 1D AF Heisenberg model. Magnetocaloric measurements, which confirmed the quantum criticality expected for the $S = ½$ AFHC (now for the first time), will be discussed.

Chapter 5 will summarize the results of this work. Open issues and future projects regarding special investigated materials will be outlined.

2. Molecular Magnetism

Molecular magnetism is a multidisciplinary field connecting the area of molecular cluster physics and solid state physics. The pioneering approaches are often due to the work of physicists and some of these may even be considered to be the founding fathers of the field. On the historical scale, M. Faraday and his famous research on molecular magnetism should be mentioned, taking us back to the 19th century. Faraday studied the magnetic susceptibility of a variety of organic molecular materials [95] and discovered the effect which later became known as diamagnetism. Two significant names in the field of molecular magnetism are J. H. Van Vleck and P. W. Anderson.

The scope of molecular magnetism covers the studying of magnetic properties of isolated molecules (entities which contain one or more magnetic center) and assemblies of molecules such as molecular crystals (molecular entities which have a very weak interaction between the molecular species) and extended molecular systems (molecular entities built from molecular precursors or 'bricks').

2.1.   Dinuclear $S = \frac{1}{2}$ compounds – dimers

2.1.1. Isolated dimer systems

Dimers are molecular entities containing only two magnetic centers. The most investigated dinuclear compounds by far are $S = \frac{1}{2}$ dimers where the interaction occurs between two local doublet states. If the two $S = \frac{1}{2}$ ions interact through the bridge ligand (diamagnetic ligand), the total spin is either $S = 0$ or $S = 1$ with $E(S = 0)$, $E(S = 1)$ being the energies of these two states. Due to electrostatic reasons, these states are, in general, not equal but separated by an energy gap defined as:

$$J = E(S = 0) - E(S = 1) \tag{1}$$

J is the isotropic interaction parameter. When the state $S = 0$ is the ground state, the interaction is antiferromagnetic and $J < 0$, while for a ground state $S = 1$ the interaction is ferromagnetic, $J > 0$. In the absence of a magnetic field, the Zeeman perturbation neither affects the singlet state nor splits the components of the triplet state, as seen in Figure 1.

If the energy of the triplet state is taken into account, the magnetic susceptibility is given by:

$$\chi = \frac{2N_A g^2 \mu_B^2}{k_B T} \frac{1}{3 + e^{-J/k_B T}} \tag{2}$$

where N_A is the Avogardro number, g is the spectroscopic g-factor, k_B stands for the Boltzmann constant, μ_B for the Bohr magneton and J for the exchange interaction between the Cu(II) ions in the dimer. This expression was derived by Bleaney and Bowers [73]. For an antiferromagnetic interaction $J < 0$, the magnetic susceptibility reaches a maximum and then tends to fall to zero, when T approaches zero, where only the diamagnetic ground state is thermally populated. The maximum in the susceptibility is a signature of the antiferromagnetic *inter*-dimer interaction. The temperature T_{max} where the maximum is located is related to J as:
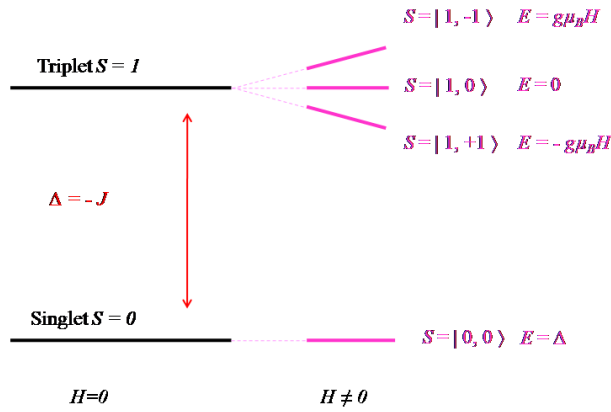
$$|J| / k_B T_{max} = 1.599 \tag{3}$$

Figure 1: Energy diagram of an isolated dimer at $H = 0$ and in a finite field.

For $J > 0$, χT is close to $\dfrac{N_A g^2 \mu_B^2}{2k_B}$ for $k_B T \gg J$. On cooling, χT increases due to the depopulation of the diamagnetic excited state in favour of the triplet ground state and tends to a plateau with $\dfrac{2N_A g^2 \mu_B^2}{3k_B}$, corresponding to the temperature range where the excited singlet state is fully depopulated. For $J < 0$, χT decreases continuously, upon cooling. The isotropic interaction is purely electrostatic in nature. However, it is often formally described by a coupling between the local spin operators $\vec{S}_1$ and $\vec{S}_2$. A phenomenological description of the isotropic interaction was introduced first by Heisenberg, and then discussed by Dirac and Van Vleck. The Hamiltonian accounting for this interaction may be written as:

$$\hat{H} = -J\vec{S}_1 \cdot \vec{S}_2 \tag{4}$$

and is generally referred to as the Heisenberg Hamiltonian.

2.1.2. Coupled dimer systems

In a weakly coupled spin $S = \frac{1}{2}$ dimer system, where the intra-dimer isotropic interaction dominates, there is a spin gap between the singlet ground state ($S = 0$) and the first excited triplet states ($S = 1$). Excitations above the singlet ground state generally can be treated as a collection of bosonic particles-magnons [54]. Holstein, Primakoff [74] and Dyson [75] showed that the magnons behave as weakly interacting quasiparticles and obey the Bose-Einstein statistics. As in each Bose gas, such a spin system may undergo Bose-Einstein condensation (BEC) but in this case of magnons[1]. An external applied magnetic field splits the excited triplet states and the lowest branch of the triplet $S \,|1, +1\rangle$ becomes the first excited state. The energy gap Δ between $S \,|1, +1\rangle$ and the singlet ground state decreases linearly with the applied field. When the external field reaches $H_g = \Delta/(g\mu_B)$, the gap in the system should "collapse" and the dimers are prompted to occupy the polarized triplet state. At finite temperature, the "collapse" of the gap will not happen at H_g but at $H = H_c > H_g$ while the thermal excitations (see Figure 2) broadening the energy branch of the triplet state. So the energy gap between the triplet and singlet energy states will have a value higher than the gap at zero temperature.
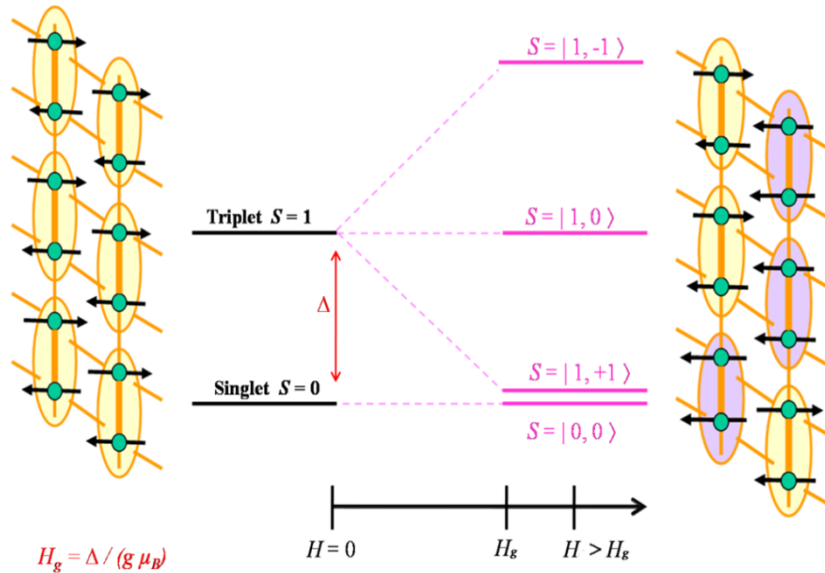

Figure 2: Schematic presentation of a coupled dimer system at $H = 0$ and in a field at and above $H_g = \Delta/(g\mu_B)$.

---

[1] In the case of atomic gas BEC is chilling of atoms of dilute vapors (typically a million or so at a time) until they enter into a single quantum state, as if all the atoms were one atom. In the solid BEC of magnons is a monolithic static magnetic alignment or long-range magnetic order in the spin system (about 10^{23} magnons participate in the condensation).

Magnetic systems composed of weakly antiferromagnetically interacting dimers with the $S = \frac{1}{2}$ spins, offer possibilities for studying finite temperature critical phenomena under well-controlled conditions. A prominent example for such phenomena is the Bose-Einstein-condensation (BEC) of magnetic triplet excitations (triplons), where one gets fascinating possibilities of exploring the behaviour of interacting quantum particles in 3D. Coupled-dimer systems enable the studying of effects of reduced dimensionality, especially those related to dimensional crossovers [49]. From this point of view, dimers with proper combination of exchange interactions can be regarded as a chemically-constructed multilayer system and may be used to understand phenomena restricted only to 2D. For interacting particles in 2D, long-range magnetic order and BEC are destroyed and not possible [60], instead a topological order may occur [61-63] known as BKT transition.

Kosterlitz-Thouless transition and the XY-model

In lattice field theory, one is interested in the phenomenon of phase transitions, where the quantity representing the length scale of relevant physics such as correlation length or inverse mass gap diverges. In different spin models, the transition between phases with and without long-range order is defined as phase transition. In models with a temperature driven phase transition these phases are distinguished by negative and positive reduced temperature ($t = 1 - T_C/T$), respectively. A conventional phase transition is then characterized by a power-law divergence in the correlation length near criticality (near $t = 0$), for the infinite volume;

$$\xi_\infty \sim |t|^{-\nu} \tag{5}$$

In two-dimensional (2D) spin models with continuous symmetry group and continuous interaction Hamiltonian, the existence of a phase with conventional long-range order is precluded by the Mermin–Wagner theorem [60]. Therefore, there is no spontaneous magnetization in $O(n)$-spin models for $n \geq 2$. Physically, the reason for this is that any long-range order which would otherwise be present is destroyed by transverse spin-wave excitations, i.e the Goldstone modes in two dimensions.

In the systems with *XY*-symmetry, order parameter functions at low temperature change algebraically rather than exponentially, as they would in completely disordered phase. Therefore, posing the question of whether change from an algebraically ordered low-temperature phase to an exponentially disordered high-temperature phase in a *XY*-model can be considered as transition, i.e., a transition from quasi-long-range order to disorder. Applying the renormalization group methods to the non-linear σ–model predicts that transition temperature tends to zero as $d \to 2$ for all $n > 2$, thus all these models are disordered in two-dimensions except at $T = 0$K. The non-linear σ–model gives an intermediate result for the transition temperature of the two-component *XY*-model.

In a *d*-dimensional theory, if the order parameter lies in a space G, then topological defects of dimension p can occur if the homotopy group $\pi_{d-p-1}(G)$ is non trivial [76]. Thus the

two dimensional $O(2)$-model can have point defects or vortices. Vortices are a special class of defects called topological defects. A topological defect (topological soliton) is a solution of a system of partial differential equations or of a quantum field theory that can be proven to exist because the boundary conditions cause the existence of homotopically distinct solution. Topological defects are stable against small perturbations and cannot decay or be undone or be de-tangled, because there is no continuous transformation that will map them (homotopically) to a uniform or "trivial" solution. Topological defects have different names depending on the symmetry that is broken in the particular system; in the superfluid helium and *XY*-models they are called vortices, in periodic crystals, dislocations and in nematic liquid crystals, disclinations. Topological defects are believed to drive the phase transition in condensed matter physics. Therefore, in 2D models, topological long-range order can exist and the pivotal role in the transition from quasi-ordered low-temperature phases to a high-temperature disordered phase is played by topological defects. Topological defects are generally characterized with two regions:

(1) core region (a point or a line) where the order is destroyed
(2) far-field region where an elastic variable changes slowly in space.

A vortex is characterized with integer number k called *winding number* or *strength* of the vortex. The $k = 1$ vortex state is a topologically and physically stable state even though it has much higher energy than the ground state because there is no path to the ground state that is not energetically costly. A single vortex has energetically costly elastic distortion far from its core. On the other hand, pairs of vortices with opposite winding number in a far-field configuration topologically are equivalent to the uniform state. Vortex pairs represent important excitations from the ground state of 2D systems with *XY*-symmetry.

The existence of topological point defects (vortices) in a 2D *XY*-system, suggests that maybe thermally excited vortices could be responsible for a transition from algebraically ordered phase to exponentially disordered phase in 2D *XY*-systems.

Kosterlitz and Thouless used approximate renormalization group methods to show the existence of a phase transition driven by the binding of vortices in the two dimensional *XY*–model (which is also called the $O(2)$ non-linear σ-model or the two-component Heisenberg model) at finite nonzero temperature [61, 63, 77]:

$$T_C = \frac{\pi Y}{2} \tag{6}$$

where Y is the fully renormalized helicity modulus or spin-stiffness which is related to the fluctuations in the total winding number [78]. They also showed that this is a phase transition of infinite order.

The scenario proposed by Berezinskii [61] and Kosterlitz and Thouless [77] (BKT) demonstrates that at temperatures above some critical value ($T > T_C$), the vortices and antivortices are unbounded and serve to disorder the system (disordered phase is a result of the formation of vortices). The temperature at which the BKT transition occurs (T_C) is in fact that at which vortex generation becomes thermodynamically favorable. For the vortex

formation, the vortex chemical potential is a relevant variable, and for the simple square lattice with the spacing a, r_0 a cutoff of the order of the lattice spacing a and unit strength of the vortex, it has a form:

$$\mu = -2\pi J \ln \frac{r_0}{a} \tag{7}$$

Decreasing the temperature causes the vortices and antivortices to bind in pairs of zero total vorticity, thereby decreasing their relevance as dynamical degrees of freedom. The model remains critical (thermodynamic functions diverge) for all $T < T_C$ and the critical exponents are dependent on temperature. In terms of the reduced temperature t, the leading critical behaviour of the correlation length, susceptibility and the specific heat is given as:

$$\xi_\infty \sim e^{bt^{-\nu}} \tag{8}$$

$$\chi_\infty(\beta) \sim \xi_\infty^{\tilde{\gamma}} \tag{9}$$

$$C_\infty(\beta) \sim \xi_\infty^{\tilde{\alpha}} + const. \tag{10}$$

and for $t \to 0^+$, $\nu = 1/2$, $\tilde{\gamma} = \frac{7}{4}$, and $\tilde{\alpha} = -2$.

The exponential scaling behaviour of (8) is referred to as essential scaling to distinguish it from the power-law behaviour of (5). Thus the 'KT scenario' means a phase transition:

(i) which is driven by a vortex binding mechanism and
(ii) exhibiting essential scaling behaviour.

Field-induced *XY* behaviour in the two-dimensional quantum Heisenberg antiferromagnet

Field-induced effects in low-dimensional antiferromagnets have been the subject of interest in recent years; on the theoretical side, the possibility of inducing novel magnetic phases via application of a strong field has been pointed out [79, 80] and on the experimental side, fields of very high intensity have become available.

When the two-dimensional quantum Heisenberg antiferromagnet (2D QHAF) in a uniform magnetic field was considered it was found that the rich phenomenology [81] of the model is ruled by the interplay between the exchange and the Zeeman terms. The applied field breaks the $O(3)$ symmetry of the isotropic model and induces a uniform alignment in the z direction; such an alignment frustrates the antiferromagnetic order along z but does not clash with anti-alignment on the xy-plane, where $O(2)$ symmetry stays untouched. Hence for infinitesimally small fields, one expects the spins to lie anti-aligned on the xy plane, and progressively cant out of it as H is increased. Saturation occurs at the critical value H_C, above which the ground state displays uniform ferromagnetic alignment along the z direction. In the range $H < H_C$ one may also expect thermal fluctuations of the z spin components to be smaller

for a larger field, while no such reduction should occur as far as the *x* and *y* components are concerned. From the above picture, it is clear that the model shares essential features with the easy-plane 2D QHAF [82].

The quantum Monte Carlo calculations [82] of the $S = \frac{1}{2}$ two-dimensional QHAF on the square lattice in an arbitrary uniform field, indicate that an arbitrarily small field is able to induce a BKT transition and an extended *XY* phase above it. The field-induced *XY* behaviour becomes more and more marked for increasing fields, while for strong fields the antiferromagnetic behaviour along the field axis is nearly washed out, so that the system behaves as a planar rotator model with antiferromagnetism surviving in the orthogonal plane only; the BKT critical temperature vanishes as the field reaches the saturation value H_C and the effective rotator length goes to zero. The model in a moderately strong field represents an ideal realization of the *XY* model: the *XY* behaviour can be detected by measuring standard non-critical quantities, such as the specific heat or the induced magnetization; this opens the possibility for an experimental realization of the *XY* model in purely magnetic systems, and for a systematic investigation of the dynamics of vortex/antivortex excitations.

Helicity modulus of the quantum *XY*-model

The **spin-stiffness** or **spin rigidity** or helicity modulus or the "superfluid density " (for bosons the superfluid density is proportional to the spin-stiffness) is a constant which represents the change in the ground state energy of a spin system as a result of introducing a slow in plane twist of the spins. The importance of this constant is in its use as an indicator of quantum phase transitions.

Mathematically it can be defined by the following equation:

$$Y = \frac{\partial^2}{\partial \theta^2} \frac{E_0(\theta)}{N}\bigg|_{\theta=0} \tag{11}$$

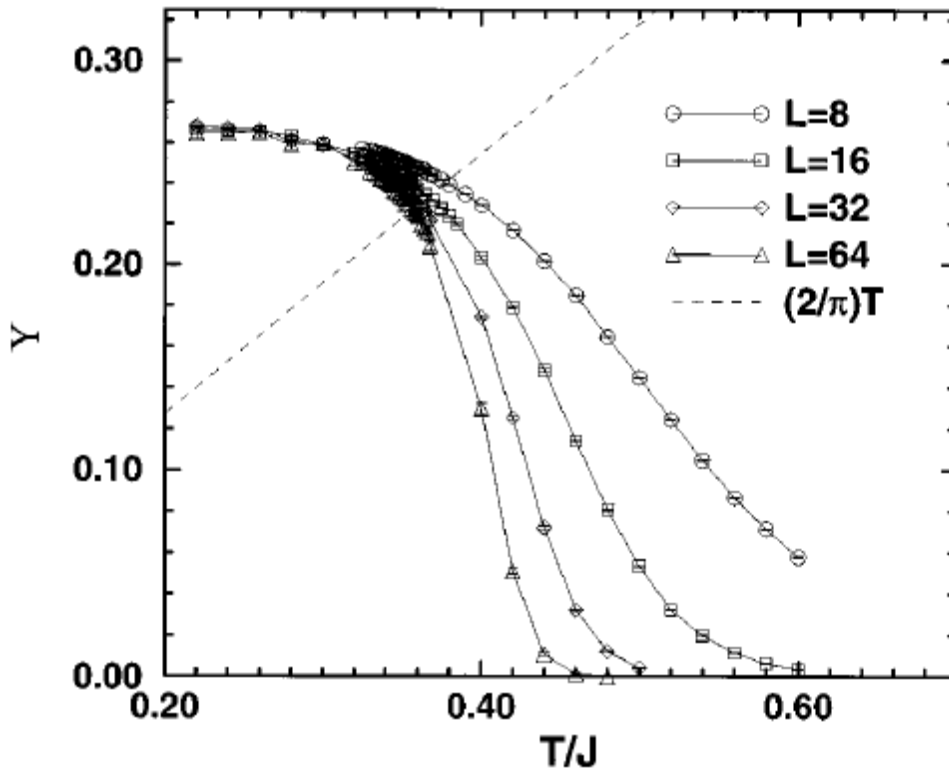where E_0 is the ground state energy, θ is the twisting angle, and *N* is the number of lattice sites.

Figure 3: The helicity modulus as a function of temperature, the universal jump is expected at the point where $Y = (2\pi)/T_C$. Figure is taken from [85].

The Kosterlitz renormalization-group equation [77] leads to the prediction that the Y jumps from the value $(2\pi)/T_C$ to zero at the critical temperature [83]. This quantity corresponds to the superfluid density when the model is regarded as a Boson system with hard cores. According to the quantum Monte Carlo method, the helicity modulus is related to the fluctuation in the total winding number-W of world lines by the following equation [84]:

$$Y = (T/2)\langle W^2 \rangle \tag{12}$$

The helicity modulus exhibits the universal jump at the critical temperature, see Figure 3. Figure 3 demonstrates results from Monte Carlo simulations of Y for the different system sizes. The solid line is $(2\pi)/T$ and the cross-section with simulation curves define the critical temperature T_C.

2.2. Trinuclear $S = ½$ compounds – trimers

Trinuclear compounds are molecular species, consisting of building blocks which contain three magnetic centers. The macroscopic nature of the interaction between adjacent centers is the same as in dinuclear compounds but the presence of more than two spin carriers may lead to a different magnetic behaviour. There are two aspects of interest in the building scheme of trimer systems:

1. irregular spin-state structure
2. spin frustration

which are not encountered in dimer compounds.

2.2.1. Symmetrical trimers

Symmetrical trimers are trinuclear compounds which can be presented either as a triangular or a linear trinuclear species (see Figure 4). In such compounds, the magnetic centers can be homo or hetero nuclear. The simplest situation is the case of the homo-nuclear compound.
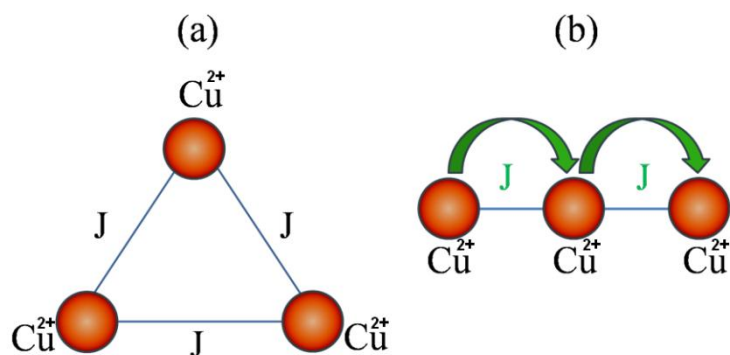
Figure 4: Basic structures of homo-nuclear symmetrical trimer compounds, (a) triangular structure and (b) linear structure.

The triangular lattice is the simplest realization of a geometrically frustrated lattice. Antiferromagnetic spin systems on geometrically frustrated lattice show many unusual behaviours of magnetic and thermal properties, and the spin frustration plays an essential role in several physical fields such as magnetism [86], superconductivity [87], and even in the field of neural networks [88]. The interplay between the geometric frustration and quantum fluctuations gives rise to a number of intriguing phenomena, including the macroscopic

degeneracy of the ground state [86], the quantized plateaux in magnetization curves [89] and the double-peak structure in the specific heat [90], etc.

The spin Hamiltonian for isolated trimers with a linear geometrical structure, a uniform isotropic Heisenberg *intra*-trimer exchange interaction J and an isotropic g−factor is given by:

$$\hat{H} = -J(\hat{S}_1\hat{S}_2 + \hat{S}_2\hat{S}_3) - g\mu_B\vec{H}(\hat{S}_1 + \hat{S}_2 + \hat{S}_3) \tag{13}$$

This Hamiltonian corresponds to the geometrical structure shown in the Figure 5.
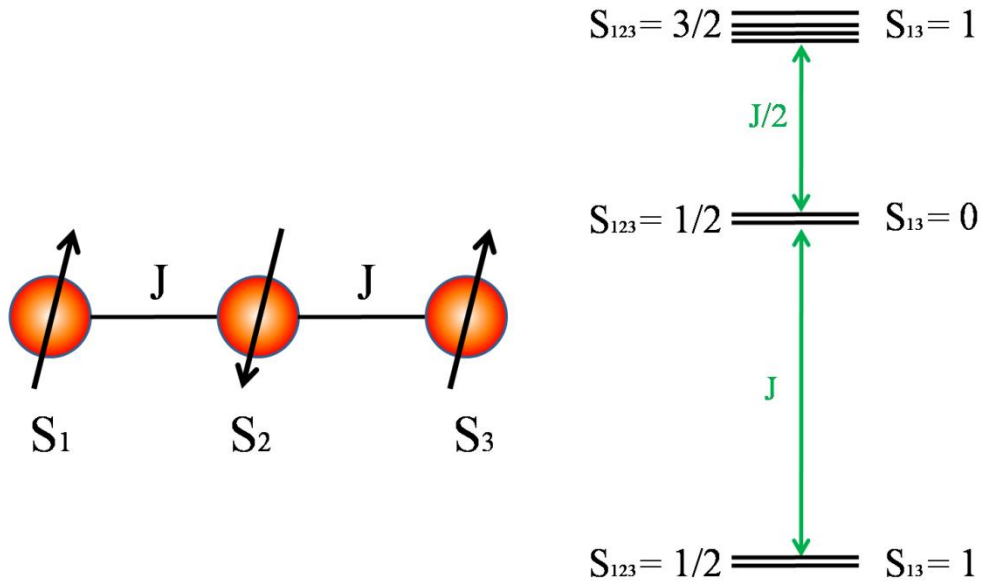
Figure 5: The linear trimer model with uniform Heisenberg inter-trimer interaction J, the spin states of the isolated trimers are labeled as $S = S_{123}$. S_{123} is the total spin $\hat{S} = \hat{S}_1 + \hat{S}_2 + \hat{S}_3$ and $\hat{S}_{13} = \hat{S}_1 + \hat{S}_3$ is an intermediate coupling number.

The relative energies in zero field for this spin system are given as:

$$E(S, S') = \frac{J}{2}S(S + 1) + \frac{J}{2}S'(S' + 1) \tag{14}$$

where $S' = S_1 + S_3$ and $S = S' + S_2$. The trimer has a simple energy spectrum which consists of doublet ground state $E\left(\frac{1}{2}, 0\right) = -J$, with $S = \frac{1}{2}$ and energy $-J$ (in zero field) where the spin-down state is given by $(|\uparrow\downarrow\downarrow> - 2|\downarrow\uparrow\downarrow> + |\downarrow\downarrow\uparrow>)/\sqrt{6}$ (see Figure 5). The first excited state (doublet) $E\left(\frac{1}{2}, 1\right) = 0$ has zero energy and also $S = \frac{1}{2}$ with the spin-down state given by $(|\uparrow\downarrow\downarrow> - |\downarrow\downarrow\uparrow>)/\sqrt{2}$. The highest energy state (quartet) $E(3/2, 1) = J/2$ has $S = 3/2$ and energy $J/2$. The spin states of the isolated trimer are labeled according to the eigenvalues of the square of the total operator $\hat{S}_{123} = \hat{S}_1 + \hat{S}_2 + \hat{S}_3$ and an intermediate coupling quantum number

$\hat{S}_{13} = \hat{S}_1 + \hat{S}_3$. From the partition function the magnetic susceptibility can be derived in a straightforward way yielding Equation (15), where $x = \exp(-J/2k_BT)$:

$$\chi_{mol} = \frac{N_A\mu_B^2 g^2}{4Tk_B} \frac{1 + x^2 + 10x^3}{1 + x^2 + 2x^3}$$

(15)

The magnetization of the isolated linear trimer can be written, where $h = g\mu_B/k_B$:

$$M(T,h) = N_A\mu_B g \frac{1}{2} \frac{(1 + x^2 + x^3)s_1 + 3x^3 s_3}{(1 + x^2 + x^3)c_1 + x^3 c_3}$$

$$c_1 = \cosh(h/2T)$$
$$c_3 = \cosh(3h/2T)$$
$$s_1 = \sinh(h/2T)$$
$$s_3 = \sinh(3h/2T)$$

(16)

In the limit $J\to\infty$ or $T << J/k_B$, that is, $x\to0$, the trimer is locked into a $S = \frac{1}{2}$ state and $M(T,h)$ reduces to the $S = \frac{1}{2}$ Brillouin function. Conversely, for vanishing exchange coupling J or $T >> J/k_B$, that is, $x\to1$, the spins of the trimer are independent and $M(T,h)$ is 3 times the $S = \frac{1}{2}$ Brillouin function.

2.2.2. Competing interaction and frustration

The frustration was initially introduced to describe a system's inability to simultaneously minimize the competing interaction energy between its components [91]. Frustrated systems were discovered and have been studied for more than 50 years, the famous example being the Ising spins on an antiferromagnetic triangular network studied by G. H. Wannier in 1950. A renewed and greater interest in such systems arose almost two decades later in the context of spin glasses and spatially modulated magnetic superstructures.

In general, frustration is caused either by competing interactions due to site disorder (the Villain model [92]) or by lattice structure such as in the triangular, face-centered cubic (fcc), hexagonal-closed-packed, tetrahedron, pyrochlore and kagome lattice with antiferromagnetic interaction [93]. So frustration can be divided into two categories:

(1) the spin glass, phenomenon caused by disorder in the structure and frustration in the spins

(2) the geometrical frustration, phenomenon caused by an ordered lattice structure and frustration of spin.

The frustration of a spin glass can be understood within the framework of the RKKY model, in which the interaction property, either ferromagnetic or antiferromagnetic, is dependent on the distance of the two magnetic ions. Due to the lattice disorder in the spin glass, one spin of interest and its nearest neighbors could be at varying distances and have a different interaction property, thus leading to a different preferred alignment of the spin.

Geometrical frustration is a phenomenon in which the geometrical properties of the atomic lattice forbid the existence of a unique ground state; resulting in nonzero residual entropy (an example of a geometrically frustrated material is ordinary water ice, which has residual entropy of around 3.4 J/Kmol). One simple example is shown in Figure 6 where one of the interactions is different and presented with J'. Three magnetic ions with Ising anisotropy reside on the corner of a triangle with antiferromagnetic interactions between them. Once the first two spins are aligned anti-parallel, the third one is frustrated because its two orientations (up or down) give the same energy-the third spin cannot simultaneously minimize its interactions with either of the other two. Thus the ground state is twofold degenerate (see Figure 6).
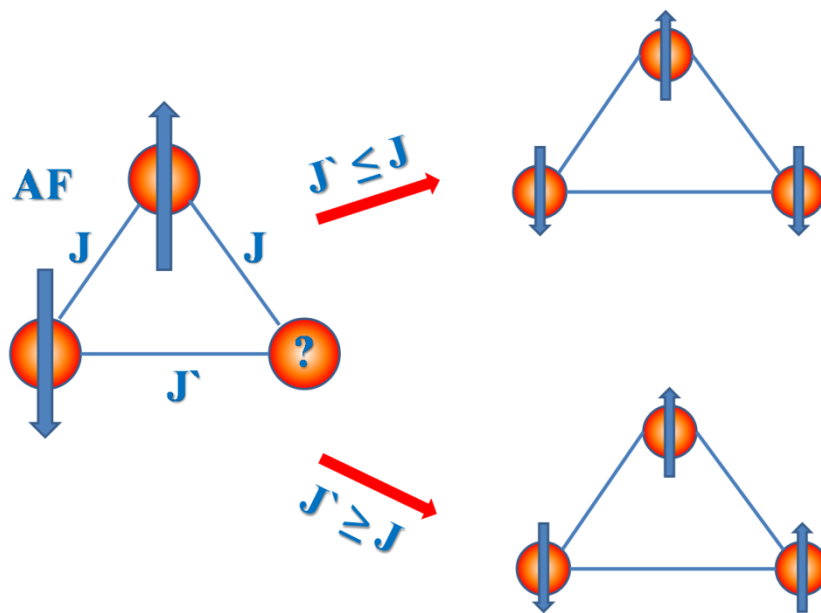
Figure 6: Antiferromagnetically interacting Ising spins in a triangular arrangement.

2.3. Quantum-spin Heisenberg chains

One-dimensional (1D) magnetic compounds first attracted interest after it was found that they provide good examples for testing models which could not be solved in higher dimension [81]. In the 1970's, several families of magnetic compounds with linear chain structure were discovered and analyzed with models that had been developed a decade earlier [94]. In the 1980's, a major discovery was bimetallic chain compounds with alternating spin carriers because these introduced a new concept in 1D magnetism , the so-called 1D ferrimagnetism. The search for novel magnetic materials led to exotic systems such as ladder-like chains, triangle-based chains, spin-frustrated double chains, topological 1D ferrimagnets, and spin-frustrated topological 1D ferrimagnets.

Due to the possible anisotropies of the exchange interaction, theoretical models consider the boundary cases of the so-called *Heisenberg* and *Ising interaction*. Heisenberg-isotropic interaction refers to fully isotropic spin Hamiltonian of the form:

$$H(\hat{S}, \hat{S}') = J\hat{S} \cdot \hat{S}' \tag{17}$$

Positive *J* value corresponds to an AF interaction. The Equation (17) does not include all types of isotropic coupling, for instance, the isotropic biquadratic spin interaction (magnon-phonon interaction) [95].

The Ising interaction is a special case of the more general anisotropic coupling which has a spin Hamiltonian of the form:

$$H(\hat{S}, \hat{S}') = (J_x S_x S_x' + J_y S_y S_y' + J_z S_z S_z') \tag{18}$$

where J_x, J_y and J_z are the components of the exchange coupling between the *x*, *y* and *z*-components of the spins, respectively.

Apart from the Ising coupling, analytical solutions are possible when the spin is treated in the classical approximation. There is no exact solution for the infinite chain, even in the simple F or AF case, except for the ground state energy of the AF *S* = ½ chain [96].

The simplest case is a linear chain with Heisenberg coupling between nearest-neighbor quantum spins without local anisotropy. The general method for obtaining a solution is to use an extrapolation procedure taken from the exact results for the different finite length chains. The pioneering work in this field was performed by Bonner & Fisher where they discussed the problem of the uniform *S* = ½ chain, with exchange anisotropy ($J_x = J_y \neq J_z$) and with either F or AF coupling [97]. They considered open chains in order to evaluate finite size effects on the magnetic properties. Their work was expanded by Weng who experimented with larger spin values [98] to the AF Heisenberg chains and later by Blöte [99] who took into account the exchange and single-ion anisotropy. Duffy & Barr introduced alternating exchange interaction in the AF *S* = ½ Heisenberg chain [100].

2.3.1. Uniform antiferromagnetic $S = ½$ Heisenberg chain

The spin $S = ½$ antiferromagnetic (AF) uniform Heisenberg chain has a long and distinguished history in condensed matter physics, because it exhibits unusual static and dynamic properties unique to a one-dimensional spin system. The Hamiltonian of this system is:

$$H = J\sum_i S_i S_{i+j} \tag{19}$$

J > 0 is AF exchange interaction

The $S = ½$ Heisenberg chain is known to be exactly solvable [96], i.e., all eigenvalues can be obtained from the so-called Bethe ansatz equations. The direct method for evaluating the partition function was given in [101, 102] and is known as "thermodynamic Bethe ansatz" (BTA), but did not allow high accuracy calculations, especially in the low-temperature region.

The possibility for calculating the physical properties of the $S = ½$ Heisenberg chain has enabled the path integral formulation of the transfer matrix treatment of quantum systems [103]. On the basis of a Bethe ansatz solution to the transfer matrix, Eggert, Affleck and Takahashi in 1994 obtained numerically exact results for the magnetic susceptibility $\chi(T)$ down to much lower temperatures than have ever been achieved before and compared this result with low-temperature results from conformal theory [104].

Thermodynamic Properties of the Uniform $S = ½$ AFHC

The thermodynamic bulk properties as magnetic spin susceptibility χ, magnetization M and specific heat C can be obtained from the free energy F and the entropy S as function of magnetic field H and temperature T. Statistical mechanics relations were used for this:

$$\chi = \left(\frac{\partial M}{\partial H}\right)_T = -\frac{1}{N}\left(\frac{\partial^2 F}{\partial H^2}\right)_T \tag{20}$$

$$M = -\frac{1}{N}\left(\frac{\partial F}{\partial H}\right)_T \tag{21}$$

$$C = T\left(\frac{\partial S}{\partial T}\right)_H = T\left(\frac{\partial^2 F}{\partial T^2}\right)_H \tag{22}$$

Magnetic Susceptibility of the Uniform $S = ½$ AFHC

The magnetic susceptibility χ of the uniform $S = ½$ AFHC was calculated for the first time by Bonner and Fisher in 1964 [97]. Their first results referred to the chains with ≤ 11

spins and were done for $T \geq 0.4J/k_B$. They extended their results by extrapolation to $T = 0K$. A first exact solution for $\chi(T)$ was obtained by Eggert, Affleck and Takahashi in 1994 using Bethe ansatz. They found $\chi(T \rightarrow 0K)$ in the form of "logarithmic corrections" where the T_0 temperature is not predicted by the field theory. Lukyanov has done an exact theory for $\chi(T)$ at low-T, including the value for the T_0 [105].

The uniform $S = ½$ AFHC has no spin gap and in the $T \rightarrow 0K$ limit, the magnetic susceptibility $\chi(T)$ has a finite value in an external magnetic field less than the saturation field ($H_{sat} = 2J/g\mu_B$), see Figure 7. At zero temperature and in zero external field, the spin susceptibility of the uniform $S = 1/2$ AFHC is $\chi(0) = N_A g^2 \mu_B^2/(\pi^2 J)$. At $H = H_{sat}$ (red curve) the susceptibility diverges at $T = 0K$ and for $H > H_{sat}$ the susceptibility drops to zero at $T = 0$ (see Ref. [106]). For higher temperatures and for fields lower than the saturation field, the spin susceptibility $\chi(T)$ exhibits a broad maximum χ^{max} at a temperature T^{max}. In zero field one finds [107]:

$$\chi^{max} T^{max} = 0.094158 \frac{N_A g^2 \mu_B^2}{k_B} \tag{23}$$

In the limit $H \rightarrow 0$ the relation given by Equation (23) is a good initial test of whether the $S = ½$ AFHC model might be used for a particular magnetic system. For the external field $H < H_{sat}$, the maximum of $\chi(T)$ shifts to lower temperatures, becomes narrow and grows in height and eventually for $H = H_{sat}$ endues into a divergence for $T \rightarrow 0K$.
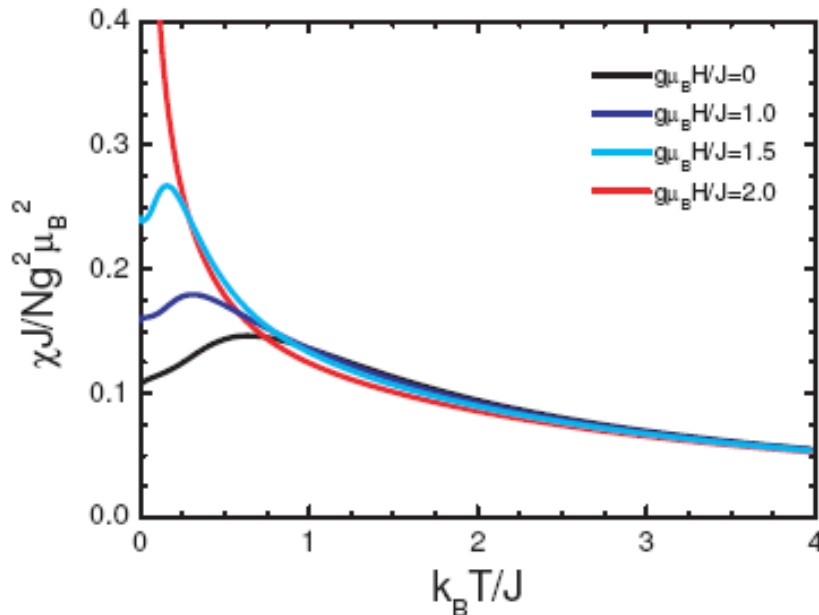
Figure 7: Magnetic susceptibility χ versus temperature T for the uniform $S = ½$ AFHC for various external magnetic fields as calculated by Klümper [106]. The figure is taken from Ref. [108].

Eggert *et al.* [104] derived an expression for the temperature dependence of $\chi(T)$ by using the Bethe ansatz. This result differs significantly from the Bonner-Fisher result for $T < 0.25J/k_B$. The result of Eggert *et al.* is:

$$\chi(T) = g^2 \left(\frac{N_A \mu_B^2}{4 k_B}\right) F\left(\frac{J}{k_B T}\right) \frac{1}{T}$$

(24)

where $F(x = J/k_B T)$ is an empirical rational function. Feyerherm *et al.* [109] found:

$$F(x) = \frac{1 + 0.08516x + 0.23351x^2}{1 + 0.73382x + 0.1369x^2 + 0.53568x^3}$$

(25)

for $T > 0.05J/k_B$. Note that $F(x) \rightarrow 1$ for $T \rightarrow \infty$. The theoretical result of Eggert *et al.* and the Bonner−Fisher result coincide for $T > 0.5J/k_B$. As $T \rightarrow 0K$, a simple expansion of the spin susceptibility in the variable $x = J/k_B T$ fails. Such a nonanalytic behaviour in x can be viewed as a consequence of the strong correlations between the quasi-particles - spinons, *i.e.*, the elementary excitations of the system are not free. Hence, serial expansion of the spin susceptibility has to be supplemented by a term $1/\log(x)$.

Eggert *et al.* obtained the magnetic susceptibility data $\chi(T)$ using Bethe ansatz till $T \sim 0.003J/k_B$. Their results, in a recently calculated more accurate form [107], are shown in Figure 8. One should note that after passing the maximum χ^{max} at a temperature T^{max}, the slope of χ starts to increase below the inflection point $T^{infl} \approx 0.087J/k_B$, approaching infinity as $T \rightarrow 0K$. For $T < 0.1J/k_B$ the magnetic susceptibility is:

$$\chi(T \rightarrow 0) = \chi(0)\left(1 + \frac{1}{2 \ln\frac{T_0}{T}}\right)$$

(26)

with $\chi(0) = N_A g^2 \mu_B^2/(\pi^2 J)$ and $T_0 \approx 7.7J/k_B$, and as one can see is mainly dominated by the logarithmic corrections.

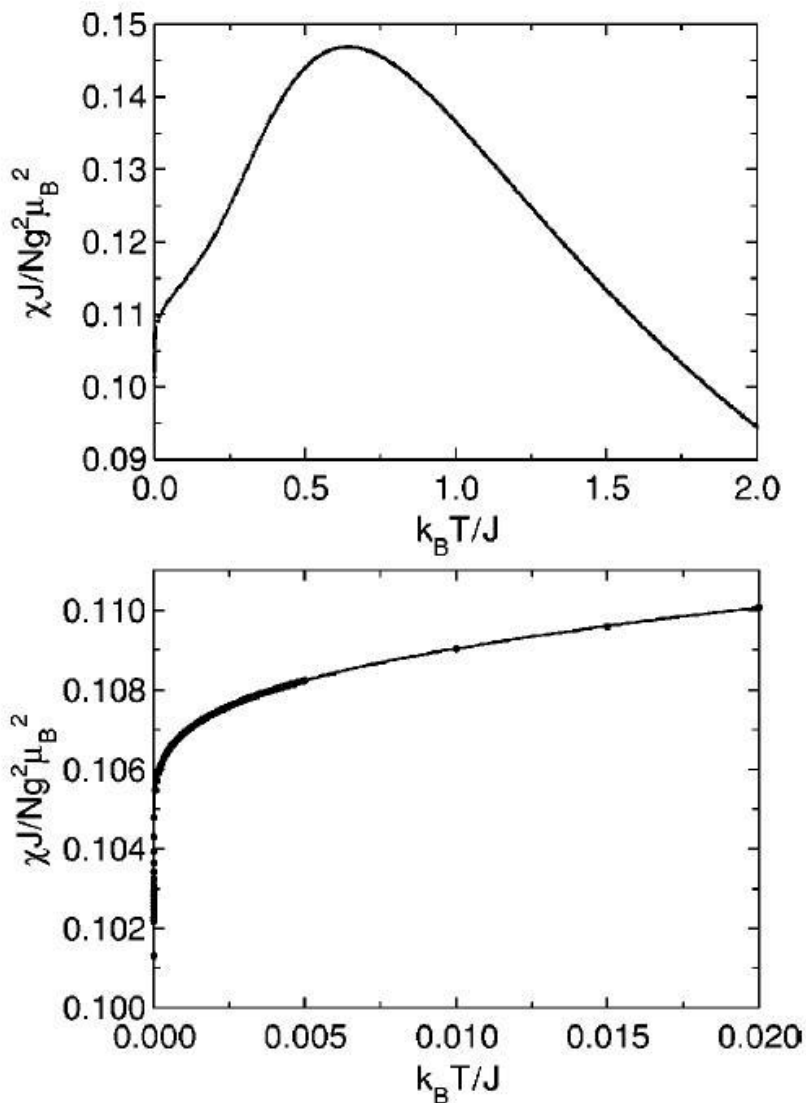Figure 8: Magnetic susceptibility χ versus temperature T for the uniform $S = ½$ AFHC in zero external fields. The lower graph shows an expansion of the data for $0 \leq k_B T/J \leq 0.02$ together with the fit. The figure is taken from Ref. [107].

Magnetic specific heat of the uniform $S = ½$ AFHC

As in the case of the magnetic susceptibility χ of the uniform $S = ½$ AFHC, the magnetic specific heat C was calculated for the first time by Bonner and Fisher in 1964 [97] and $C(T \to 0K)$, in the form of "logarithmic corrections" were studied for this quantity as well [106]. According to the recent high-accurate calculations by Klümper and Johnston [107], the zero-field magnetic specific heat of uniform $S = ½$ AFHC is given exactly in the $T \to 0K$ limit as:

$$C(T \to 0) = \frac{2}{3} \frac{N_A k_B^2 T}{J} \tag{27}$$

The linear dispersion relation of the fermionic spinons at low energy implies that the low-temperature specific heat of the $S = ½$ AFHC is linear in T [110, 111] and can be obtained by:

$$C_H(T) = \frac{\pi}{3} R \frac{k_B T}{v_S(H)} \tag{28}$$

with $v_S(H) = \frac{E}{2\pi\sigma(\Lambda)}$ the field-dependent spinon velocity. E and σ are determined by integral equations given in [112]. In zero field, $v_S = \frac{\pi J}{2}$, and the specific heat takes the form given in the equation (27).

For higher temperatures in zero field the magnetic specific heat $C(T)$ exhibits a broad maximum C^{max} at a temperature T_C^{max} with:

$$\frac{C^{max}}{N_A k_B} = 0.349712 \tag{29}$$

$$\frac{k_B T_C^{max}}{J} = 0.480285 \tag{30}$$

A universal expression for the high-temperature serial expansion-HTSE terms for $C(T)$ exists and is given for $S = ½$ by Johnston [107]:

$$\frac{C(T)}{N_A k_B} = \frac{3}{16} \frac{J^2}{k_B^2 T^2} \left(1 + \sum_{n=1}^{\infty} \frac{c_n}{(k_B T/J)^2} \right) \tag{31}$$

with $c_1 = ½$, $c_2 = c_3 = -5/16$, $c_4 = 7/256$, $c_5 = 917/7680$.

The electronic specific heat coefficient $C(T)/T$ of the uniform $S = ½$ AFHC approaches the value $\frac{2}{3} \frac{N_A k_B^2 T}{J}$ as $T \to 0K$. The initial deviation from this constant is positive and approximately quadratic in T.

The zero-field data exhibit the behaviour described above, with the broad maxima and the zero-temperature values of $C(T)$ and $C(T)/T$, respectively. With the application of an external field H, the maximum of $C(T)$ is reduced and shifts to lower temperatures, see Figure 10.
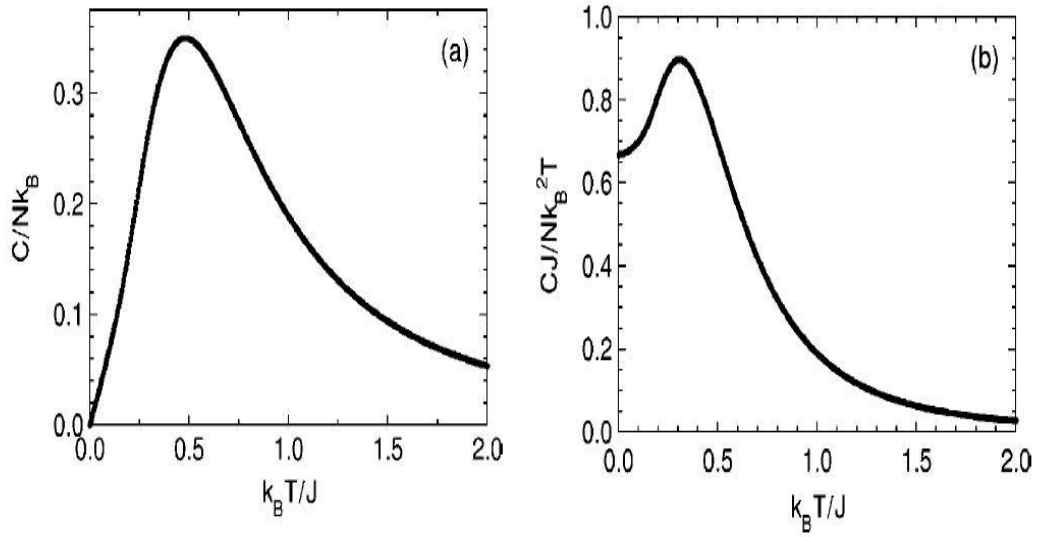
Figure 9: (a) Zero-field temperature dependence of the magnetic specific heat $C(T)$ of the uniform $S = ½$ AFHC. (b) Electronic specific heat coefficient C/T versus T from the data in (a). Figures are taken from Ref. [107].
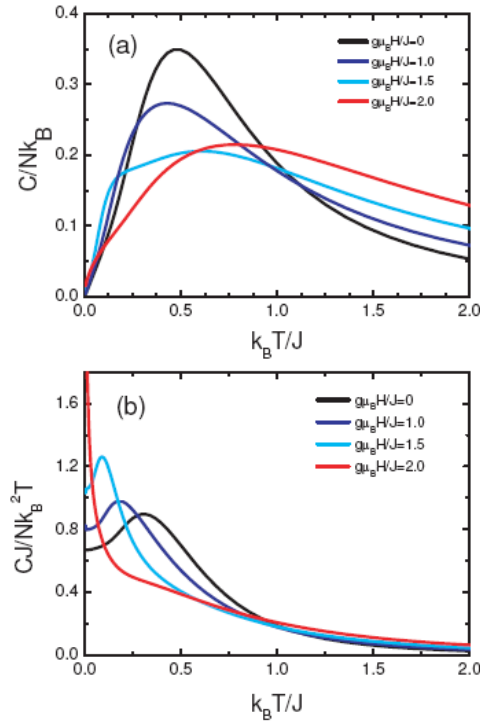

Figure 10: The specific heat of the Heisenberg chain for different values of the magnetic field (a) $g\mu_B H/J = 0, 1, 1.5, 2$, note the linear T dependence at low temperatures for fields less than the saturation value $g\mu_B H_{sat}/J = 2$. For $H = H_{sat}$ the specific heat is proportional to $T^{1/2}$ for sufficiently low T, as calculated by Klümper [106]. (b) Plot of the data from (a) as the electronic specific heat coefficient $C(T)/T$. Figures are taken from [108].

In the vicinity of the saturation field a second maximum appears. These qualitative aspects of the curves in the fixed external field can be understood in the picture of spinon excitations. The external magnetic field acts very much like a chemical potential for the spinons for which there are particle and hole-like excitations. At zero field, the bands of the particle and the hole-type excitations are identical. However, for a sufficiently strong field H the band widths vary considerably, resulting in two maxima in the specific heat at different temperatures.

At the saturation field, $H_{sat} = 2J/(g\mu_B)$, which represents a critical field above which the antiferromagnet becomes fully magnetized at zero temperature, remains a broad maximum at a higher temperature. For $H = H_{sat}$ this behaviour is qualitatively different for the electronic specific heat coefficient. Here, $C(T)/T$ diverges as $T \to 0K$, while $C(T)$ is equal to zero at $T = 0K$. Such anomalous behaviour is the signature of the existence of logarithmic corrections to the specific heat at temperatures $T << J/k_B$ [105, 106, 113], just as it was for the magnetic susceptibility.

By integrating the $C(T)/T$ data vs. T and normalizing it by $S(T \to \infty) = N_A k_B \ln 2$, the magnetic entropy $S(T)$ can be determined (see Figure 11). This figure allows one to estimate the maximum magnetic entropy that can be associated with any magnetic transition involving $S = ½$ AFHC when weakly coupled to each other [assuming that the (average) J does not change at the transition].
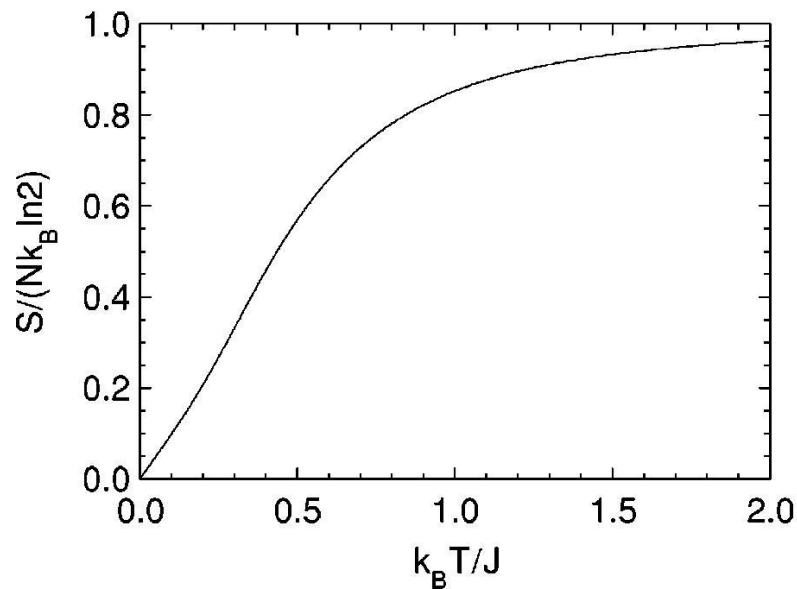

Figure 11: Entropy S vs. temperature T for the uniform $S = ½$ AFHC, obtained from the data in Fig. 9(b). The entropy is normalized by $S(T \to \infty) = N_A k_B \ln 2$. The figure is taken from Ref. [107].

According to the conservation of magnetic entropy, if the magnetic critical fluctuations increase the specific heat, and hence the entropy, above T_c than it has to be

reduced to a level below T_c for the same amount, compared to the values for the isolated chain at the same reduced temperatures.

The electronic specific heat coefficient $C(T)/T$, at low temperatures, becomes independent of temperature (apart from logarithmic corrections), as does the spin susceptibility $\chi(T)$, exactly as in a metal (Fermi liquid). For a metal, the relevant quantity is the Wilson-Sommerfeld ratio-R_W (see Equation 32), which for $S = ½$ quasiparticles is 1. Should some exchange-enhanced interaction be present in the metal, the Wilson-Sommerfeld ratio will take values $1 < R_W \leq 10$. For the $S = ½$ Heisenberg chain, $R_W = 2$ as $T \rightarrow 0K$, according to the equation:

$$R_W(T) = \frac{4\pi^2 k_B \chi(T) T}{3 N_A g^2 \mu_B^2 C(T)} \tag{32}$$

According to the Wilson-Sommerfeld ratio, the uniform $S = ½$ Heisenberg chain behaves like a Fermi liquid at low temperatures (small logarithmic corrections being neglected). This can be understood from its elementary excitations, which are $S = ½$ spinons with a Fermi surface, *i.e.*, Fermi points in one dimension. Since the spinons carry no charge, the chain is an insulator. The deviation of R_W from unity and the existence of logarithmic corrections are due to spinon interactions.

Magnetization of the uniform $S = ½$ AFHC

The magnetization M of the uniform $S = ½$ AFHC is given by $M = -\frac{1}{N}\left(\frac{\partial F}{\partial H}\right)_T$. F denotes the free energy, which is equal to the lowest eigenvalue of the Hamiltonian of the uniform $S = ½$ AFHC in an external magnetic field H (Equation 21). The magnetization as a function of the external field, as obtained by the thermodynamic Bethe ansatz by Klümper [106], is shown in Figure 12. Starting from zero field, $M(H{=}0) = 0$ at $T = 0$K, M increases monotonically with increasing external field, as:

$$M(H) = \frac{1}{\pi} arcsin \frac{1}{1-\frac{\pi}{2}+\frac{\pi J}{g\mu_B}H} \tag{33}$$

for $0 \leq H \leq H_{sat} = 2J/(g\mu_B)$.

The slope of the limiting magnetization curve at $H = 0$ is the zero point susceptibility $\chi(0)$. $M(H)$ has a sharp cusp at H_{sat} for $T = 0$K, the cusp is constantly rounded for temperatures $T > 0$K, and the saturation of the magnetization is delayed to fields $H > H_{sat}$.

Considering the derivative of the magnetization, $(\partial M/\partial H)_T = \chi(H)$, one can distinguish between three different intervals:

(1) a monotonically increasing curve for $T = 0$K, which diverges towards the saturation field and abruptly jumps to zero at $H \geq H_{sat}$

(2) an intermediate regime for $0 < T < T_c$, where $(\partial M/\partial H)_T = \chi(H)$, passes through a maximum and subsequently approaches zero at a field $H > H_{sat}$, and

(3) a regime for $T > T_c$, where $(\partial M/\partial H)_T = \chi(H)$ monotonically decreases towards zero. For the uniform $S = ½$ AFHC the inflection point T_c is given by $T_c = 1.2J/k_B$.
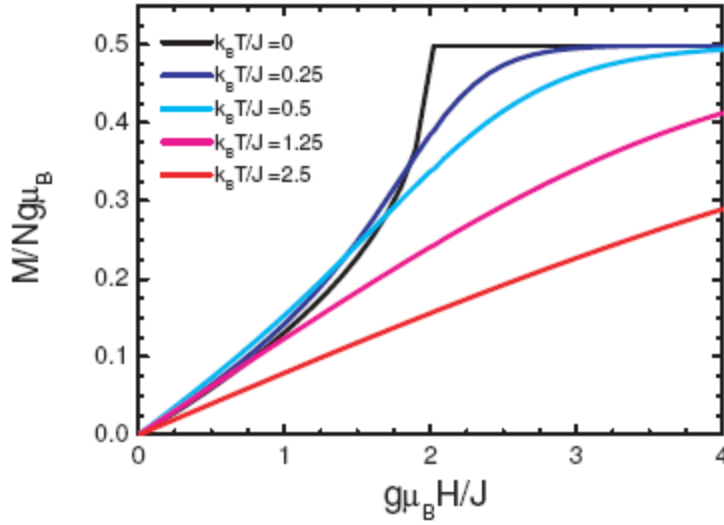
Figure 12: Magnetization curves as calculated by Klümper [106] at temperatures $0 \le k_B T/J \le 2.5$. The figure is taken from [108].

Magnetocaloric effect of the uniform $S = ½$ AFHC

The magnetocaloric effect (MCE) is related to the isothermal variation of the entropy in a magnetic field via a simple thermodynamic relation:

$$\left(\frac{\partial T}{\partial H}\right)_S = T \frac{(\partial S/\partial H)_T}{C} \tag{34}$$

where C is the specific heat at a constant magnetic field. A field variation of entropy can be found via a temperature variation of the magnetization: $(\partial S/\partial H)_T = (\partial M/\partial T)_H$. Standard examples of magnetic materials with a significant MCE include paramagnetic salts and ferromagnets near the Curie point since $(\partial M/\partial T)_H$ is large [114, 115]. Recently, it has been predicted that an enhanced MCE exists in the vicinity of field transitions in a class of geometrically frustrated antiferromagnets [116] as well as in systems which exhibit quantum phase transition [117, 118]. In some earlier works it was shown that the MCE has great importance as a new technique which could be used for magnetic cooling [119, 120, 121] and in a recent one, it was pointed out how one can use MCE for the detection and identification of quantum critical points [117, 118].

A large MCE appears near continuous phase transitions in a magnetic field for general one-dimensional (1D) quantum spin systems [122]. The phenomenon can be explained with the form of the excitation spectrum at the quantum critical point-QCP. It was observed that the excitation spectrum is softer compared to spectra above and below the transition. The soft modes increase the total magnetic entropy around the transition point which according to equation (34) produces a larger MCE.

Using the Jordan-Wigner transformation [123], the Hamiltonian of Heisenberg chain equation 19 can be mapped to a Hamiltonian of free spinless fermions and the fermion energies and saturation field are:

$$H = \sum_k (\varepsilon_k - \mu) n_k = \sum_k (\varepsilon_k - \mu) c_k^+ c_k \tag{35}$$
$$\varepsilon_k = H - J(1 - \cos k) \tag{36}$$
$$H_c = 2J \tag{37}$$

The interaction of the *z*-components of the spin in the Heisenberg chain influences the value of the fermion energies and the saturation field. The *z*-component interaction induces the interaction between the fermions but this interaction (between the fermions) in the vicinity of the saturation field for the Heisenberg chain plays a minor role [124, 125, 126].

The adiabatic de(magnetization) curves of a Heisenberg chain in magnetic field can be calculated by numerical integration of the differential relation (34). The results are presented in Figure 13 [122].
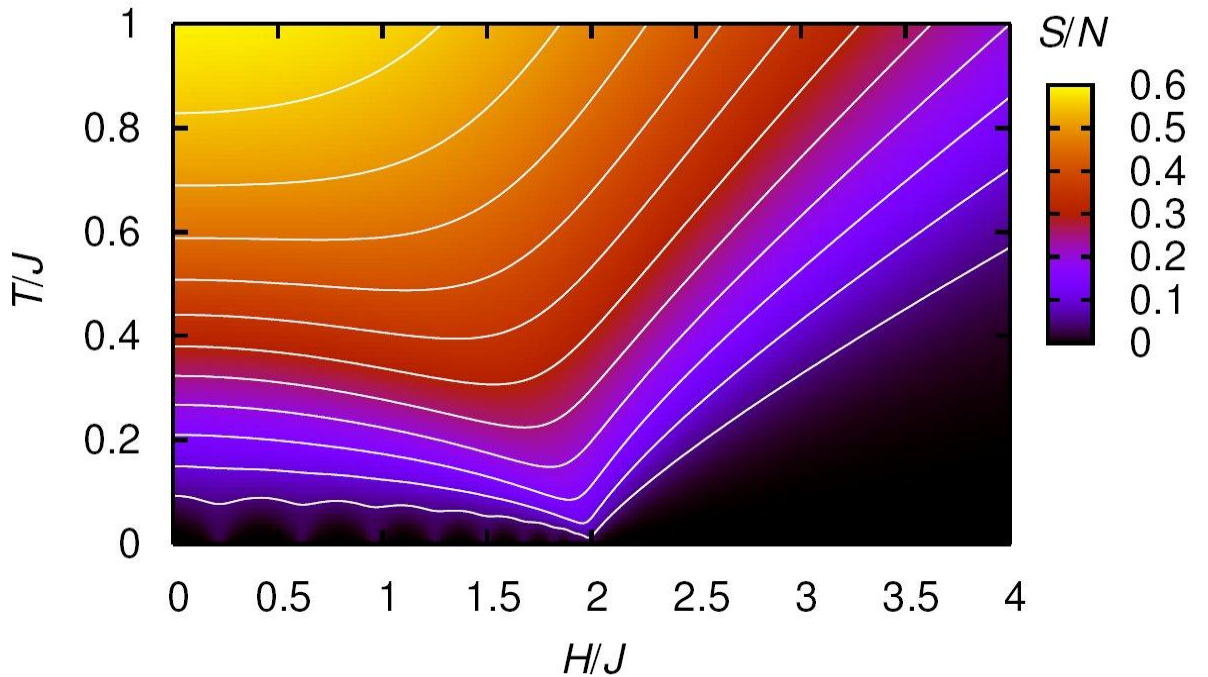
Figure 13: Adiabatic curves as a function of temperature and magnetic field of the $S = ½$ Heisenberg chain model calculated by Zitomirksky and Honecker [122].

As can be seen, in the low-temperature region there are three different regimes of isentropes for the $H < H_c$, $H = H_c$ and $H > H_c$. For $T > 0$, the system has an entropy contribution different from zero and in the applied magnetic field, the system has large relative changes in the entropy and therefore a large magnetocaloric effect. Below the saturation field, the temperature decrease is weaker than in the region above the saturation fields, the strongest temperature change, the system has near $H = H_c$. Actually the lowest temperature of the adiabatic process is reached at $H^* < H_c$ and as the temperature decreases,

the difference between these two fields becomes minimal. At the temperature close to absolute zero, the cooling rate of the adiabatic process is maximal. At low temperatures $T/J < 0.1$ the isentropes shows oscillations which originate from finite-size effects in the calculations [122].

It has been shown that the frustration increases entropy at low temperatures at the saturation field [122] and that the frustrated systems have an enhanced magnetocaloric effect. Comparison of adiabatic curves for the $S = ½$ AFHC, the J_1-J_2 chain and the sawtooth chain are shown in Figure 14. During an adiabatic demagnetization, all three systems cool upon approaching the saturation field, the J_1-J_2 chain cools down to lower temperatures than the $S = ½$ AFHC under the same conditions, and the sawtooth chain to even lower temperatures. The enhancement of the magnetocaloric effect with increasing frustration is evident.
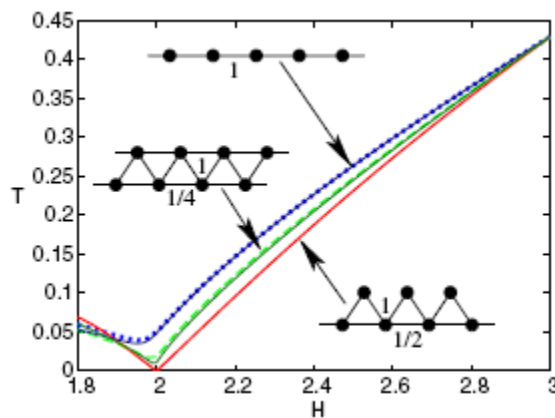
Figure 14: Isentropes upon approaching the saturation field from above for the $S = ½$ Heisenberg chain, the J_1-J_2 chain with $J_1 = J$, $J_2 = 1/4J$, and for the sawtooth chain with $J_1 = J$, $J_2 = 1/2J$. The bold curves present the results of numerical calculations and the two thin curves present a free-fermion approximation. The figure is taken from [122].

One-dimensional quantum spin systems in an external magnetic field exhibit large relative changes of entropy and pronounced magnetocaloric effect. These properties enable these low-dimensional systems to be promising refrigerant materials in low-temperature physics and industry.

2.3.2 Alternating-exchange chains

In an alternating Heisenberg chain the nearest-neighbor spins in the chain interacting via the Heisenberg interaction and the spin Hamiltonian in zero field has the form:

$$H = J \sum_{i=1}^{n/2} \left[S_{2i} S_{2i-1} + \alpha S_{2i} S_{2i+1} \right] \tag{38}$$

The alternation parameter is $\alpha = J'/J$, the uniform Heisenberg chain is one limit of the alternating chain in which $\alpha = 1$ and $J = J'$, whereas the other limit is the isolated dimer in which one of exchange constants is zero and $\alpha = 0$.

The spin gap of the alternating-exchange chain $\Delta(\alpha)$ was calculated by Barnes *et al.* [127] and they found:

$$\Delta(\alpha) \approx (1 - \alpha)^{3/4}(1 + \alpha)^{1/4}J \tag{39}$$

2.4. Quantum phase transitions - QPT

Phase transitions play an essential role in nature and numerous examples abound, such as boiling of water, melting of ice or, more complicatedly, transition of a metal into the superconducting state. The universe itself is thought to have passed through several phase transitions as the high-temperature plasma, formed by the Big Bang, cooled to form the world as we know it today. Phase transitions occur usually upon variation of an external control parameter; their common characteristic is a qualitative change in the system properties. They occur at a finite temperature, where macroscopic order is destroyed by thermal fluctuations.

A different class of phase transitions also exists in nature, namely transitions which take place at zero temperature known as quantum phase transitions (QPT). In the systems which undergo QPT, order is destroyed solely by quantum fluctuations. A control parameter which brings the system to the transition is non-thermal in nature such as pressure, electric field, magnetic field, or chemical composition. Quantum phase transitions [128] have become a topic of great interest, while the presence of zero temperature quantum critical points (QCPs) holds the key to currently unsolved puzzles in many systems, such as rare-earth magnetic insulators [129], heavy fermion compounds [130, 131], high-temperature superconductors [132, 133] and two-dimensional electron gases [134]. Quantum critical behaviour, arising from the peculiar excitation spectrum of the quantum critical ground state, can influence measurable quantities over a wide range of the phase diagram.

Traditionally, phase transitions are classified into first-order and continuous transitions. At a first-order transition, the two phases co-exist at the transition temperature (ice and water at 0°C or water and steam at 100°C). In contrast, at a continuous transition, the two phases do not co-exist (for example, the ferromagnetic transition of iron at 770°C, above which the magnetic moment vanishes). Continuous phase transition can usually be characterized by an order parameter, a thermodynamic quantity that is zero in one phase (the disordered) and non-zero and non-unique in the other (the ordered) phase. Very often, the choice of an order parameter for a particular transition is obvious but in some cases finding an appropriate order parameter is complicated and is still a matter of debate, (the Mott transition [135] for example). A quantitative characteristic of an order parameter in the disordered phase is that its average value is zero, while its fluctuations are non-zero. If the critical point is approached, the spatial correlations of the order parameter fluctuations become long-ranged. Close to the critical point, the correlation length, ξ, diverges as:

$$\xi \propto |t|^{-\nu} \tag{40}$$

where ν is the correlation length critical exponent and t is some dimensionless measure of the distance from the critical point. If the transition occurs at a non-zero temperature T_c, it can be defined as $t = |T - T_c|/T_c$. In addition to the long-range correlations in space there are analogous long-range correlations in time. The typical timescale for a decay of the fluctuations is the correlation (or equilibration) time, τ_c. As the critical point is approached the correlation time diverges as:

$$\tau_C \propto \xi^z \propto |t|^{-\nu z} \tag{41}$$

where z is the dynamic critical exponent. Close to the critical point, the characteristic length scale is ξ and the characteristic timescale is τ_c. The divergences of correlation length and correlation time are responsible for the so-called critical phenomena. At the phase transition point, correlation length and time are infinite, fluctuations occur on all length scales and timescales, and the system is said to be scale-invariant. As a consequence, all observables depend via power laws on the external parameters. The set of corresponding exponents (critical exponents) completely characterizes the behaviour near the phase transition.

The underlying quantum phase transition in some system manifests itself at finite temperatures in an unusual sensitivity of thermodynamics on tuning some of the external parameters. Here we will discuss some aspects of the QPT where the QCP is reached by tuning the magnetic field-H. At $T = 0K$ the distance to the QCP is determined by the control parameter which depends on magnetic field, $r = r(H)$ see Figure 15.
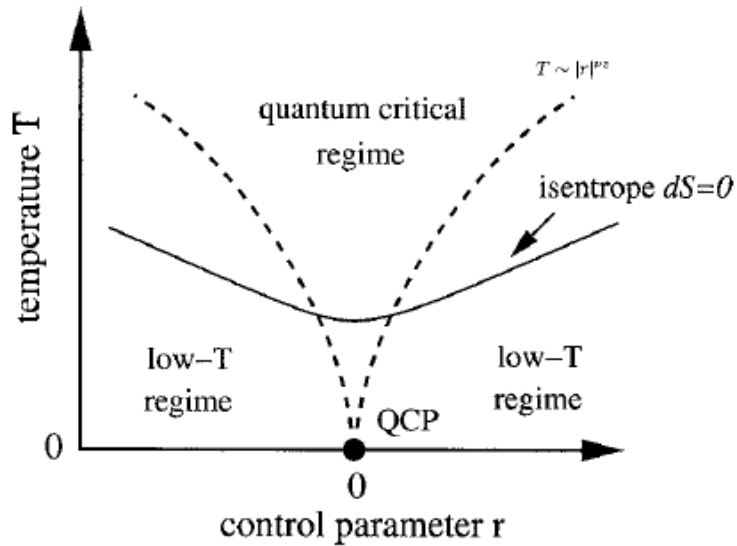
Figure 15: Different regimes in the phase diagram of a quantum phase transition. The solid line shows a generic isentrope along which the entropy is constant, $dS = 0$. Figure is taken from [118].

As can be seen from Figure 15, with respect to the QCP one can distinguish two regimes in the phase diagram, namely the quantum critical regime and the low-T regime. In both of them the measurable quantities behave differently.

In the surrounding of the QCP the control parameter can be linearized around its critical value:

$$r(H) = (H - H_c)/H_0 \tag{42}$$

where H_0 is a constant magnetic field and H_c is the critical field where the transition occurs. Generically, the critical magnetic field will depend also on pressure, $H_c = H_c(p)$, and vice versa.

If the QPT is tuned by the magnetic field, than the free energy density is a function of this control parameter and temperature, $f = f(H,T)$. Thermodynamically, the sensitivity on the tuning magnetic field is measured by the derivative of the free energy density with respect to H and has the quantity $(dM/dT)_H$. The quantity known as the magnetocaloric effect can be defined as:

$$\Gamma_H = \frac{(\partial M/\partial T)_H}{C_H} = -\frac{1}{T}\frac{(\partial S/\partial H)_T}{(\partial S/\partial T)_H} = \frac{1}{T}\frac{\partial T}{\partial H}\bigg|_S \tag{43}$$

where C_H is the specific heat at constant H. The magnetocaloric effect-Γ_H can be experimentally observed under adiabatic conditions by measuring the change in temperature at constant entropy upon magnetic field variations. On looking at the equation (43), it is obvious that the magnetocaloric effect is proportional to the slope of the constant entropy curves (isentropes) in the phase diagram.

Applying the scaling analysis [117] in the quantum-critical regime, i.e., for $T \gg |r|^{vz}$ it is obtained:

$$\Gamma_H \propto \frac{1}{T^{1/vz}} \tag{44}$$

the magnetocaloric effect is in this region magnet-field independent and depends only on the temperature of the system and critical exponents v and z.

On the other hand, in the low-T regions $T \ll |r|^{vz}$, the magnetocaloric effect diverges inversely with applied magnetic-field:

$$\Gamma_H = -G_r \frac{1}{(H-H_C)} \tag{45}$$

In this region the magnetocaloric effect depends also on the critical exponents because they define the value of G_r by the relation:

$$G_r = -v\frac{y_0^{\pm}z-d}{y_0^{\pm}} \tag{46}$$

where $y_0^{\pm}$ are critical exponents which define the low-T behaviour of the specific heat of the system and d define the dimensionality of the system.

As can be seen from equation (45), where G_r has the same sign in both low-T regions, the sign change of this quantity takes place. The equation (45) implies a divergence and sign change of the magnetocaloric effect in the low-T regions, these are very strong signatures of this quantity. The natural question is where and when does the sign change take place?

Sign change of Magnetocaloric Effect

In order to understand why the magnetocaloric effect changes the sign, one should consider the behaviour of the entropy within the temperature-field plane. As can be seen from Figure 15, on the left-hand side of the QCP the isentrope line has a negative slope while on the right-hand side of the QCP the slope is positive. This means that somewhere in the near surrounding of the QCP, the sign change takes place *i.e.* in the quantum critical region. The minimum of the isentrope is directed toward the QCP because as the system approaches to the QCP, it accumulates the entropy and at the QCP system is frustrated (with the two possible different ground states which it can take). The minimum of the isentrope describes how the entropy accumulates around the QCP and is located at the field in the phase diagram where the system waves on the choice of the ground states (has frustration).

Using a scaling analysis one can determine the behaviour of the isentropes. For the low-temperature region it is:

$$T(H - H_c)_S \propto |H - H_c|^{-G_r} \tag{47}$$

from the above relation it is clear that the isentropes have power low behaviour and the exponent of the power low dependence is given by the value G_r. If the $G_r < 0$ this means that the isentropes have a minimum.

If one considers an Ising chain as an example of the system which orders at zero-temperature, where the critical exponents important for the discussion have values $d = 1$, $z = 1$, $\nu = 1$ and $y_0^\pm = \infty$, the factor G_r, which determines the behaviour of the system in the low-temperature region, will have the magnitude:

$$G_r = -\nu z = -1 \tag{48}$$

Calculating the thermodynamic quantities with previously mentioned critical exponents, the isentropes of the system will have the form shown on the Figure 16(a). The magnetocaloric effect-Γ_H will be according to the equation (45) inversely proportional to the applied magnetic field. Because of the inversion symmetry with respect to the applied field ($H - H_c \rightarrow H_c - H$), the sign change will take place directly at the $H = H_c$, see Figure 16(b).
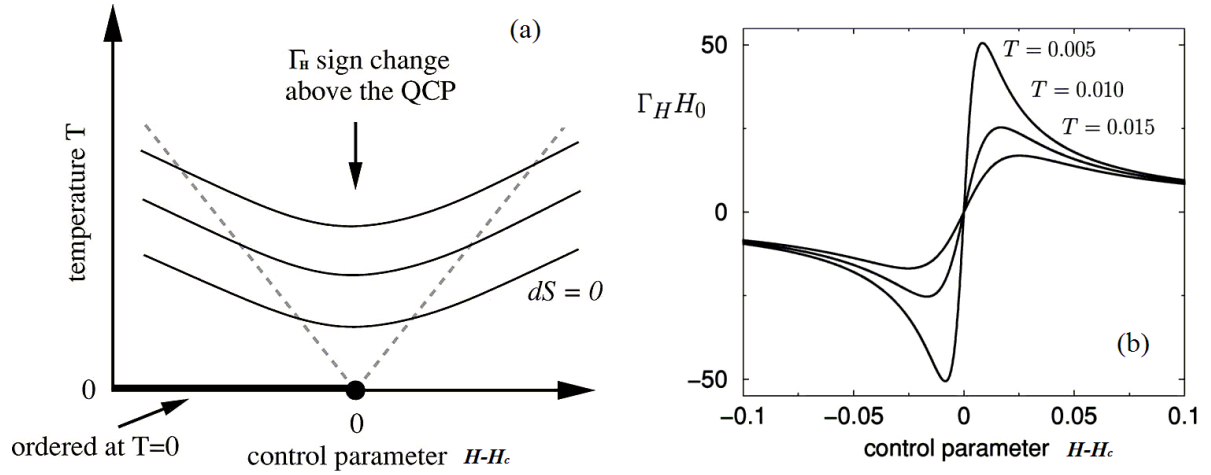
Figure 16: (a) Adiabatic (de)magnetization curves-isentropes of the Ising chain. (b) Magnetocaloric effect at different temperatures. Figure is taken from [118].

As one can see from the Figure 16(b), on approaching the critical field from the left and right hand side, the magnetocaloric effect diverges. Such a divergence in a combination with the sign change leads to the very pronounced signature of the magnetocaloric effect in the surrounding of the critical field.

A similar behaviour of the magnetocaloric effect will have the Heisenberg chain since in this type of the system critical exponents have the values $d = 1$, $z = 2$, $\nu = \frac{1}{2}$ and $y_0^{\pm} = \infty$ and the factor G_r have the same magnitude as in the case of the Ising chain. This means that in the case of the Heisenberg chain, the MC effect will also diverge on approaching the critical field from the left and right hand side of the low-temperature region. This divergence, in a combination with the sign change (which will take place in this system also), will result in a pronounced signature of the MC effect as in the case of Ising chain. Therefore the magnetocaloric effect can be used as a very powerful tool to detect and identify the quantum critical point of such systems.

3. Experimental Methods

3.1. Quantum Design MPMS XL-5

DC − Magnetometer

DC magnetic measurements determine the equilibrium value of the magnetization in a sample. The sample is magnetized by a constant magnetic field and the magnetic moment of the sample is then measured, producing a DC magnetization curve $M(H)$. The moment is measured by force, torque or induction techniques, the last being the most common in modern instruments. Inductive measurements are performed by moving the sample relative to a set of pickup coils, either by vibration or one-shot extraction. In conventional inductive magnetometers, one measures the voltage induced by the moving magnetic moment of the sample in a set of copper pickup coils. A much more sensitive technique uses a set of superconducting pickup coils and a SQUID to measure the current induced in superconducting pickup coils, yielding high sensitivity that is independent of the sample speed during the extraction. Inductive magnetometers can also be used to perform AC magnetic measurements.

AC − Magnetometer

In AC magnetic measurements, a small AC drive magnetic field is superimposed on the DC field, causing a time-dependent moment in the sample. The field of the time-dependent moment induces a current in the pickup coils, allowing measurement without sample motion. The detection circuitry is configured to operate only in a narrow frequency band, normally at the fundamental frequency (that of the AC drive field). In the case of very low frequencies an AC measurement is most similar to a DC measurement. In this case, the magnetic moment of the sample follows the $M(H)$ curve that would be measured in a DC experiment. As long as the AC field is small, the induced AC moment is $M_{AC} = (dM/dH)H_{AC}$ $\sin(\omega t)$ where H_{AC} is the amplitude of the driving field, ω is the driving frequency, and $\chi = dM/dH$ is the slope of the $M(H)$ curve, called the susceptibility. As the DC magnetic field is changed, different parts of the $M(H)$ curve are accessed, giving a different susceptibility. One advantage of the AC measurement is already evident: the measurement is very sensitive to small changes in $M(H)$. Since the AC measurement is sensitive to the slope of $M(H)$ and not to the absolute value, small magnetic shifts can be detected even when the absolute moment is large.

At higher frequencies than those considered above, the AC moment of the sample does not follow along the DC magnetization curve due to dynamic effects in the sample. For this reason, the AC susceptibility is often known as the dynamic susceptibility. In this higher frequency case, the magnetization of the sample may lag behind the drive field, an effect that is detected by the magnetometer circuitry. Thus, the AC magnetic susceptibility measurement yields two quantities: the magnitude of the susceptibility, χ, and the phase shift, ϕ (relative to the drive signal). Alternately, one can think of the susceptibility as having an in-phase, or real, component χ', and an out-of-phase, or imaginary, component χ''. The two representations are related by:

$$\chi' = \chi \cos \varphi \tag{49}$$

$$\chi'' = \chi \sin \varphi \tag{50}$$

In the limit of low frequency where an AC measurement is most similar to a DC measurement, the real component χ' is just the slope of the *M(H)* curve discussed above. The imaginary component, χ'', indicates dissipative processes in the sample. In conductive samples, the dissipation is due to eddy currents. In ferromagnets, a nonzero imaginary susceptibility can indicate irreversible domain wall movement or absorption due to a permanent moment. Also, both χ' and χ'' are very sensitive to thermodynamic phase changes, and are often used to measure transition temperatures.

Superconducting Quantum Interference Device – SQUID

The SQUID magnetometer is one of the most effective and sensitive ways of measuring magnetic properties. In particular, it is the only method which directly allows determination of the overall magnetic moment of a sample in absolute units. The term SQUID is an abbreviation and stands for *Superconducting Quantum Interference Device*.

Following the equations established by Brian David Josephson in 1962, the electrical current density flowing through a weak electric contact between two superconductors depends on the *phase difference $\Delta\varphi$* of the two superconducting wave functions. Moreover, the time derivative of $\Delta\varphi$ is correlated with the voltage across this weak contact. In a superconducting ring with one (so-called RF SQUID) or two (DC SQUID, Figure 17, blue) weak contacts, $\Delta\varphi$ is additionally influenced by the magnetic flux Φ through this ring. Therefore, such a structure can be used to convert magnetic flux into an electrical voltage.
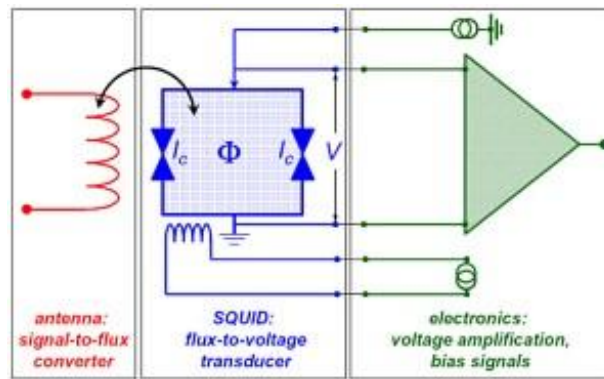
Figure 17: SQUID: flux-to-voltage converter.

In this work a commercial SQUID magnetometer system from Quantum Design, San Diego was utilized. The sample is located at the center of a superconducting solenoid producing magnetic fields up to 5T. The sample space is filled with helium at low pressure at temperatures ranging from 2-400K. The sensitivity of the system is 10^{-8}emu or 10^{-11}J/T in the RSO mode. The magnetic signal of the sample is obtained via a superconducting *pick-up coil* with 4 windings, see Figure 18. This coil is, together with a SQUID antenna (red in Figure 17), part of a whole superconducting circuit, transferring the magnetic flux from the sample to an RF-SQUID device, located away from the sample in the liquid helium bath. This device acts as a magnetic flux-to-voltage converter (blue in Figure 17). This voltage is then amplified and read out by the magnetometer's electronics (green in Figure 17). When the sample is moved up and down it produces an alternating magnetic flux in the pick-up coil leading to an alternating output voltage of the SQUID device. By locking the frequency of the readout to the frequency of the movement (RSO, Reciprocating Sample Oscillation), the magnetometer system can achieve extremely high sensitivity for ultra small magnetic signals as described above.
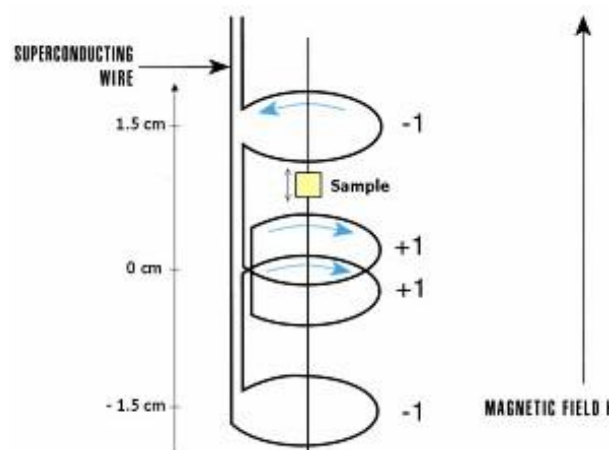
Figure 18: Scheme of the pick-up coils system.

RSO Measurements

Unlike DC measurements where the sample is moved through the coils in discrete steps, the Reciprocating Sample Option (RSO) measurements are performed using a servo motor which rapidly oscillates the sample, see Figure 19. A shaft encoder records the position of the sample synchronous with the SQUID signal. The data received is fitted to an ideal dipole moment response. To ensure this assumption is applicable, samples need to be small, for example, a cylinder of 3mm diameter and 3mm height. Samples of this size or smaller match an ideal point dipole [136]. RSO measurements can be made in one of two configurations: Center or Maximum slope. Center mode uses large oscillations (2 to 4cm) around the center point of the pickup coils. The scans take a long time, the sample always remains properly located and a large number of measurements can be recorded. This method gives the most accurate readings. The Maximum Slope method oscillates the sample over a small region (2mm) at the most linear part of the SQUID response (as shown in Figure 19). The smaller amplitude makes measurements quicker and prevents the sample being subjected to a significant magnetic field variation; however, it also makes the measurement less accurate and susceptible to drift in the sample position.

All measurements taken in this thesis using the MPMS XL SQUID were performed in Center mode with amplitude of 4cm.
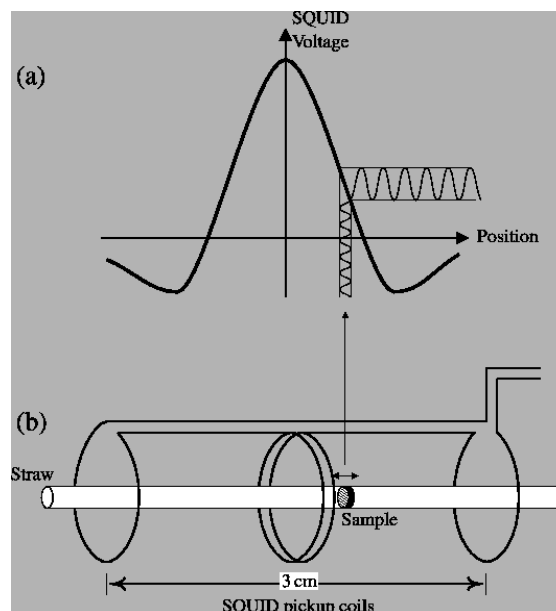
Figure 19: Illustration of an RSO measurement with the small amplitude. (a) Shows the ideal SQUID response for a dipole and (b) shows the movement of the sample within the SQUID pick-up coil.

3.2. $^3He/^4He$ dilution refrigerator

The $^3He/^4He$ dilution refrigerator operation principle was originally proposed by Heinz London in 1951, but the first working systems were not built until more than ten years later. These days, commercial $^3He/^4He$ dilution refrigerators are available for temperatures down to about 4mK. The minimum temperature obtained by the method to be discussed below is about 2mK, achieved by Frossati and co-workers.

The essence of the dilution refrigerator method is to use a mixture of ^3He (boiling temperature 3.19K) and ^4He (4.2K) which is separated into two phases, and to dilute this mixture with pure ^4He. Inside the "mixing chamber", where the mixture is condensed, two distinct phases are formed. The pure ^4He cannot dissolve in the ^3He-rich phase as this is already saturated with ^{4}He. The additional ^4He increases the volume of the ^4He-rich phase, while at the same time ^3He atoms from the ^3He-rich phase pass into the ^4He-rich phase, so as to maintain the equilibrium concentration. Hence, during the dilution, ^3He atoms evaporate from the ^3He-rich phase into the ^4He-rich phase. By continuously pumping the mixture, ^3He atoms are removed from the diluted phase. This allows more ^3He atoms to diffuse out of the condensed phase into the diluted one, further cooling the mixture.

All the measurements are performed in a commercial $^3He/^4He$ dilution refrigerator, model 400S from the Oxford Instruments company. The achievable temperature range of this cryostat is 15mK-6.6K, and superconducting magnet realizing the fields $\leq$ 15.5T, with the use of Lambda point refrigeration field of 17T is reachable. Around the mixing chamber, there is a field-compensated zone in which all thermometers can be placed (compensation field- $\mu_0H_{kom} \leq$ 3mT). The mixing chamber temperature is measured with a commercial calibrated Ge thermometer in the temperature range 1.2K $\leq T \leq$ 6.6K, a commercially calibrated RuO_2 thermometer in the range 0.03K $\leq T \leq$ 1.2K and for the temperature $T \leq$ 0.1K a home made CMN-thermometer [137] calibrated with a fix-point device.

3.2.1. AC – Susceptibility Measurements

An inductive magnetometer is used to perform AC magnetic measurements. For this type of measurements, an *ac* current is used (ν = 117Hz, $I \approx$ 0.1mA) with which a field amplitude μ_0H_{AC} = 100μT is accomplished. In the coil, the construction of which is explained below, two opposite voltages will be induced astatic in the secondary. If the sample is placed in one of the two secondary coils (cross section A and length l), additional voltage proportional to the susceptibility of the sample, is induced. The voltage signal is detected with the Lock-in technique, according to the electronic scheme showed in Figure 20.
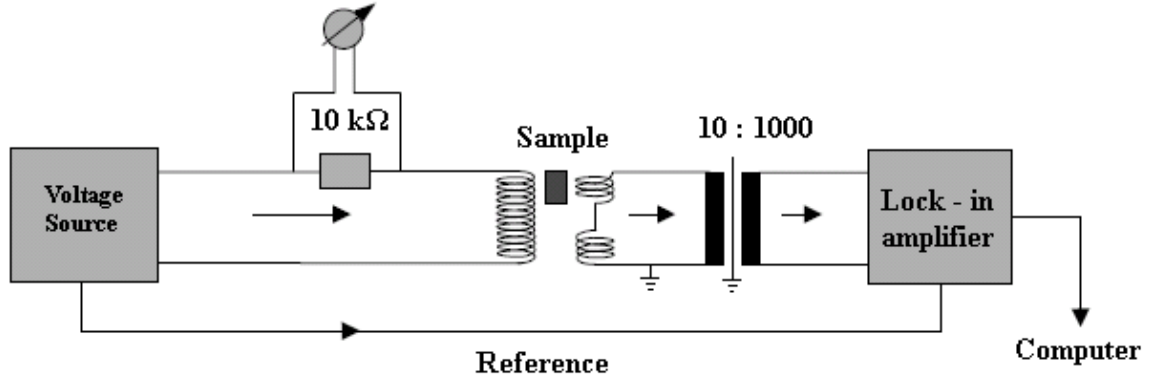
Figure 20: Diagram of the AC - Susceptibility measurements in the bottom-loading cryostat.

The induced voltage is:

$$U_{ind}(t) = -N_S \frac{d\Phi_S}{dt} = -N_S A \mu_0 \frac{dM(t)}{dt} \tag{51}$$

N_S – number of windings of the pick-up coil

μ_0 – vacuum permeability

$M(t)$ – sample magnetization

So from the measured voltage one has:

$$U_{ind}^{\Delta\varphi=90°} = \frac{2\pi\nu}{\sqrt{2}} N_S \frac{V_S}{l} \mu_0 H_{AC} \chi' \tag{52}$$

$$U_{ind}^{\Delta\varphi=180°} = \frac{2\pi\nu}{\sqrt{2}} N_S \frac{V_S}{l} \mu_0 H_{AC} \chi'' \tag{53}$$

V_S – volume of the sample

The phase shift between both the measured and reference signal is induced by the sample holder.

The measurement coil (see Figure 21) consists of a long primary coil around which a couple of astatic secondary coils have been wound. In the case of perfect astatic conditions, the induced voltage in both the secondary coils will be mutually deleted. Because the secondary coils are not completely astatic, two different voltages will be induced in the coils and the resultant voltage will give a finite offset. To suppress the offset, two other astatic primary coils have been wound, so that they are parallel to a real primary coil and together with the changeable resistor (ca. 200kΩ) are connected to the voltage source. In this way, the resolution of the coil is improved. The sample in one of the pick-up coils induces a voltage, which is proportional to the sample susceptibility. This measurement principle permits only the determination of the susceptibility change. To determine the absolute values, it is necessary to perform additional measurements on a calibrated sample.
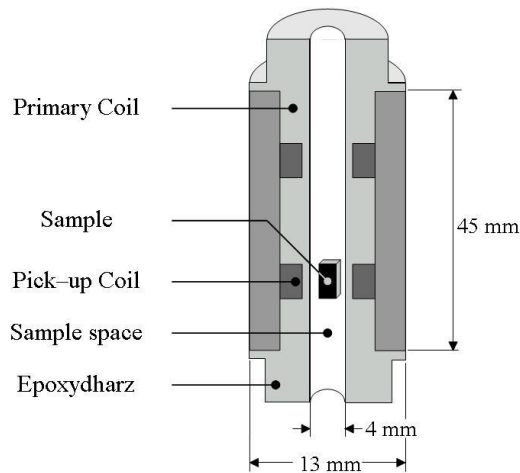
Figure 21: Schematic cross-section of the AC-susceptibility sample holder.

3.2.2. DC – Susceptibility Measurements

DC-magnetization measurements are performed with the home-made sample holder and a commercial SQUID-sensor from Oxford Instruments. The sample holder [138] is placed in the field-compensated zone directly below the mixing chamber. It consists of a small coil made from a superconducting wire which can produce a field strength of up to 8mT ($\mu_0 H =$ (0.128 mT/mA)·I) [138]), as well as a pair of astatically wound pick-up coils. The pick-up coils are wound with NbTi wire and each of them has three windings. The sample is thermally coupled to the mixing chamber over the Cu-wires in which it is packed and placed in one of the pick-up coils. A signal from the pick-up coil passes over a flux transformer to the SQUID-sensor. The flux transformer is placed in the Pb-Zn capillary [138] which serves as a shield. The SQUID-sensor is placed directly onto the 1K-pot of the cryostat [139]. The rest of the SQUID electronics are outside the cryostat.

3.2.3. Magnetocaloric effect (MCE) measurements

Some magnetic materials heat up when they are placed in a magnetic field and cool down when they are removed. This is known as the *magnetocaloric effect*. The heating/cooling of a magnetic system under an adiabatic (de)magnetization process, is related to the isothermal variation of the entropy in a magnetic field via a simple thermodynamic relation, see Equation 34.

When a material is magnetized by application of a magnetic field, the entropy associated with the magnetic degrees of freedom, S_m, is changed. Under adiabatic conditions, ΔS_m must be compensated for by an equal but opposite change in the entropy associated with the lattice, ΔS_l, resulting in a change in temperature of the material, ΔT. The magnetocaloric effect can be related to the magnetic properties of the material, since magnetic properties are easier to measure directly than the entropy of the system. Through the thermodynamic Maxwell's equation $\left(\frac{\partial S}{\partial H}\right)_T = \left(\frac{\partial M}{\partial T}\right)_H$, the above relation takes the form:

$$\left(\frac{\partial T}{\partial H}\right)_S = -T\frac{(\partial M/\partial T)_H}{C} \tag{54}$$

The MCE can be measured either by scanning the temperature during the field sweep under adiabatic conditions (quasi-adiabatic calorimetry) or by measuring the temperature dependence of the magnetization in the constant field (magnetization measurement) and the *T*-dependence of the specific heat at constant field or field dependent specific heat at different temperatures (specific heat measurement). An easier and more direct method would be quasi-adiabatic calorimetry. Quasi-adiabatic calorimeter can be used for *ac*-calorimetry where a calorimeter is weakly coupled to the thermal bath. Such a microcalorimeter usually consists of a thermometer with an integrated sample holder with a low specific heat. In most of the designs published, the sample platform consists of a sapphire or diamond substrate with a thermometer. Such a calorimeter is mounted onto a high vacuum cryogenic inset by means of thin supporting wires which also act as electrical connectors to the thermometer, and which provide only a weak and controllable coupling to the thermal bath [140]. Thermometry is crucial for such a type of measurement; this means that the thermometer should have a high sensitivity and a short response time. Furthermore the thermometer should be well anchored to the sample/platform system and should be non-magnetic. In this sense, thin film resistance thermometry is more sensitive and reliable than the thermocouple thermometry. In the set-up used in this work, a commercially available thin film RuO_2 thermometer was utilized. For the purpose of this work it was the optimal choice since it covers the desirable temperature range with the same sensitivity and, for low-temperatures, had sufficiently high sensitivity for detecting of millikelvin variations.

The *ac*-calorimetry is the ideal method for measuring small changes of temperature. Assuming τ_1 is the relaxation time of the microcalorimeter/sample assembly and with τ_2 is the relaxation time of the assembly to the bath then, in the limit $\omega_1\tau_1 \ll \omega_2\tau_2$, the appropriate temperature change of the sample can be measured. To check if the system is in this limit

ΔTω versus *ω* curve has to be traced to determine the frequency below which the heat escapes through the thermal links to the bath and above which the substrate is unable to follow the rapid heat modulations. In the range between, steady state conditions are realized. A photograph of the calorimeter and the sample is shown in Figure 22. For the electrical leads, Pt-W wires (25μm in diameter and ~ 1cm in length) were used as they are thermally anchored to the bath over the copper frame. Wires are used as thermal and electrical contacts. For the mechanical support, nylon wires 0.1mm in diameter were used. Mechanical support is important to ensure that there are no mechanical vibrations due to the magnetic field. Bonding to the mechanical support is done so that the sample is correctly aligned in the magnetic field (parallel alignment). Since the thermal contact is made over the wires, it has to be chosen so that the thermal conductivity between the microcalorimeter and bath has a proper value. The thermal conductivity and the resulting relaxation time can be controlled by making the wires longer and thinner and by using higher resistivity alloys. The sample can be mounted with a small drop of Apiezon N-grease. The thermal conductance between the bath and the calorimeter was estimated to be ~ 10^{-8}W/K. By applying a heat pulse to the calorimeter, the thermal relaxation time constant of the calorimeter to the bath temperature was found to be ~ 1000s at the temperatures and fields at which the MCE measurements were performed.
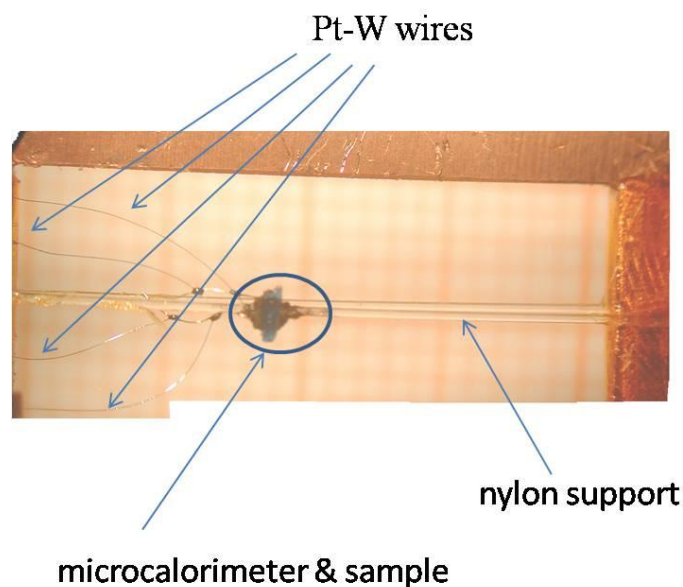
Figure 22: Photo of the microcalorimeter chip mounted on the Cu frame. The sample (blue single crystal CuP) is mounted on one side of the chip with Apiezon N-grease.

3.3. Electron spin resonance

Electron spin resonance (ESR) spectroscopy is a technique for studying materials that have one or more unpaired electrons, such as organic and inorganic free radicals or inorganic complexes possessing a transition metal ion. The basic physical concepts of EPR are analogous to those of nuclear magnetic resonance (NMR), but it is the electron spins that are excited instead of spins of atomic nuclei. Because most stable molecules have all their electrons paired, the EPR technique is less widely used than NMR.

Every electron has a magnetic moment and spin quantum number $S = \frac{1}{2}$, with magnetic components $m_s = + \frac{1}{2}$ and $m_s = - \frac{1}{2}$. In the presence of an external magnetic field with strength B_0, the electron's magnetic moment aligns itself either parallel ($m_s = - \frac{1}{2}$) or antiparallel ($m_s = + \frac{1}{2}$) to the field, each alignment having a specific energy. The parallel alignment corresponds to the lower energy state, and the separation between it and the upper state is $\Delta E = g_e \mu_B B_0$, where g_e is the electron's so-called g-factor. This equation implies that the splitting of the energy levels is directly proportional to the magnetic field's strength, as shown in Figure 23. An unpaired electron can move between the two energy levels either by absorbing or emitting electromagnetic radiation of energy $\varepsilon = h\nu$ such that the resonance condition, $\varepsilon = \Delta E$, is obeyed. Substituting in $\varepsilon = h\nu$ and $\Delta E = g_e \mu_B B_0$ leads to the fundamental equation of EPR spectroscopy:

$$h\nu = g_e \mu_B B_0 \tag{55}$$

Experimentally, this equation permits a large combination of frequency and magnetic field values.
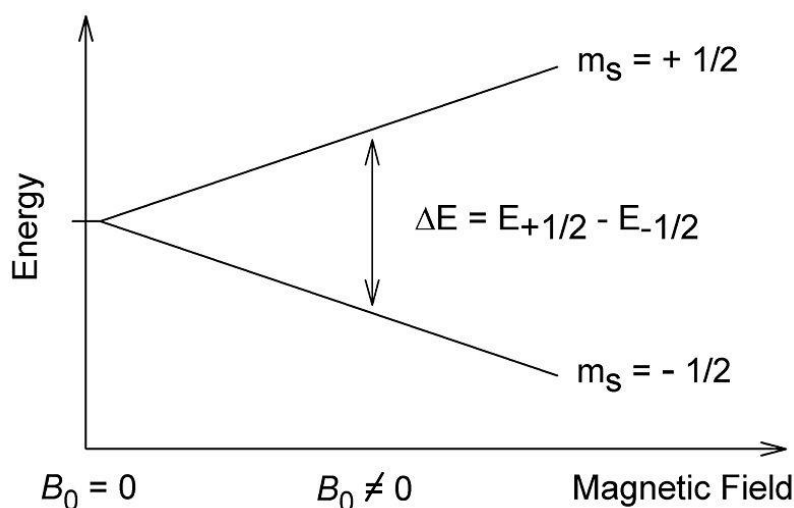

Figure 23: Energy level splitting in the magnetic field-Zeeman Effect.

In principle, EPR spectra can be generated by either varying the photon frequency while holding the magnetic field constant, or doing the reverse. In practice, it is usually the frequency which is kept fixed. By increasing an external magnetic field, the gap between the $m_s = +\frac{1}{2}$ and $m_s = -\frac{1}{2}$ energy states is widened until it matches the energy of the microwaves, as represented by the double-arrow in the Figure 23. At this point the unpaired electrons can move between their two spin states. Since, there are more electrons in the lower state, due to the Maxwell-Boltzmann distribution, there is a net absorption of energy, and this absorption is monitored and converted into a spectrum.

In real systems, electrons are normally not solitary, but are associated with one or more atoms. Therefore ESR spectroscopy can be used to determine:

1) ***g*-factor value**
   An unpaired electron can gain or lose angular momentum, which can change the value of its g-factor, causing it to differ from g_e. This is especially significant for chemical systems with transition-metal ions.

2) **Hyperfine coupling constant**
   If an atom with which an unpaired electron is associated has a non-zero nuclear spin, then its magnetic moment will affect the electron. This leads to the phenomenon of hyperfine coupling, analogous to *J*-coupling in NMR, splitting the EPR resonance signal into doublets, triplets and so forth.

3) **Line shape of the spectral line**
   Interactions of an unpaired electron with its environment influence the shape of an EPR spectral line. Line shapes can yield information about the type of the exchange interaction, degree of interaction, rates of chemical reactions *etc*.

4) **Anisotropy**
   The g-factor and hyperfine coupling in an atom or molecule may not be the same for all orientations of an unpaired electron in an external magnetic field. This anisotropy depends upon the electronic structure of the atom or molecule (e.g., free radical) in question, and so can provide information about the atomic or molecular orbital containing the unpaired electron.

The ESR measurements in this thesis were conducted by the technique in which the details and the measurement set-up are given in the Ref. [141].

3.4. Specific heat

Specific heat capacity, also known simply as specific heat, is the measure of the heat energy required to increase the temperature of a unit quantity of a substance by a certain temperature interval. The term originated primarily through the work of the Scottish physicist Joseph Black who conducted various heat measurements and used the phrase "capacity for heat."[142]

The symbols for specific heat capacity are either C or c depending on how the quantity of a substance is measured. In measurement of physical properties, the term "specific" means the measure is a bulk property (an intensive property), whereby the quantity of substance must be specified. For example, the heat energy required to raise the temperature of water by 1K (equal to 1°C) is 4.184J/g - the gram being the specified quantity. This measure would be expressed as $c = 4.184\mathrm{Jg}^{-1}\mathrm{K}^{-1}$.

The specific heat (C) measurements reported in this thesis were conducted by the compensated heat-pulse technique [143] and the details of the measurement device and technique are given in the same reference.

4. Experimental Results and Discussion

4.1. Magnetic properties of betaine adducts with transition metals

As mentioned in the Introduction, the metal-organic compounds studied in this work are materials composed of magnetic centers (transition metal ions) connected via the bridging unit (carboxylate group, diamine group or quinone group), which is a part of an organic molecule and contains large organic ligands that act as spacer/connection between the bridged entities. One of the well-known molecules which can simultaneously act as a bridging unit and spacer is the betaine molecule. In Chemistry, betaine is referred to as neutral chemical compound which consists of a positively charged (cationic) group such as ammonium ion or phosphonium ion and a negatively charged functional group such as the carboxylate group. Due to its electro-negativity (delocalized π-electron), the carboxylate group - on the one end of the betaine molecule - can act as a bridging ligand providing a super-exchange pathway between spin-bearing metal ions, while the large electro positively trimethylammonium part on the other end behaves like a spacer that can separate adjacent low-dimensional structures (see Figure 24).
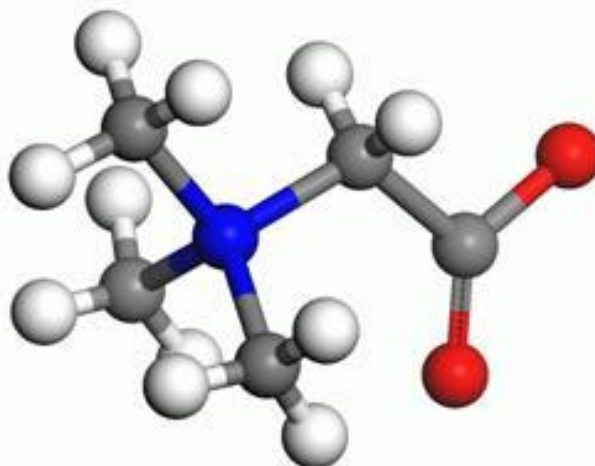
Figure 24: The betaine molecule with a trimethylammonium group on one end and a carboxylate group on the other end of the molecule.

Betaine compounds are represented in all biological systems and have an important function to play in different intercellular processes. Therefore, application of this compound in medicine and pharmacy is multifunctional and widespread.

From the physical point of view, the betain compound has attracted much attention after the discovery of the ferroelectric and antiferroelectric ordering which occurred at low temperature of some betain salts and adducts [144]. An anomalous temperature dependence of

dielectric and elastic properties and ferroelastic behavior, which induce phase transitions in commensurate and incommensurate superstructures, has been reported for a few betaine compounds [144]. Special attention was paid to betaine adducts after the discovery of the antiferromagnetic phase transition in the betaine phosphate [145]. One of the most famous betaine compounds which attracted lot of interests in the 80's is known as betaine calcium chloride dihydrate, $b \cdot CaCl_2 \cdot 2H_2O$ with b = betaine ($C_5H_{11}NO_2$) [146, 147]. Interest in this compound stems from its unusually large number of phase transitions and its sensitiveness to external influence, and has been termed devil's staircase.

4.1.1. Betaine chain compounds $((CH_3)_3NCH_2COO)_3MnMCl_4$ with M = Mn^{2+}, Co^{2+}, Zn^{2+}

The possibility to use betaine as a bridging ligand has attracted some attention in the field of crystal engineering of low-dimensional magnetic systems. A few one-dimensional betaine adducts have been reported up to the present day such as $2b \cdot Cu(NO_3)_2 \cdot Cu(N_3)_2$ [21], certain adducts of betaine with $MnCl_2$ [22, 148, 149] and cadmium salts [23].

In order to search for new low-dimensional magnetic systems with betaine as bridging ligand, the crystallographic group from the Institute of Geosciences (Goethe Universität-Frankfurt) synthesized a few new betaine adducts with manganese(II)-, cobalt(II)- and zinc(II)-chloride, namely $3b \cdot 2MnCl_2$ (BMM) [148, 149], $3b \cdot MnCl_2 \cdot CoCl_2$ (BMC) and $3b \cdot MnCl_2 \cdot ZnCl_2$ (BMZ) [150]. All three compounds are isomorphous and crystallize in the trigonal space group P $\bar{3}$. BMM, BMC and BMZ are 1D magnetic systems consisting of polymeric chains of MnO_6 connected via the carboxylate groups of the betaine molecules, see Figure 26. Within these chains, magnetic interactions between the Mn^{2+} cations (spin 5/2) are expected. The other metal ions (M = Mn^{2+} (spin 5/2), Co^{2+} (spin 3/2), Zn^{2+} (spin 0)) occupy slightly distorted tetrahedral MCl_4 sites, located in between the chains, and filling the holes between the trimethylammonium groups of the betaine molecules.

4.1.1.1. Crystal Synthesis and Structure

BMM, BMC and BMZ were synthesized by dissolving in defined stoichometric ratio betaine monohydrate ($C_5H_{11}NO_2 \cdot H_2O$) and the corresponding metal (II) chlorides $MnCl_2$, $CoCl_2 \cdot 6H_2O$ and $ZnCl_2$, (details of the crystal growth are given in Ref. [151]).

Using the technique of slow evaporation of the solvent, the group of L. Wiehl, succeeded in growing large single crystals of BMM and BMZ of diameters up to 20mm within four weeks at room temperature. Working with growth rates of about 0.5mm/day, single crystals of optical quality (BMM) could be obtained. Small crystals of 3mm in diameter were used as seed crystals. Crystals of BMZ show a pale pink color, BMM is light yellow and BMC is dark blue, see Figure 25. The morphology of BMZ, BMM and BMC consists of a

hexagonal prism and a pinakoid. There is a good cleavage which can be observed parallel to the prism faces. Contrary to the BMZ and BMM, single crystals of BMC were only up to 3mm long and have a long-prismatic form. In the case of BMC, it was difficult to produce larger single crystals due to the problem of controlled growth of the crystals. The problem with the crystal growth occurred due to the high viscosity and the opacity of the saturated aqueous solution of BMC.
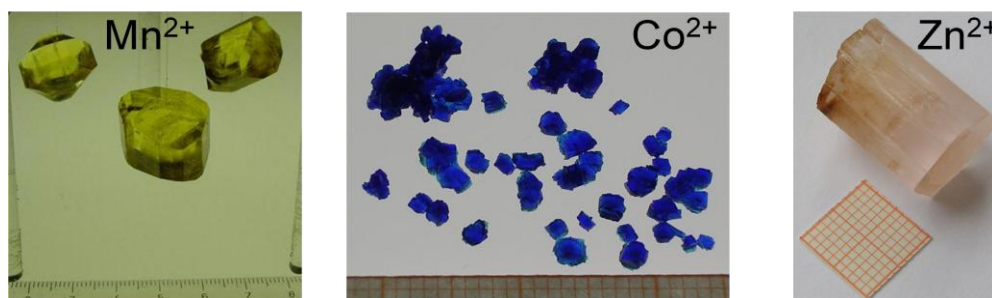

Figure 25: Single crystals of 3b·2MnCl$_2$ (BMM), 3b·MnCl$_2$·CoCl$_2$ (BMC) and 3b·MnCl$_2$·ZnCl$_2$ (BMZ).

The crystal structures of BMZ and BMC [150] were determined by L. Wiehl from the Institute of Geosciences (Goethe Universität-Frankfurt) by single crystal X-ray diffraction, using a four-circle diffractometer Xcalibur3 from Oxford Diffraction with CCD camera and a sealed tube with Mo Kα radiation. The lattice parameters and a detailed structure of the betaine compounds are given in Ref. [151].

According to the structure analysis [148, 149, 150], crystals of BMM, BMZ and BMC contain chains of carboxylate linked $M^{2+}O_6$ octahedra along the [001] direction (Figure 26). From this point of view, the structural features of the betaine compounds are one dimensional (1D) in character. The charge compensation is provided by isolated $[MCl_4]^{2-}$ groups located between the chains. The $[MCl_4]^{2-}$ groups have the shape of distorted tetrahedron. The chains are surrounded by voluminous trimethylammonia tails of the betaine molecules, which are connected with their neighbours via weak van-der-Waals contacts. Magnetic interactions between the metal ions within the chains are realized over the carboxylate bridges (delocalized π-electron), and where the metal-metal distances are of about 4.5Å. However, the metal ions between the chains (in the tetrahedral positions) are too far separated from one another, and from the chains, to participate in magnetic interactions. In BMM, for example, (Mn1, Mn2 in chain, Mn3 in tetrahedra) the respective distances are d(Mn1-Mn3) = 7.68Å, d(Mn2-Mn3) = 7.89Å and d(Mn3-Mn3) = 8.36Å and 9.12Å. In BMC and BMZ the corresponding distances differ by less than 1%.
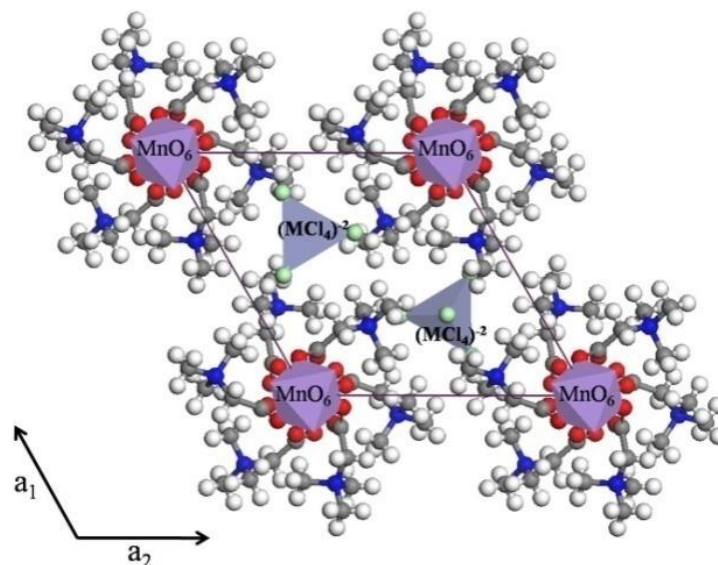
Figure 26: Projection of the unit cell of trigonal 2b·MnMCl$_4$ on the (001) plane in the trigonal-hexagonal setting. The principal bond chains parallel to the 3-fold axis consist of carboxylate-bridged MnO$_6$ octahedra.

The main question, which appears here, is in what quantity metal ions occupy the octahedral and tetrahedral position, in other words which metal ions participate in the construction of chain structures and which metal ions are located in between. Conversely, in BMM where the octahedral and tetrahedral lattice sites are both occupied by manganese, this question has no relevance. The importance of this issue regarding BMZ and BMC is obvious as these are compounds consisting of different metal ions.

Thus for BMZ, Zn occupation in tetrahedral coordination [150] was expected. A possible mixing of Mn and Zn on the octahedral and tetrahedral lattice sites was tested by refining partial site occupation factors in the final states of structure calculations. Here are two possible combinations involved: either the inequivalent octahedral Mn sites are partially occupied by Zn or the tetrahedral Zn sites are partially occupied by Mn ions. In both cases, according to the structural calculations, these occupation factors are refined to values of zero within the statistical error. These findings are compatible with the results of magnetic measurements, which show an amount of about 0.4% uncoupled Mn^{2+} $S = 5/2$ spins, for which it is assumed that they take the tetrahedral site positions.

On the other hand, for BMC the situation is unclear, because the difference of atomic scattering factors between Mn and Co is significantly smaller than for the pair Mn-Zn. According to the structural data analyses, no Co was found in the octahedral positions (within the chains) within the experimental error and a Co occupation factor of at least 90% at the tetrahedral sites was found. Many examples of octahedral and tetrahedral Co^{2+} complexes [152] show that there are no pronounced crystallographic preferences. The deep blue color of the BMC crystals hints at a predominately tetrahedral coordination of Co, as this color is

53

characteristic for many compounds containing $CoCl_4$ or CoO_4 tetrahedra, whereas e.g. the octahedral $[Co(H_2O)_6]^{2+}$ complex colored pink.

4.1.1.2. Magnetic properties

Magnetic measurements were performed in the temperature range between 2K and 300K and fields up to 5T, by using a SQUID system. For temperatures below 2.5K and down to 0.1K the magnetic susceptibility was determined with an *ac*-technique adapted to a $^3He/^4He$ dilution refrigerator. Single crystals of BMZ, BMM and of BMC with masses of 35.0mg (BMZ), 65.0mg (BMM) and 44.7mg (BMC) respectively, were used for the measurements. The rectangular parallelepiped sample of BMM with edge lengths of about 3mm and edges parallel and perpendicular to the 3-fold axis was cut from a large single crystal. All susceptibility data were corrected for a temperature-independent diamagnetic contribution according to Ref. [95].

Figure 27 shows the temperature dependence of the molar magnetic susceptibility χ_{mol} measured on a single crystal of $3b \cdot MnCl_2 \cdot ZnCl_2$ (BMZ). The data have been taken in a magnetic field of 0.5T applied parallel to the *c*-axis (along the polymeric chains of the MnO_6 octahedra). The analysis of the low-temperature susceptibility in the temperature range between 0.1K and 2.5K, shown in the inset of Figure 27, results in a small concentration of uncoupled $S = 5/2$ spins of 0.4%. The corresponding paramagnetic Curie contribution, which dominates the low-temperature part of $\chi_{mol}(T)$, has been also subtracted from the data shown in the main panel of Figure 27. With decreasing temperature $\chi_{mol}(T)$ shows a Curie Weiss-like increase followed by a pronounced maximum around 28K.
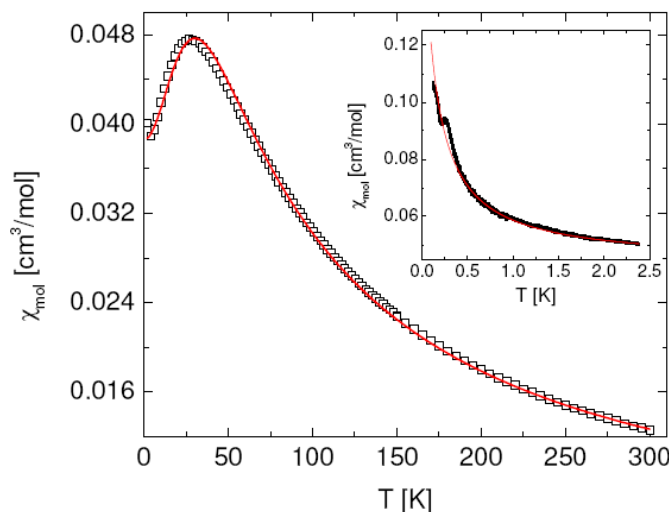
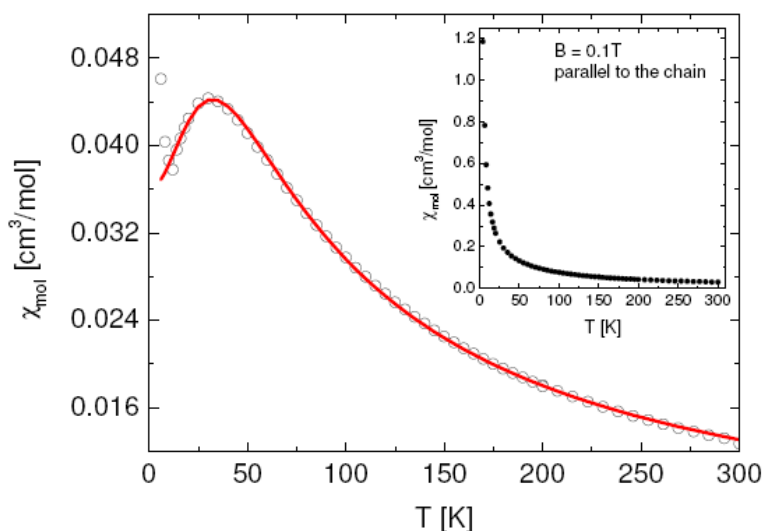Figure 27: Molar magnetic susceptibility χ_{mol} of $3b \cdot MnCl_2 \cdot ZnCl_2$ (BMZ) in a field of $B = 0.5T$ applied parallel to the *c*-axis. The solid line is a fit to the experimental data based on a model for an antiferromagnetic Heisenberg spin chain. Inset: Low-temperature data of χ_{mol} together with a Curie-Weiss fit which accounts for uncoupled Mn^{2+} $S = 5/2$ spins.

An extrapolation of the low-temperature data in the main panel of Figure 27 to $T = 0\text{K}$ yields $\chi_{mol} = 0.0385\text{cm}^3/\text{mol}$. The molar susceptibility of BMZ displayed in Figure 27 is typical for a low-dimensional spin system governed by short-range spin correlations. From the high-temperature part, which can be well described by a Curie-Weiss susceptibility with $S = 5/2$, a g-factor $g = 2$ and an antiferromagnetic Weiss temperature $\theta_W = -42.5\text{K}$, an average antiferromagnetic interaction between neighbouring Mn^{2+} spins is inferred. For a quantitative discussion of the susceptibility, the system was modeled by assuming independent antiferromagnetic Heisenberg chains, consistent with the crystal structure. The corresponding Hamiltonian is given by:

$$H = -2J\sum_i \hat{S}_i \cdot \hat{S}_{i+1} \tag{56}$$

Fitting the data shown in Figure 27 with the expression given by Hiller [153], using the *intra*-chain magnetic exchange coupling constant J between Mn^{2+} ($S = 5/2$) ions and their concentration c as free parameters, a good description (solid line in Figure 27) is achieved with $J/k_B = -(3.0\pm0.15)\text{K}$ and a concentration $c = 99.76\%$ of Mn^{2+} ions in the chain. According to a mean field approach, where only the nearest neighbours z are taken into account, $\theta_W = 2z(S(S + 1))J/3k_B$ allowing for $z = 2$, $S = 5/2$ and $J/k_B = -(3.0\pm0.15)\text{K}$ to obtain $\theta_W = -35\text{K}$ for BMZ [154]. This means that the given value of J is consistent with the Weiss temperature of $\theta_W = -42.5\text{K}$. Possible sources of inaccuracy in the applied fitting procedure are:

   I.   Presence of magnetic impurities with spin states different from $S = 5/2$.

   II.   Finite *inter*-chain interactions.

   III.   Local magnetic anisotropies.

In the inset of Figure 27 is shown the susceptibility for the temperature range $0.12\text{K} < T < 2.4\text{K}$ measured with an *ac*-susceptometer adapted to the ${}^3He\text{-}{}^4He$ dilution refrigerator. For temperatures down to about 0.4K, the data nicely follow a Curie-Weiss-like temperature dependence (solid line). For lower temperatures, however, the susceptibility increases faster than expected from the Curie-Weiss fit and reveals a peak anomaly at 0.25K. Since the susceptibility of uncoupled Heisenberg spin chains is constant (apart from small logarithmic corrections) in this temperature range, it was assumed that this anomaly is due to a long-range antiferromagnetic order as a result of a weak *inter*-chain couplings. According to the Oguchi criterion [155], a Néel temperature of $T_N = 0.25\text{K}$ and the *intra*-chain coupling constant of $|J/k_B| = 3\text{K}$ corresponds to a ratio of *inter*-chain to *intra*-chain coupling by less than $\sim 10^{-4}$ for $S = 5/2$ spin chains. From the low-temperature susceptibility data, it may be concluded that BMZ is a very good realization of an antiferromagnetic $S = 5/2$ Heisenberg spin-chain system.

Unlike the BMZ system discussed above, the magnetic susceptibilities for BMM and BMC are both governed by large paramagnetic contributions. This is not surprising in view of the structural properties of these systems, yielding-as the only difference-magnetically isolated $MnCl_4$ (BMM) or $CoCl_4$ tetrahedra (BMC) which are replaced by non-magnetic $ZnCl_4$ tetrahedra in BMZ. The structural parameters, like bond distances and bond angles within the magnetic spin chains of BMM, BMC and BMZ, are almost identical [150]. Given the similar structural parameters of these compounds, it is possible to analyze the magnetic properties of BMM and BMC in more detail.

In the compound BMM the magnetic contribution of the $MnCl_4$ tetrahedra, which corresponds to 50% of the total amount of Mn^{2+} ions were treated as free spins with $S = 5/2$. By subtracting the corresponding Curie susceptibility from the raw data, the susceptibility originating from the chains of coupled MnO_6 octahedra were obtained, see Figure 28. The resulting $\chi_{mol}(T)$ is very similar to the data for BMZ shown in Figure 27. Employing the same fitting procedure as for the latter system yields, within the error, the same antiferromagnetic *intra*-chain coupling constant $J/k_B = - (3.0\pm0.15)K$ for BMM.

Figure 28: Molar magnetic susceptibility χ_{mol} of 3b·2$MnCl_2$ (BMM) in a field of $B = 0.1T$ applied parallel to the *c*-axis after subtracting the paramagnetic contribution due to magnetically isolated Mn-Cl tetrahedra. The solid line is a fit to the experimental data based on a model of an antiferromagnetic Heisenberg spin chain. Inset: The raw data before subtraction.

In the case of the BMC compound, the exact analysis of the magnetic data is difficult to obtain due to the presence of the Co ions. Firstly, depending on the Co ion coordination environment, the crystal field splitting of the Co^{2+} ions can give rise to a temperature-dependent contribution to the susceptibility. Secondly, the site-exchange between Mn and Co ions may have occurred within the uncertainty of ~ 10% implied in structural analysis.

Assuming that at least 90% of the tetrahedral sites are occupied by the Co^{2+} ions (a value consistent with X-ray diffraction experiments), whereas the Mn^{2+} ions are predominantly in an octahedral coordination, the room-temperature susceptibility would correspond to an effective magnetic moment for the Co^{2+} ions of $\mu_{eff} \sim 4.6\mu_B$. Such a value is compatible with Co^{2+} in a tetrahedral coordination [156]. Under these conditions, the effective moment of the Co^{2+} ion is nearly temperature independent, which enables us to perform an analysis similar to that employed for BMM. As a result it was found that in BMC the octahedrally coordinated Mn^{2+} ions forming the spin chains are also coupled antiferromagnetically with $J/k_B = - (3.0 \pm 0.3)K$, whereas the $CoCl_4$ tetrahedra are magnetically isolated.

4.1.1.3. Summary

The three isomorphic compounds $3b \cdot MnCl_2 \cdot MCl_2$ with M = Mn^{2+}, Co^{2+}, Zn^{2+} have three different cation sites, two in octahedral and one in tetrahedral coordination, in the ratio 1:1:2. Isomorphic replacement takes place on the tetrahedral site of the compound BMZ with Zn^{2+} and in BMC with Co^{2+} ions, leaving the octahedral chains occupied by manganese-Mn^{2+} in all three compounds. The features that are common for all three betaine compounds are the chains of carboxylate-bridged Mn^{2+} ions ($S = 5/2$) which are antiferromagnetically coupled. The second metal in the isolated MCl_4 tetrahedral position influences the magnetic properties of Mn^{2+} chains considerably, depending on its spin state (for Mn $S = 5/2$, for Co $S = 3/2$ and for Zn $S = 0$). This influence can be seen as an additional paramagnetic contribution of isolated spins in relation to the contribution of the coupled spins in the chain. Thus, the compound BMZ is the only one where the magnetic properties of the chains are seen in pure form. In BMM and BMC, on the other hand, the chain contribution could be modeled after subtracting the paramagnetic contribution of the isolated spins in the MCl_4 tetrahedra.

An essential point for the magnetic model calculations was the occupation of metal octahedral and tetrahedral sites. A possible mixing of different spin states on octahedral and tetrahedral lattice sites could not be modeled from the magnetic data alone, but had to be backed up by the knowledge of the chemical composition. For BMZ there is a clear chemical preference for MnO_6 in the octahedral position and $ZnCl_4$ in the tetrahedral position. The quantum mechanical calculations [151] show that it is energetically very unfavorable to incorporate Zn into the octahedral sites in BMZ. This result is confirmed by X-ray diffraction, which is able to deliver significant occupation factors in the Mn-Zn case. For BMC, on the other hand, no pronounced chemical preferences exist. X-ray diffraction can only narrow the extent of disorder down to less than 20%. This limit is further reduced by the results of magnetic measurements, which are compatible only with an amount significantly less than 10% Co in the magnetically coupled Mn chain.

The magnetic properties of all three betaine compounds BMZ, BMM and BMC are well described by the model of independent Heisenberg spin chains, formed by Mn^{2+} ions with $S = 5/2$ which are all in octahedral coordination. The weak antiferromagnetic *intra*-chain

coupling of $J/k_B \sim$ -3.0K, for all three compounds, is provided by the carboxylate groups at the ends of the betaine molecules. The metal ions, located on the tetrahedral positions in between the chains, are magnetically isolated and do not influence the magnetic properties of the spin chains. This explains the similar *intra*-chain exchange interaction of BMZ, BMM and BMC and is consistent with their structural properties.

4.1.2. Betaine trimer system $((CH_3)_3NCH_2COO)_2 \cdot 3CuCl_2 \cdot 2H_2O$

4.1.2.1. Crystal Synthesis and Structure

The studied compound was synthesized by E. Haussühl from the Institute of Geoscience (Goethe University Frankfurt am Main). The raw material was prepared by the reaction of stoichometric quantities of betaine hydrate and copper chloride in pure water:

$$3(CH_3)_3NCH_2COO \cdot H_2O + 2CuCl_2 + 2H_2O \Rightarrow b_3(CuCl_2)_2 \cdot 2H_2O$$

For the crystallographic characterization and for the purpose of obtaining seed crystals, single crystals were grown having a diameter of a few mm. Larger crystals having optical quality and typical dimensions about 20 x 20 x 20mm were grown from aqueous solutions by standard methods (controlled evaporation at about 290K, Figure 29) in air thermostats. The growth rate reached about 0.5mm/day. The progress of crystal growth was difficult to control due to the very high viscosity and the opacity of the saturated aqueous solution in $b_3(CuCl_2)_2 \cdot 2H_2O$. The crystals are stable in air at room temperature up to humidity of about 70%.
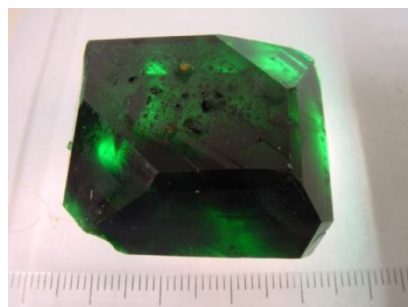
Figure 29: Single crystal of $2b \cdot 3CuCl_2 \cdot 2H_2O$.

The crystal structure of $2b \cdot 3CuCl_2 \cdot 2H_2O$ is built up of centro-symmetric trimeric molecular units of the form $OCl_2Cu–b–CuCl_2–b–CuCl_2O$, as can be seen in Figure 30. The crystal consists of neutral, trinuclear betaine-$CuCl_2$-water complexes which are connected by hydrogen bonds and van der Waals interactions. The copper ions are linked pairwise by the carboxylate groups of two betaine molecules. All Cu^{2+} ions show a nearly planar quadratic environment, indicating that the unpaired electron is located in the d_{x2-y2} orbital. The central Cu1 ion of the trimer is coordinated by two Cl ions in trans position ($d = 2.341$Å) and two oxygen atoms ($d = 1.924$Å) of two different betaine molecules. In addition, semi-coordination between the magnetic centres exists within the trimer via the Cl atoms. The outer Cu2 ions are coordinated each by the second oxygen atom ($d = 2.007$Å) of the bridging betaine carboxylate group, two Cl ions ($d = 2.227$-2.243Å) in cis position and a water molecule ($d = 1.975$Å).

Therefore, the central Cu1 ion has 4+2 coordination and the outward Cu2 ions exhibit only 4+1 coordination.
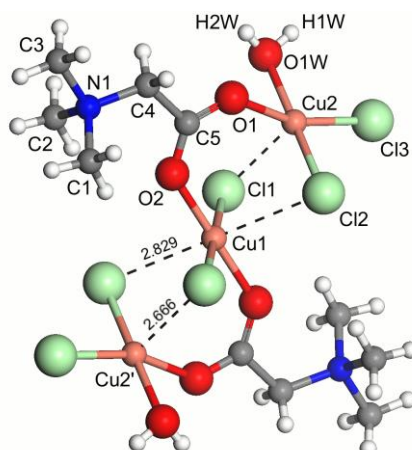

Figure 30: Molecular structure of the trinuclear complex 2b·3CuCl$_2$·2H$_2$O with an atom numbering scheme. The Cu centers are bridged by carboxylate groups O(1)-C(4)-O(2) at the end of the betain b molecules (b = (CH$_3$)$_3$NCH$_2$COO). Dotted lines indicate the distance between Cu and nearest neighbor atoms.

In the *ab*-plane ((001) plane), a two-dimensional network of hydrogen bonds from water molecules to chlorine ions connect each trimer with four other trimers in a nearly quadratic arrangement with distances d(O1W…Cl1) = 3.107Å and d(O1W…Cl2) = 3.130Å and O-H-Cl angles of 167° and 148°, respectively. There are two different hydrogen bridges involved connecting the trimers, namely the path Cu2-O1W-H2W...Cl1-Cu1 with a total length of 7.439Å and the path Cu2-O1W-H1W...Cl2-Cu2' with a total length of 7.441Å. Figure 31 shows such a layer of H-bonded trimers.
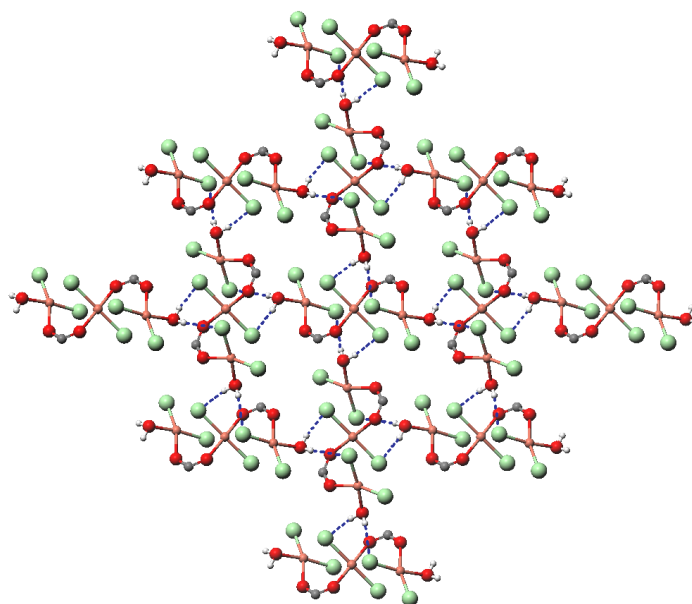
Figure 31: The Cl-H bonds (dashed lines) of H$_2$O molecules mediate trimer-trimer interactions of 2b•3CuCl$_2$•2H$_2$O in the *ab*-plane. The bond lengths are 2.309 and 2.407Å.

The layers are connected by weak van der Waals bonds along the *c*-axis. The betaine molecules have been omitted for clarity with the exception of the carboxylate groups. The large tails of the betaine molecules are orientated essentially in the *c*-direction. The shortest atomic contacts between neighbouring layers are C-Cl contacts at a distance of 3.67Å.

4.1.2.2. Magnetic properties

Temperature dependent (2-300K) magnetic susceptibility and isothermal magnetization measurements on the single crystal of $2b \cdot 3CuCl_2 \cdot 2H_2O$ ($m = 46.29$mg) were carried out in fields $B \leq 5T$. All data are corrected for the temperature-independent diamagnetic core contribution according to Ref. [95] and the sample holder contribution. The sample holder contribution of $M_{sample\ holder} = 8.6 \times 10^{-6}$ emu has been determined by analyzing the high-temperature magnetic behavior.

Figure 32 shows the susceptibility $\chi(T) = M(T)/B$ of the $2b \cdot 3CuCl_2 \cdot 2H_2O$ compound in a form $\chi_{mol}^{-1}(T)$ vs. *T*, where *M* denotes the magnetic moment of the sample.
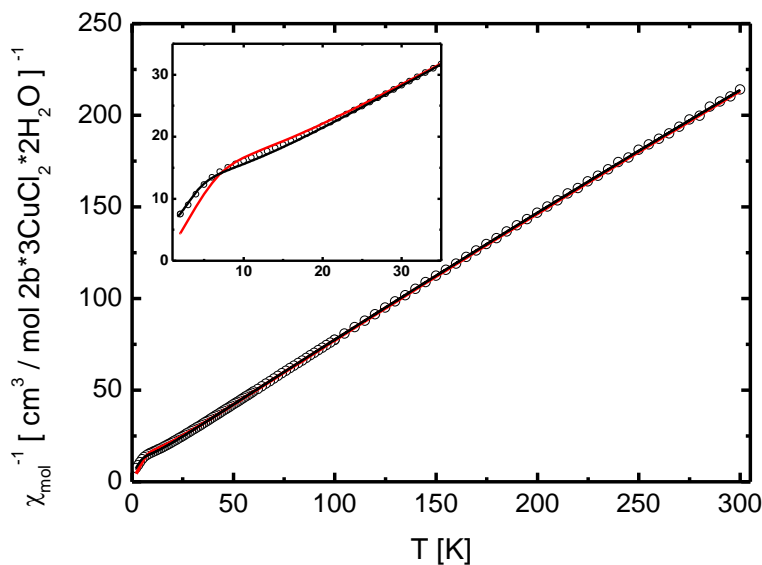
Figure 32: The inverse magnetic susceptibility of the compound $2b \cdot 3CuCl_2 \cdot 2H_2O$ in the temperature range 2-300K. Data were taken at a magnetic field of 0.05T. The red solid line represents the best fit for the model of isolated, linear $S = \frac{1}{2}$ trimers with an antiferromagnetic *intra*-trimer exchange interaction $J/k_B = -20(1)$K and $g = 2.2(1)$. The black solid line corresponds to the best fit for the model of antiferromagnetically coupled trimers with *intra*-trimer coupling $J/k_B = -15$K and an *inter*-trimer coupling of strength $J_a/k_B = J_b/k_B = -4$K.

The data were found to be reversible upon cooling and heating with no indications for hysteretic behavior. No sign for long-range magnetic ordering was found in the temperature range under investigation. The inverse magnetic susceptibility $\chi_{mol}^{-1}(T)$ in Fig. 32 shows two linear regimes corresponding to two distinct Curie-Weiss-like temperature dependences $\chi_{mol} = C_m/(T-\Theta)$, with different Curie constants and Weiss temperatures.

In the high temperature range 300-100K, the sample shows a simple Curie behavior, and the best fit to the experimental data is achieved with a Curie constant $C_{HT} = 1.390\text{cm}^3\text{Kmol}^{-1}$ and a Weiss constant $\Theta_{HT} = -11.8\text{K}$. The Curie constant is consistent with the presence of three Cu(II) ions per molecule, giving a perfect agreement for a spin-only value $1.361\text{cm}^3\text{Kmol}^{-1} = 3\times0.453\text{cm}^3\text{Kmol}^{-1}$ for $g = 2.2$. The negative Weiss constant indicates the presence of antiferromagnetic spin-spin interactions in the high-temperature range.

As seen in Figure 32, the slope of the χ_{mol}^{-1} curve changes around 7K. Since χ_{mol}^{-1} is still approximately linear below 7K, one can fit the low-temperature data with the Curie-Weiss function. The best result is achieved for $C_{LT} = 0.608\text{cm}^3\text{Kmol}^{-1}$ and $\Theta_{LT} = -2.8(2)\text{K}$. A distinctly larger slope of the χ_{mol}^{-1} in the low-temperature range and a smaller Curie constant indicate a reduced magnetic moment at low temperatures.

The susceptibility of 2b•3CuCl$_2$•2H$_2$O is reminiscent of that observed in a variety of isolated trimer systems [157-160]. This suggests that the dominant magnetic coupling is provided by an *intra*-trimer Cu-Cu exchange interaction *J*, where the three linked Cu(II) centers were considered as a linear three-spin-system with two equivalent exchange interactions occurring between the carboxilate bridged ions, Cu(2)-O(1)-C(4)-O(2)-Cu(1) and Cu(1)-O(2)-C(4)-O(1)-Cu(2), see Figure 30.

In a first approach, isolated trimers with a uniform isotropic Heisenberg *intra*-trimer exchange interaction *J* and an isotropic *g*-factor will be considered, described by the spin Hamiltonian given in Equation 13. The trimer has a simple spectrum with an $S = \frac{1}{2}$ ground state with energy - *J* (in zero field) with the spin-down state given by $(|\uparrow\downarrow\downarrow>-2|\downarrow\uparrow\downarrow>+|\downarrow\downarrow\uparrow>)/\sqrt{6}$. The first excited state has zero energy and also $S = \frac{1}{2}$ with the spin-down state given by $(|\uparrow\downarrow\downarrow>-|\downarrow\downarrow\uparrow>)/\sqrt{2}$. The highest energy state has $S = 3/2$ and energy $J/2$. The resulting expression for $\chi_{mol} T$ is given by the Equation 15. The magnetization of the isolated linear trimer is given by Equation 16 (see Ref. [160]).

In the limit $J\rightarrow\infty$ or $T \ll J/k_B$, that is, $x\rightarrow0$, the trimer is in an $S = \frac{1}{2}$ state and $M(T,h)$ reduces to the $S = \frac{1}{2}$ Brillouin function. For vanishing exchange coupling *J* or $T \gg J/k_B$, that is, $x\rightarrow1$, the spins of the trimer are independent and $M(T,h)$ is 3 times the $S = \frac{1}{2}$ Brillouin function.

Fitting the inverse susceptibility data in Figure 32 for the whole temperature range 300-2K, a reasonably good agreement (solid line Figure 32) was found for an antiferromagnetic *intra*-trimer interaction of $J/k_B = -20(1)\text{K}$. The simple isolated-trimer model describes the major part of the experimental data quite well, especially the increase of the slope of $\chi_{mol}^{-1}(T)$ for temperatures above 10K, as well as the reduction of the Curie constant for temperatures lower than 7K. However, a closer look at the low-temperature part in Figure

32 reveals deviations of the model curve from the experimental data, indicating the presence of additional, weaker *inter*-trimer interactions (intermolecular exchange interaction) and a more complex ground state of the system.

A finite trimer-trimer interaction can be expected because of the presence of water molecules, which provide exchange paths between the Cu(II) atoms in the trimer and the Cu(II) atoms in adjacent trimers, see Figure 31. Weak trimer-trimer interactions can arise through the water molecules H_2O and neighbor trimers Cl ions; this exchange path involves rather long H-Cl bonds ranging from 2.309 to 2.407 Å. Since the Cu-O-H-Cl-Cu paths range from 4.555 to 4.653 Å, their coupling strength are expected to be weak. At low temperatures, this coupling can nonetheless become important and therefore these trimer-trimer interactions were included in a refined model derived by N. Hasselmann by introducing the coupling constants J_a and J_b that link the linear trimer centers within the molecule with neighbor trimers via the water molecules and Cl ions. This results in a rather interesting model of interacting trimers with the topology shown in Figure 33. Details of the model are presented in [161]. It was assumed that both J_a and J_b are antiferromagnetic (positive) and that they are much smaller than *J*. Both of these assumptions are validated by a comparison with the experimental data, as shown below.
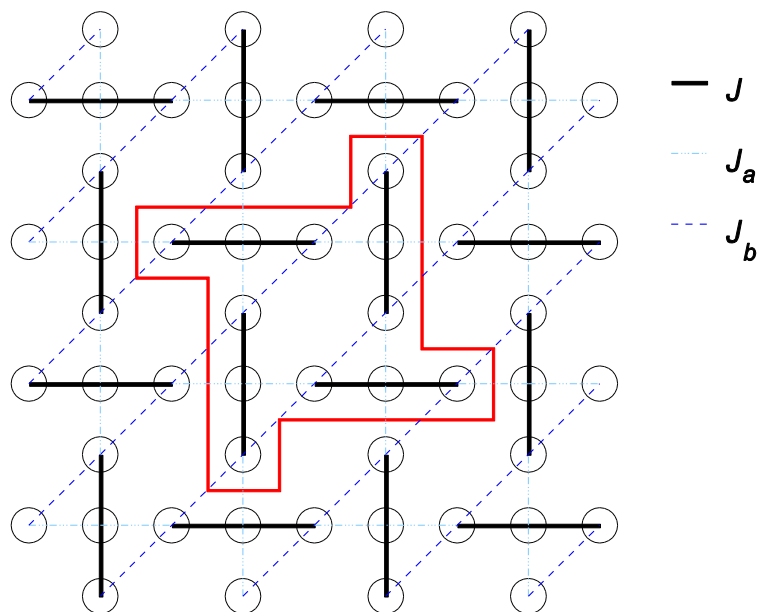
Figure 33: Effective interacting-trimer model with *intra*-trimer coupling *J* and two types of *inter*-trimer couplings J_a, J_b. The central region was used in the numerical calculations and contains four coupled trimers (with periodic boundary conditions).

At low temperatures $k_B T << J$ the trimers should be mostly in their ground state. Since the trimer ground state has $S = ½$, the system can, for low temperatures, be described by a reduced low-energy model of coupled $S = ½$ spins, one for each trimer. The trimer model

considered here reduces then to a square lattice of $S = \frac{1}{2}$ spins. If the *inter*-trimer interactions J_a, J_b are much smaller than the *intra*-trimer interaction J, one can use perturbation theory to calculate the effective exchange parameters for the square lattice model. First-order perturbation theory reveals that the dominant effective exchange interaction of the trimers is then a nearest-neighbor coupling of strength $J_{eff} = (4/9) (J_b - J_a/2)$. The interesting fact here is that even if all bare spin interactions are antiferromagnetic, the low-energy effective interaction among the trimers could become ferromagnetic when $J_b < J_a/2$ (a similar dependence of the effective trimer coupling on the bare exchange parameters has been reported in [159] for the case of trimer chains). The low-energy states, which result from the 12-spins model forming a plaquette of trimers, are shown schematically in Figure 34. In the corners, the energy levels spectra of the decoupled four trimers are shown, which consist of an $S = \frac{1}{2}$ ground state, an $S = \frac{1}{2}$ excited state and an $S = 3/2$ state at energy $3J/2$ above the ground state. The weak coupling of the trimers via $J_{a/b}$ mixes the $S = \frac{1}{2}$ trimer ground states and, to leading order in perturbation theory, leads to the low-energy states shown in the center of Figure 34. For the application to the present model and in order to reduce the number of adjustable parameters to a minimum, the two *inter*-trimer coupling constants were set $J_a = J_b$.
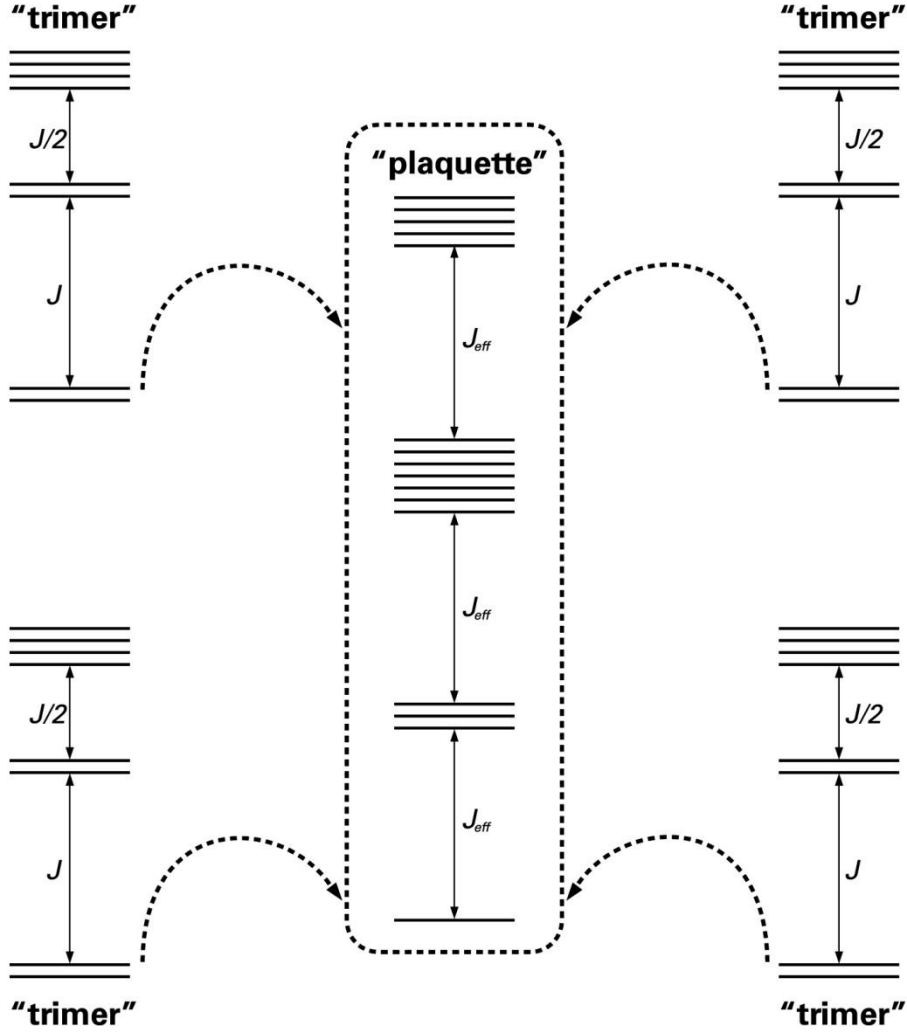
Figure 34: The *intra*-trimer coupling yields at low energies an effective theory of coupled $S = \frac{1}{2}$ states. Leading-order perturbation theory predicts that the ground state of the plaquette is a singlet and the lowest excited states are $S = 1$ triplets separated by J_{eff} from the ground state (assuming here $J_{eff} > 0$). At another energy J_{eff} higher are two degenerate $S = 1$ triplets and an $S = 0$ singlet. The highest-energy state with all trimers still in their ground state is the $S = 2$ ferromagnetic state.

For a four-spin plaquette, the most general $S = \frac{1}{2}$ Hamiltonian can be written as $\hat{H} = \hat{H}_1 + \hat{H}_2 + \hat{H}_3 + \hat{H}_4$ [162], with:

$$\hat{H}_1 = j_1(\hat{S}_1 \cdot \hat{S}_2 + \hat{S}_2 \cdot \hat{S}_3 + \hat{S}_3 \cdot \hat{S}_4 + \hat{S}_4 \cdot \hat{S}_1), \tag{57}$$

$$\hat{H}_2 = j_2(\hat{S}_1 \cdot \hat{S}_3 + \hat{S}_2 \cdot \hat{S}_4), \tag{58}$$

$$\hat{H}_3 = j_3((\hat{S}_1 \cdot \hat{S}_2)\cdot(\hat{S}_3 \cdot \hat{S}_4)+(\hat{S}_1 \cdot \hat{S}_4)(\hat{S}_2 \cdot \hat{S}_3)-(\hat{S}_1 \cdot \hat{S}_3)\cdot(\hat{S}_2 \cdot \hat{S}_4)), \tag{59}$$

$$\hat{H}_4 = j_4(\hat{S}_1 \cdot \hat{S}_3)\cdot(\hat{S}_2 \cdot \hat{S}_4). \tag{60}$$

The first term - $\hat{H}_1$ is the nearest-neighbor exchange, the second term - $\hat{H}_2$ describes next-to-nearest-neighbor exchange, the third term - $\hat{H}_3$ arises from a four-spin cyclic exchange and the last term - $\hat{H}_4$ describes a four-spin exchange via the diagonals of the plaquette.

Comparing the evolution of the lowest eigen-energies, done by exact diagonalization calculation, and a first-order perturbation theory calculation, the deviation between these methods is observable even for small values of J_a, $0.1 \leq J_a/J$. In this case, higher-order perturbation terms are necessary to account for the difference. Inclusion of next-to-nearest-neighbor interactions and four-spin interaction processes can account for the difference indicating the importance of these exchange processes in the magnetic behavior of the system (details of the calculations are given in the Ref. [161]). The most important findings in these calculations are the energy limit up until which the system can be considered as a plaquette of effective $S = \frac{1}{2}$ spins and exchange processes, which may influence the behavior of the system. According to the theoretical calculation, the energy limit of the plaquette model is $J_a/J = 0.4$. Near the energy $J_a/J = 0.4$ and for higher values, new energy states appear and it is not possible to consider the system as a plaquette of effective $S = \frac{1}{2}$ spins. For the case $J_a = J_b$ the dominant interaction is the nearest-neighbor interaction and it drives the system to a transition from an antiferromagnetic to a ferromagnetic state. Around the transition point, the diagonal four-spin exchange becomes stronger but remains small compared to the nearest-neighbor interaction. From this point of view, this system would be an ideal model system to probe the effect of the diagonal four-spin exchange processes at low temperatures, processes not known so well as those of the next-to-nearest-neighbor exchange and four-spin cyclic exchange processes, which are well investigated [163].

As demonstrated in Figure 32 the influence of the *inter*-trimer coupling on the susceptibility is small and deviations from the pure trimer model become visible only at low temperatures. To visualize the effect of a weak *inter*-trimer exchange interaction on the susceptibility, a representation $\chi_{mol}T$ versus T is used in Figure 35. The figure shows the best fit for weakly coupled trimers with an *intra*-trimer exchange interaction $J/k_B = -15K$ and a weak antiferromagnetic *inter*-trimer interaction $J_a/k_B = J_b/k_B = -4K$, while the red line indicates the results for the isolated-trimer model with $J/k_B = -20K$. As has already been seen in the susceptibility data in Figure 32, Figure 35 shows that the incorporation of a small but finite *inter*-trimer exchange interaction improves the fit considerably at low temperatures, although small deviations of the model curve from the data are still visible. As was discussed by Zaspel *et*. *al*. [159], the low-temperature behavior of such a generalized coupled-trimer model depends sensitively on the *inter*-trimer coupling constants.
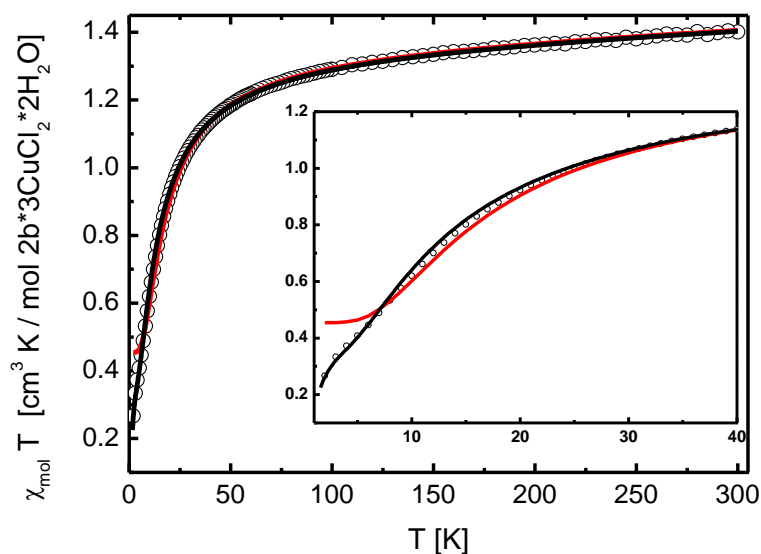
Figure 35: Magnetic susceptibility data of 2b•3CuCl$_2$•2H$_2$O taken at a field of 0.05T plotted as χ_{mol} T versus T. The inset shows the low-temperature behavior on expanded scales. The red line corresponds to the best fit for the isolated linear trimer model with J/k_B = -20K; the solid line represents the result of the model for antiferromagnetically coupled trimers with J/k_B = -15K and $J_a/k_B = J_b/k_B$ = -4K.

The coupling constants derived from fits to the susceptibility are further supported by the results of the isothermal magnetization measurements, see Figure 36. Besides the experimental magnetization data, Figure 36 also shows the calculated magnetization curves for the model of isolated trimers (red lines) and antiferromagnetically coupled (black lines) trimers, with the coupling geometry displayed in Figure 33 and the same coupling constants as described above.
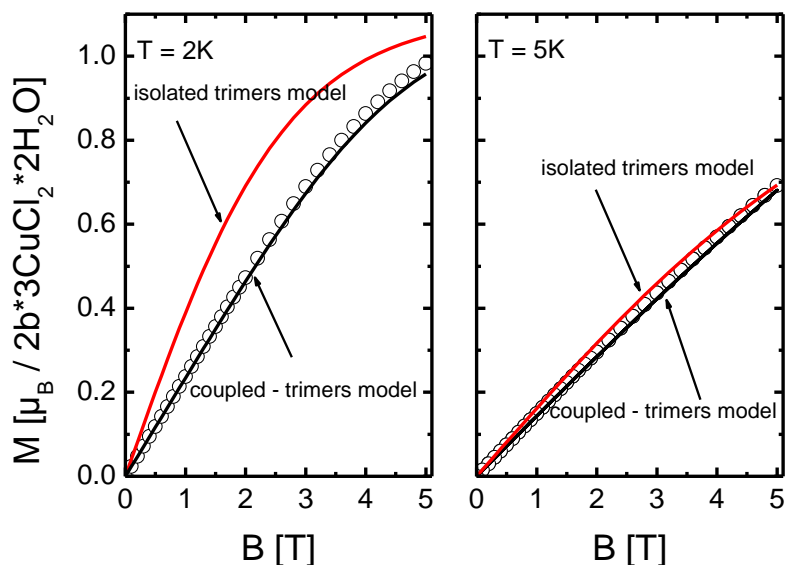
Figure 36: Isothermal magnetization measurements in dc fields up to 5T at different temperatures as indicated in the figure. The red and black lines correspond to the model curves for isolated and antiferromagnetically-coupled trimers, respectively, with the coupling parameters given in the text.

Below 5K, the isolated-trimer model clearly deviates from the experimental data and *inter*-trimer interactions become important. A very reasonable description of the magnetization curve at 2K is achieved with the model of antiferromagnetically-coupled trimers which describes the data well for all measured fields up to 5T.

4.1.2.3. Summary

The trinuclear compound $2b \cdot 3CuCl_2 \cdot 2H_2O$ consists of Cu^{2+} ions that build linear trimers via the carboxylate groups, which are connected over the strong hydrogen bonds O-H$\cdots$Cl and make a quasi-2D system. The low-dimensional 2D character of the compound is also visible in the magnetic measurements (magnetic susceptibility and isothermal magnetization) which show all the signatures of low dimensionality. Using an appropriate theoretical model developed by N. Hasselmann [161] to describe this quasi-2D system, it was possible to determine *inter*-trimer and *intra*-trimer interactions. In this way the *intra*-trimer interaction has been estimated to $J/k_B = -15K$ and the *inter*-trimer to $J_{a,b}/k_B = -4K$. The value of the *intra*-trimer interaction turns out to be relatively small considering that Cu^{2+} ions have a planar coordination, see Figure 35. Taking into account the results of a structural analysis, it can be seen that the Cu^{2+} coordination planes are not coplanar, *i.e.* they are tilted agains each another. Due to this mutual tilting, a certain reduction of the *intra*-trimer interaction is

expected. However, the values of *inter*-trimer interactions are unexpectedly large considering that the trimers are linked via hydrogen bonds. From investigations carried out on purely organic materials with magnetic character, it is known that in addition to linking magnetic ions, hydrogen bonds may be responsible for the magnetic interaction *i.e.* they can take part in the process of exchange. In this case the exchange through these links can be of the order of a few degrees Kelvin [164, 165]. In taking this fact into account, the relatively high value of the *inter*-trimer interaction can be understood.

According to the trimer topology which has a 2D character, the system could be described by a simplified plaquette model. On the basis of this model using low-order perturbation theory, we came to two very interesting conclusions:

(1) The system can have ferromagnetic interactions between the trimers in the case $J_b < J_a/2$, although the interactions J_a and J_b have antiferromagnetic character.

(2) For the energies $J_a/J \geq 0.4$ ($J_a = J_b$), the system cannot be described by the plaquette model because the processes of inter cluster (plaquette) interaction become relevant.

Due to the above-mentioned characteristics, the trinuclear compound $2b \cdot 3CuCl_2 \cdot 2H_2O$ presents a very interesting low-dimensional spin system. By model calculations on an effective trimer model parameter ranges have been identified where the four-spin diagonal-exchange processes become dominant which allow this lesser-known processes to be studied in detail. The system might be brought into the parameter range of interest either by chemical modification of the baseline compound or by the influence of some external parameters such as hydrostatic pressure.

4.2. Hydroquinone-bridged Polymer-TK91

Low-dimensional quantum magnets, exposed to strong magnetic fields, reveal a variety of fascinating phenomena. An example of high current interest is the possibility to realize a Bose-Einstein condensation of magnetic excitations in 3D coupled spin-dimer systems [166]. As mentioned in the Introduction and Chapter 2, the spin-dimer systems have a finite spin gap Δ between the non-magnetic ground state and the lowest excited state. The spin gap can be reduced by applying an external magnetic field. When the applied magnetic field is higher than a critical field, $B_c = \Delta/g\mu_B$, the spin gap closes and a 3D long-range magnetic ordering develops. This field-induced phase transition has been interpreted as a Bose–Einstein condensation of magnons [54]. This phenomenon corresponds to a field-induced phase transition into a canted AFM state in the original spin system. The suggestion that BEC of magnons could be studied in coupled spin-dimer systems has stimulated extensive experimental and theoretical studies of such systems.

4.2.1. Crystal syntheses and structure

In an attempt to search for new quantum-spin systems with interesting spin topologies, G. Margraf and collaborators from the Institute for Inorganic Chemistry (Goethe University) have recently synthesized novel Cu-containing coordination polymers by using hydroquinone-derived linkers to connect the magnetic Cu(II) ions [167]. Attaching different ligands to the ‚side arms'of the core structure of the hydroquinone derivatives, see Figure 37, one can modify both *intra*-dimer and *inter*-dimer interaction of the system.
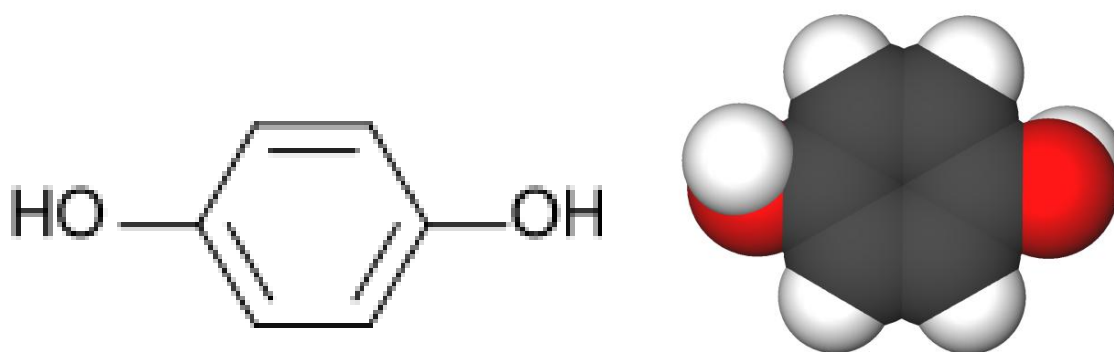
Figure 37: Chemical structure of the hydroquinone (quinol, benzene-1, 4-diol) linker.

The system can be tailored to the desirable magnetic properties by choosing various charge-balancing anions in the synthesis process. A family of novel spin-dimer systems with different magnetic properties was realized by this design strategy [17, 167]. A member of the

family, $C_{36}H_{48}Cu_2F_6N_8O_{12}S_2$ (labeled TK91 henceforth), shows the most intriguing properties. Details about synthesis one can find in the Ref. [18].

The compound is found to be a triclinic system and belongs to the $P\bar{1}$ space group. The crystallographic inversion center of symmetry lies in the midpoint of the central six-member carbon ring. The crystal has a polymeric structure along the crystallographic *a*-axis which corresponds to the long axis of the needle-shaped crystal of red-brown color. The crystal structure of TK91 is shown in Figure 38. The Cu(II) ions have a distorted octahedral coordination environment and are bridged by hydroquinone linkers to form dimer units. The equatorial plane is formed by the atoms N1, N2, O1 and O2 (DMF). The apical position have a Cu-O3 (DMF) bond of 2.565(2)Å and a Cu-O1 bond of 2.434(1)Å to a neighboring dimer. Neighboring dimers are connected via long axial Cu-O1 bonds and there are 13 of intermolecular hydrogen bonds, with H-O distances between 2.51Å and 2.75Å, and three H-F distances between 2.56Å and 2.75Å providing potential paths for *inter*-dimer magnetic exchange interaction (for details of the crystal structure, see Ref.[18]).
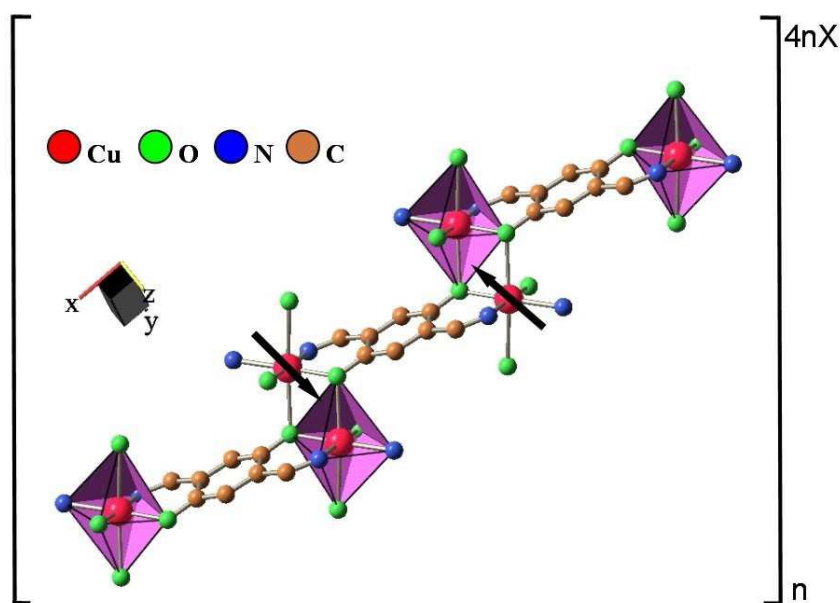
Figure 38: Schematic diagram of the crystal structure of TK91. The charge-balancing anion $CF_3SO_3^-$ is labeled *X* in the diagram. The crystallographic *a*-axis corresponds to the long axis of the needle-shaped crystal.

4.2.2. *Ab initio* calculations

Preliminary *ab inito* calculations, performed by the group of Prof. Roser Valenti at Frankfurt University, suggested that TK91 is a weakly coupled 3D spin-dimer system [17, 168]. The calculations were based on the generalized gradient approximation (GGA) [169]. For this purpose the linearized muffin tin orbital method (LMTO) was used, based on the

Stuttgart TBLMTO-47 code [169]. The aim was to get a reliable estimate of the nature of the interaction paths. In addition, the tight-binding-down-folding procedure [170] was applied, which obtains the effective Cu_d-Cu_d hopping parameters by down folding all the degrees of freedom in the band structure calculation other than the Cu_d bands at the Fermi level. According to the calculations, the strongest interaction path $t = 34$ meV is between coppers that are linked by the hydroquinone group and are as far apart as 8.4Å, while the hopping between nearest neighbor coppers at a distance of 3.4Å is almost zero. The next relevant hopping term t' is between fifth nearest neighbor Cu ions along the *a*-direction $t' = 23$meV. The main conclusion from these calculations was that the Cu-dimers contain the hydroquinone as bridging ligand, and these dimers are weakly coupled within the 3D structure. An estimate of the *intra*-dimer coupling can be obtained by considering the expression $J = 4t^2/U_{eff}$ with t being the *intra*-dimer hopping integral. This procedure yields $J/k_B \sim 17$K which overestimates the experimental value somewhat.

Refined *ab initio* Density Functional Theory (DFT) calculations together with N-th order muffin tin orbital calculations (NMTO) revealed that the *intra*-dimer and *inter*-dimer interactions have different values. The calculated Cu-Cu hopping parameters indicate that the Cu ions, linked by the modified hydroquinone group, have the strongest coupling and form dimers. A perturbative estimate of the antiferromagnetic contribution to the exchange constants, J, yields an *intra*-dimer interaction J_d/k_B of about 13.4K. These dimers are weakly coupled in the *ac*-plane via t_1 and t_2, corresponding to *intra*-plane interactions J_1 and J_2, respectively, with $J_1/k_B \approx J_2/k_B \approx J_{||}/k_B = 1.4 - 1.7$K. The resulting spin-spin interaction network has the topology of a 2D distorted honeycomb lattice, see Ref. [171]. Knowing that the exchange couplings obtained by this procedure are usually overestimated values, the very small *inter*-layer coupling $J_\perp/k_B$ of 0.1K calculated in the same way suggests that the *ac* planes in TK91 are almost decoupled.

4.2.3. DC susceptibility measurements

DC magnetic susceptibility measurements ($\chi = M/B$) were conducted on single crystalline samples of TK91 down to 2K and in an applied magnetic field up to 5T.

In Figure 39 the magnetic susceptibility χ of TK91 is shown for an applied magnetic field of 0.1T as a function of temperature. The magnetic susceptibility $\chi(T)$ shows a peak at $T \sim 6$K then it drops and extrapolates to zero at 0K, suggesting a spin gap. Moreover, $\chi(T)$ can be fitted nicely by an isolated-dimer model with $g = 2.1$ (obtained from the ESR measurements) and a small Curie contribution to account for isolated impurity spins. The values of the *intra*-dimer coupling are found from this fit to be $J_d/k_B = 9.4(2)$K. The $S = \frac{1}{2}$ impurity concentration is estimated to be less than 1%, showing the high quality of the crystals studied. In the absence of any *inter*-dimer interaction, the magnetic field required to close the spin gap would be $B_c = \Delta/g\mu_B \approx 6.6$T, where g is the *g*-factor and μ_B Bohr magneton, respectively.
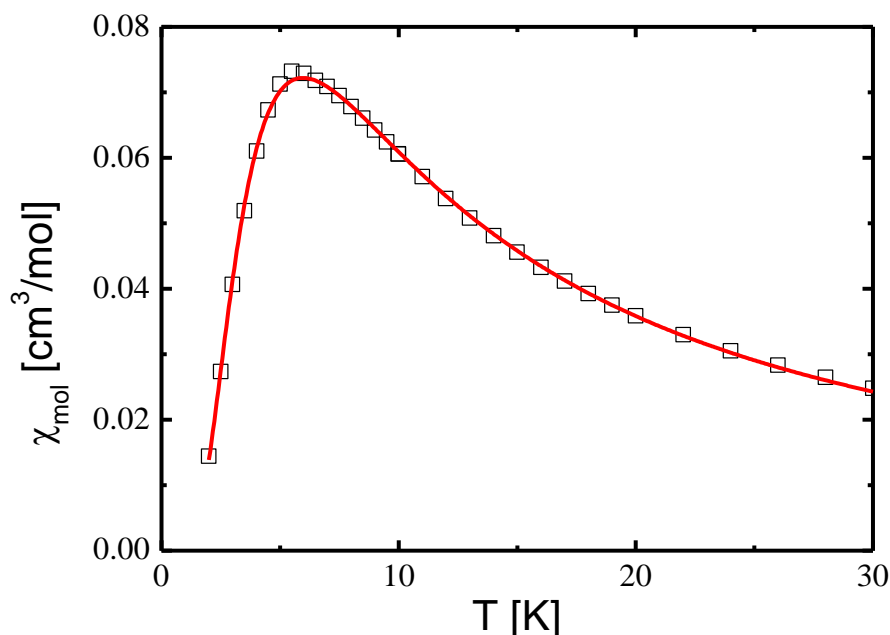
Figure 39: Magnetic susceptibility of a single crystalline sample of TK91 as function of temperature at $B = 0.1$T. Squares are experimental data and the solid line is a fit for an isolated-dimer model.

4.2.4. ESR measurements

ESR measurements have been performed by V. Pashchenko from the Institute for Physics (Goethe University Frankfurt), on a single crystalline sample TK91 in the frequency range 26-40GHz and at 56GHz. The measurements were carried out at temperatures down to 1.5K and in an applied field up to 8.5T.

The ESR measurements detect two non-equivalent magnetic centers of copper ions at any orientation of the sample with respect to the applied magnetic field. Each of these has an axial anisotropy with the g-values in the range of 2.04-2.27 at $T = 108$K, Figure 40. The local magnetic axes of these centers are almost perpendicular to each other. The axial anisotropy is in accordance with the local environment of this coupled-dimer compound determined by X-ray crystal structure analysis.

Figure 41 exhibits a typical ESR single crystalline spectrum of TK 91 at $T=108$K and a frequency of 39.852GHz. The narrow line is the signal of a small amount of the free stable radical DPPH used for calibration. The two non-equivalent Cu^{II} centers are clearly visible in the excitation spectrum.
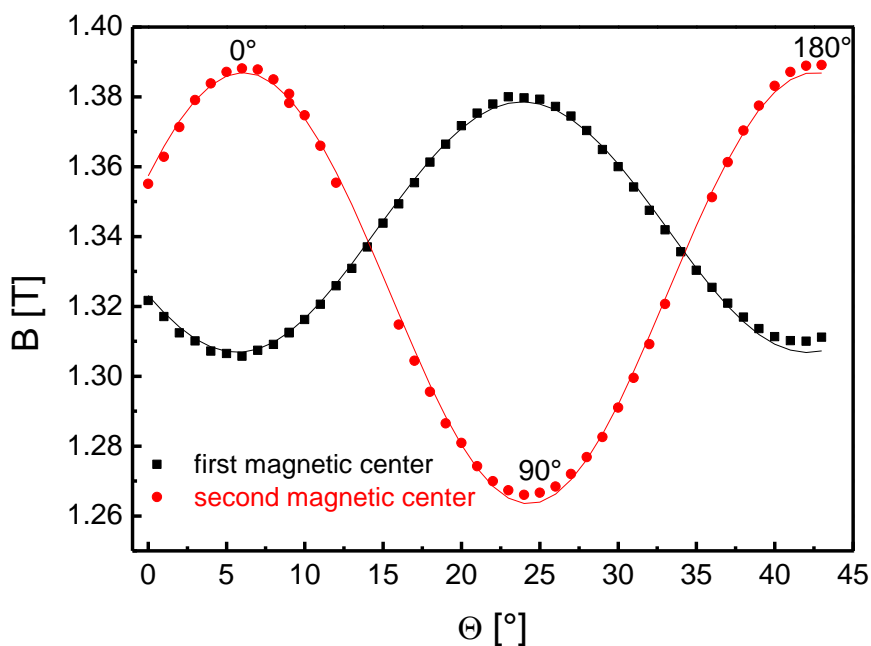
Figure 40: Angular dependence of the ESR resonance lines for a single crystal of TK91 at $T = 108K$.

The inset of Figure 41 displays a picture of a single crystal of TK91. Also indicated in the inset is the orientation of the applied magnetic field (blue arrow) which is tilted by 48.65° with respect to the *a*-axis of the single crystal. In this orientation, the external field is parallel to one of the principal magnetic axes of a Cu^{2+} center with $g = 2.27$. In this field orientation, the second Cu^{2+} center exhibits a *g*-value of 2.09. The values of these *g*-factors are directly connected with the local environment of the Cu^{2+} ions and they are in the range which is expected for six-fold coordinated copper ion [172].

To obtain information on a possible magnetic anisotropy of TK91, ESR measurements have been conducted with the field aligned along and 45°± away from the *a*-axis. The ESR spectrum is displayed in Figure 42. The results show clear resonance absorption lines corresponding to the transition between $S_z = 0$ and $S_z = \pm 1$ sublevels of the triplets. There is no indication of any thermally activated resonance absorption due to the singlet-triplet transition in the whole ranges of fields and temperatures studied. The results demonstrate that TK91 has negligible magnetic anisotropy.
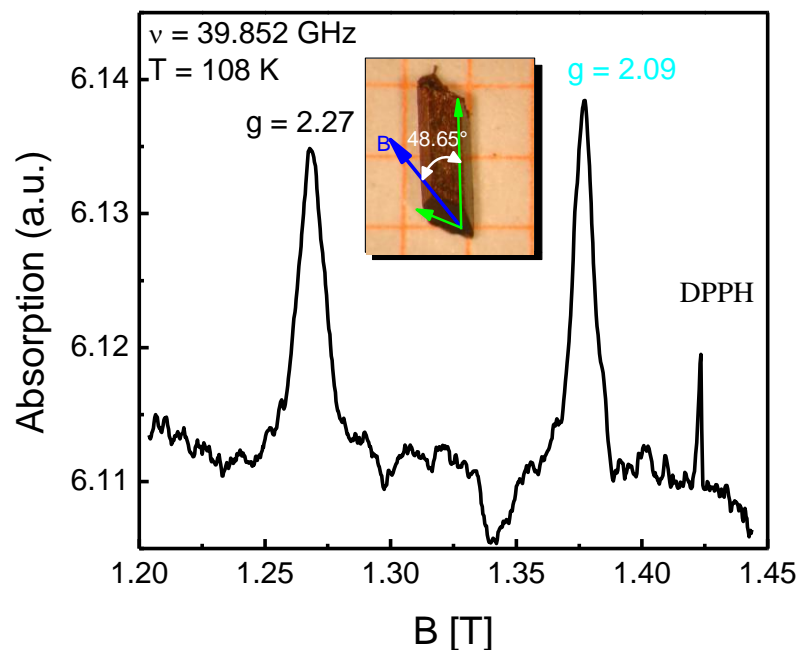
Figure 41: ESR resonance for a single crystal of TK91 at 108K. The inset displays a picture of the single crystal together with the orientation of the principal magnetic axes of a Cu^{II} center.
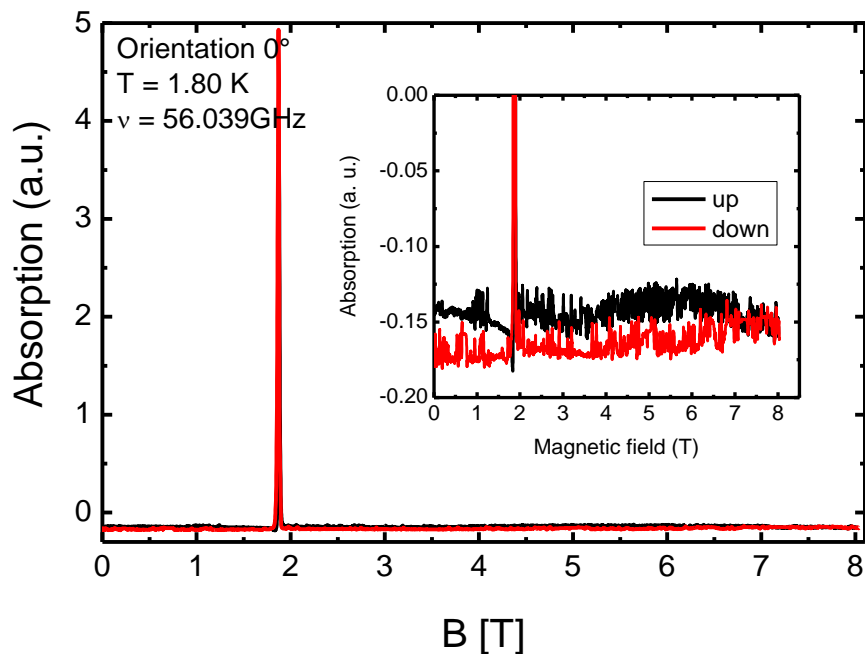
Figure 42: An ESR spectrum of a single-crystalline sample of TK91 at 1.8K at 56.039GHz. Inset shows that there is no additional feature other than the resonance absorption lines, corresponding to the transitions between $S_z = 0$ and $S_z = \pm 1$ sublevels of the triplets at B up to 8T.

4.2.5. Specific heat measurements

The specific heat measurements were performed by A. Brühl from Institute for Physics (Goethe University-Frankfurt).

The temperature dependence of the magnetic specific heat of TK91 at different applied magnetic fields is shown in Figure 43. The magnetic contribution (C_{mag}) to the total specific heat was obtained by subtracting the low-temperature phonon contribution $C_{ph} \sim (T/\Theta_D)^3$ (using a Debye temperature $\Theta_D = 168K$). C_{mag}/T at zero field can be fitted by an isolated-dimer model with $g = 2.1$ and $J_1/k_B \sim 9.6K$ very well (see Figure 43), consistent with the χ data. However, this simple isolated-dimer model starts failing to fit the C_{mag}/T data well at $B \geq 4T$. The deviation from the isolated-dimer model can be attributed to non-zero *inter*-dimer interactions. This hypothesis is supported by *ab initio* calculations which show that TK91 is a 2D-coupled dimer system. The Cu^{2+} ions linked by the modified hydroquinone group form dimers with the *intra*-dimer interaction $J_d/k_B \sim 13.4K$. These dimers are weakly coupled two-dimensionally with antiferromagnetic *inter*-dimer couplings $J_1/k_B = 1.7K$ and $J_2/k_B = 1.4K$.
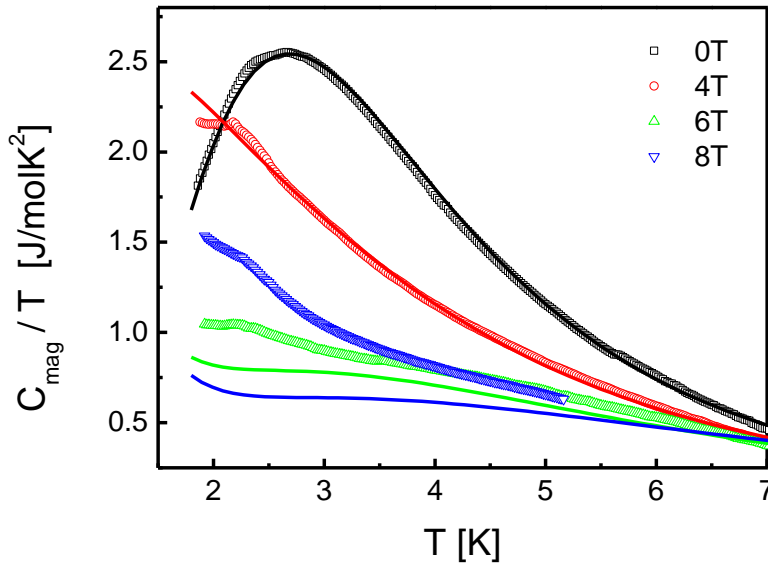
Figure 43: C_{mag}/T vs. T at different applied magnetic fields. Calculated values for an isolated-dimer model with $J_1/k_B \sim 9.6K$ and $g = 2.1$ are shown by solid lines.

4.2.6. Thermal expansion measurements

As suggested by quantum Monte Carlo simulations [173], a field-induced magnetic long-range ordering should develop in a 3D antiferromagnetically coupled spin-dimer system at low temperatures. To search for such a magnetic ordering, the thermal expansion α of a polycrystalline sample of TK91 was examined by G. Donath from The MPI-CPfS Dresden.

As shown in Figure 44, there are pronounced peaks in $\alpha(T)$ when the applied magnetic field is about a few Tesla. Since the polycrystalline sample used in the α experiment was prepared under high pressure, the field-induced transition is expected to occur at a lower field as compared to an ambient-pressure experiment [174]. Therefore, the α data cannot be directly compared with the other results obtained at ambient pressure. Nevertheless, the peaks in $\alpha(T)$ clearly indicate a field-induced phase transition at low temperatures.
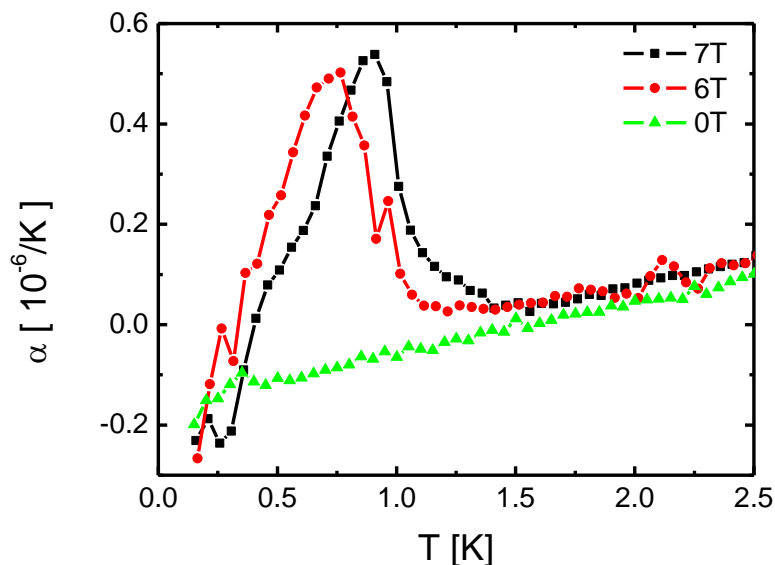
Figure 44: The coefficient of thermal expansion α of a polycrystalline sample TK91 vs. temperature at 0, 6 and 7T, performed by G. Donath, MPI-CPfS Dresden.

4.2.7. AC susceptibility measurements

The ac susceptibility (χ_{ac}) of a single crystal of TK91 was measured as function of field $\chi_{ac}(B)$ and temperature $\chi_{ac}(T)$. The crystal was oriented such that the a-axis is parallel to the applied field. Measurements were performed by using a state-of-the-art compensated-coil susceptometer. Empty-coil measurements were conducted as a direct measure of the sample-independent background. Selections of $\chi_{ac}(B)$ are shown in Figure 45. No hysteresis has been

found upon increasing and decreasing the field. For temperatures below ~ 0.2K, $\chi_{ac}(B)$ has two features. The lower-field feature indicates the field (B_{c1}) where the spin gap closes while the high-field feature indicates the field (B_{c2}) where the system enters the fully polarized state. From these data the critical fields at 0K are estimated to be $B_{c1} \approx 5.9$T and $B_{c2} \approx 6.5$T, respectively. The B_{c1} deduced from $\chi_{ac}(B)$ is lower than the value predicted by the isolated dimer model (6.6T). This difference is presumably due to the effect of the *inter*-dimer interactions giving rise to broadened dispersive triplet states. As the temperature increases, the two peaks in $\chi_{ac}(B)$ broaden, and at a temperature ~ 0.2K they merge into a single round peak. The latter is visible even up to temperatures higher than 1K, where the weak *inter*-dimer interaction should not be important. The broad peak observed in $\chi_{ac}(B)$ is likely not associated with a field-induced phase transition but rather reflects the thermally smeared singlet-triplet excitations of independent dimers. On the contrary, the sharp peaks in $\chi_{ac}(B)$ at low temperatures are likely to be associated with the phase transition to or from a long-range order state which exists inside the critical region [B_{c1}, B_{c2}]. The position of the sharp peaks in $\chi_{ac}(B)$ is plotted in the inset to Figure 45, which resembles the phase diagram of other spin-gap systems [55, 56, 173].
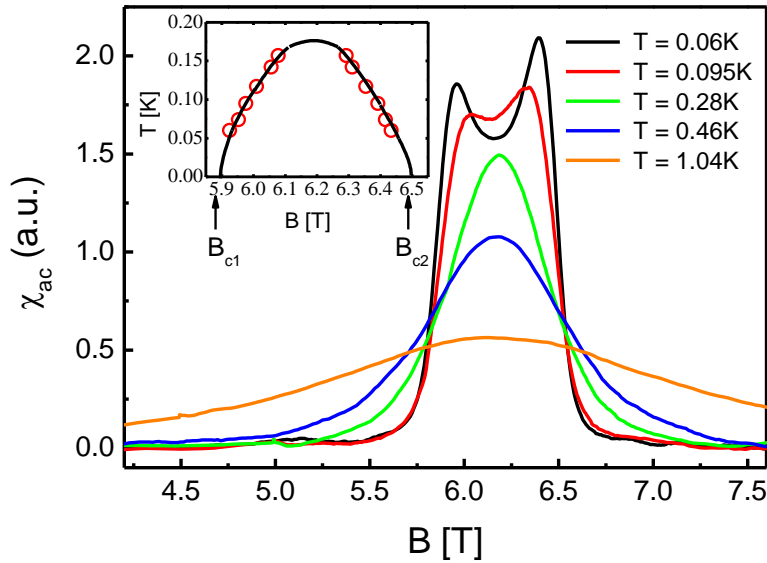

Figure 45: χ_{ac} as a function of applied field at different temperatures. The positions of the sharp features in $\chi_{ac}(B)$ are plotted in the inset and the solid line is a guide to the eyes.

Several regimes can be immediately identified from $\chi_{ac}(T)$ data. These are most clearly seen in Figure 46. As shown in Figure 46(a), for $B < B_{c1}$, the system is in the gapped state, $\chi_{ac}(T)$ is almost zero at low-T and gradually increases as the temperature rises. The data also indicate that the spin gap decreases with field. Then the spin gap closes at $B_{c1} < B < B_{c2}$ (see Figure 46b) and $\chi_{ac}(T)$ increases upon cooling except at the lowest temperatures. Remarkably, at some fields in this region, $\chi_{ac}(T)$ displays a maximum at low temperatures.

The arrows indicate the positions of the maximum in $\chi_{ac}(B)$. (c) $B > B_{c2}$, a gap opens at higher fields.
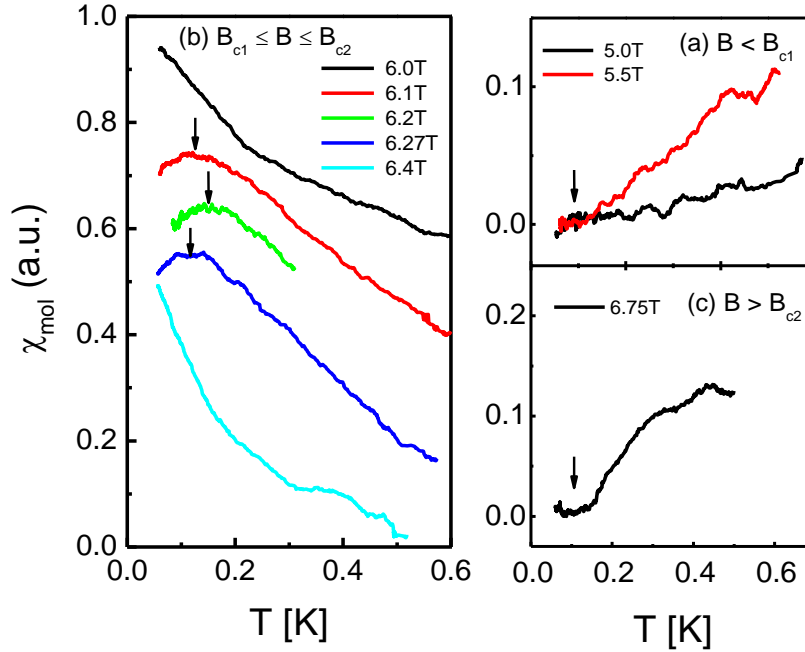

Figure 46: χ_{ac} as a function of temperature at various fields. (a) $B < B_{c1}$, a clear spin gap can be observed. (b) $B_{c1} \leq B \leq B_{c2}$, the gap closes in this field range. Data are offset for clarity. Arrows indicate the positions of the maximum in $\chi_{ac}(B)$. (c) $B > B_{c2}$, a gap opens at higher fields.

The drop in $\chi_{ac}(T)$ at low temperatures was also detected in $BaCuSi_2O_6$ [172] and was identified as the onset of the condensation of magnons. At $B = 6.2T$, the maximum in $\chi_{ac}(T)$ locates at $\approx 0.15K$ which is very close to the phase boundary interpolated from the $\chi_{ac}(B)$ data (cf. inset to Figure 45). As B moves away from 6.2T, the maximum in $\chi_{ac}(T)$ shifts to lower temperatures which is also consistent with the phase diagram obtained from $\chi_{ac}(T)$. At higher fields $B > B_{c2}$, another spin gap opens (see Figure 46c)).

At low temperatures and in high magnetic fields, the interactions between the dimers will determine the nature of the ground state, which is likely a canted antiferromagnet. Within a picture of 3D coupled dimers with negligible magnetic anisotropy, a field-induced ordered state would be expected in TK91 [43]. In such a scenario the peaks in $\chi_{ac}(B)$ below 0.2K would be associated with this state. Since the system has negligible magnetic anisotropy, the order state would then be a magnetic BEC state. However, unlike the other coupled 3D dimer systems, where sharp λ-like peaks in thermodynamic quantities indicate thermodynamic transitions at the on- and off-set of conventional long-range order [33, 34], no indications of such divergences are found in TK91! Because of that and in order to get a detailed

understanding of the distinct low-temperature anomalies in $\chi_{ac}(B)$ below 0.2K, especially with regard to the dimensionality of the interactions and the implications for the type of order that is realized here, Quantum Monte Carlo (QMC) simulations of the susceptibility have been performed.

4.2.8. Quantum Monte Carlo Simulations

Quantum Monte Carlo simulations were performed by Stephan Wessel from the Institute for the Theoretical Physic, University Suttgart, based on the low-energy spin-lattice geometry obtained from DFT and a general form of a spin-½ Heisenberg model on an anisotropic honeycomb lattice, see Ref [171]. The QMC simulations have been performed for models with different anisotropies in the magnetic couplings, including the effect of a finite *inter*-plane coupling $J_\perp$.

The combinations of exchange parameters which were considered in the analysis were constrained by the positions of the low- and high-field peaks in $\chi_{ac}(B)$. Assuming a dominant *intra*-dimer exchange J_d, the effective spin exchange parameters can be estimated from an expansion of B_{c1} and B_{c2} up to first order in the *inter*-dimer exchange. For the honeycomb lattice, by setting $J_1 = J_2 = J_\parallel$, this yields $g\mu_B B_{c1} = J_d - J_\parallel - J_{\perp/2}$ and $g\mu_B B_{c2} = J_d + 2J_\parallel + J_\perp$, the latter formula is exact as B_{c2} equals the saturation field. In his analysis S. Wessel considered three different *inter*-dimer coupling shemes:

    (1) One-dimensionally coupled dimers, 1D
    (2) Two-dimensionally coupled dimers, 2D
    (3) Strongly anisotropic three- dimensionally coupled dimers, 3D.

The results of this analysis are presented together with the experimental results in Figure 47. Details of the analysis can be found in Ref [171].
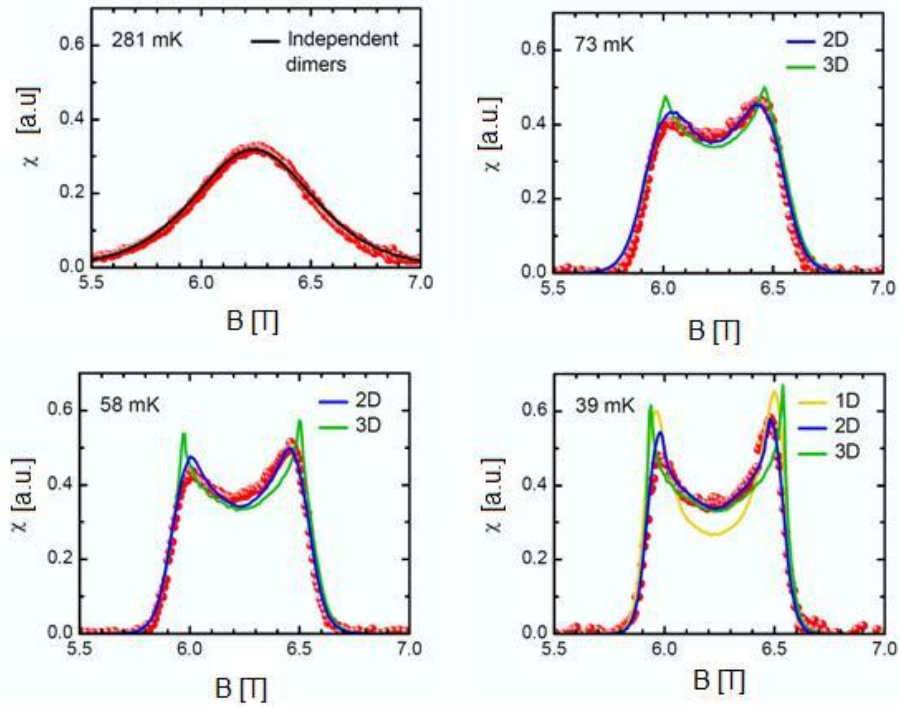
Figure 47: Magnetic susceptibility as a function of the magnetic field *B* for different temperatures. The solid lines (blue, green and light brown) are the results of Quantum Monte Carlo simulations for the 2-dimensional distorted honeycomb lattice using an *intra*-dimer coupling of $J_d/k_B = 9.507$K and three different *inter*-dimer coupling schemes. Black solid line corresponds to singlet-triplet excitations of independent dimers.

As can be seen from Figure 47, the 1D-model does not fit the data well, even though it generates rounded peaks, it fails in quantitatively describing the $\chi_{ac}(B)$ peaks and the minimum at intermediate fields. The anisotropic 3D-model with an anisotropy $J_\parallel/J_\perp = 6$ describes the data in the intermediate field range quite well, but it significantly deviates from the data around the peaks. The sharp features found in the simulations, indicating divergence in $\chi_{ac}(B)$, reflect the on- and off-sets of usual field-induced long-range antiferromagnetic order, as a consequence of the 3D interactions. The model description becomes considerably improved, however, by considering the purely 2D-model, i.e. excluding any *inter*-layer interaction. Such a type of model yields the correct rounding around the $\chi_{ac}(B)$ peaks and it reproduces well the $\chi_{ac}(B)$ data at intermediate fields. The 2D-model provides an excellent description of the double-peak structure upon increasing the temperature from 39 mK to 58 and 73mK.

From the previous discussion it is obvious that the purely 2D Heisenberg model of weakly interacting dimers is a suitable basis for describing the field-induced effects observed in TK91 at low temperatures. The strictly 2D character of the exchange interaction implies that the state realized here is not the usual field-induced long-range antiferromagnetism (known as the BEC of triplons), but has to be assigned to a *collectively-coupled dimer state* of different type.

4.2.9. Berezinskii-Kosterlitz-Thouless transition

As it was pointed out by Berezinskii, Kosterlitz and Thouless [61-63] long time ago, there is a different type of phase transition at a temperature T_{BKT}, associated with topological order, which is inherent to the 2D *XY* model. Details of the theory are given in the Chapter 2.1.2.

The question which raises here is whether the 2D *XY* model is applicable to the TK91 in the field range $B_{c1} \leq B \leq B_{c2}$. As it was pointed out by various authors [70, 175], a BKT transition and generic *XY* behaviour can be found also in an $S = \frac{1}{2}$ 2D Heisenberg antiferromagnet by the application of a finite magnetic field along the z axis which breaks the $O(3)$ symmetry of the isotropic model. In the case of the dimerized systems like TK91, this scenario is applicable for $B_{c1} \leq B \leq B_{c2}$, while then the low-energy physics of the system can be mapped on an effective easy-plane spin-½ *XXZ* model at a field $B - B_{c1}$ [176].

As it was discussed in the Chapter 2.1.2, the helicity modulus (spin stiffnes) *Y* is a physical quantity, which can tell us at which finite nonzero temperature the system undergoes the phase transition driven by the binding of vortices, Equation 6. Therefore, S. Wessel performed QMC calculations for the 2D model to estimate the helicity modulus *Y*, by using the same set of parameters as utilized above for the analysis of susceptibility data. On the upper panel of Figure 48, the helicity modulus (spin stiffnes) *Y* as a function of temperature at a field $B = 6.144$T is shown. All data from QMC calculations are based on the finite-size analysis and in order to extract the exact BKT transition temperature from the finite-size data, an analysis of Weber and Minnhagen [177] was employed (for the details of analysis, see Ref [171]).The field value of $B = 6.144$T is selected, because there the maximal T_{BKT} is expected.

In the lower panel of Figure 48, the normalized magnetization (blue spheres, derived from QMC calculations) is presented together with experimental data (black spheres, derived by integrating experimental $\chi_{ac}(B,T = \text{const})$ curves), where M_{max} corresponds to the magnetization of the fully-polarized state at $B \geq B_{c2}$. As one can observe, there is a pronounced minimum in the magnetization data well above T_{BKT}. As it was discussed earlier [82] for a square-lattice configuration, the growth in the magnetization is a clear signature of the crossover to *XY* behaviour.
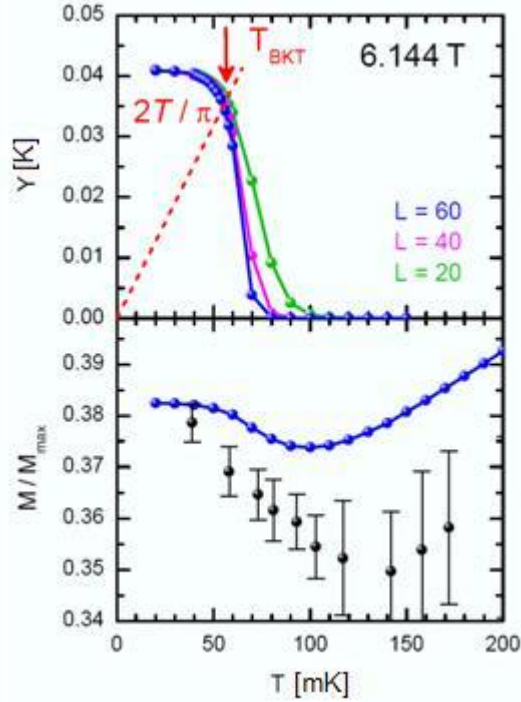
Figure 48: Helicity modulus and uniform magnetization. Upper panel shows QMC results of the helicity modulus for systems of linear size *L* as a function of temperature. The broken straight line corresponds to the universal curve *2T/π*, and the arrow marks the transition temperature T_{BKT} obtained from the finite-size analysis. Lower panel shows magnetization data derived from QMC calculations together with experimental data.

The results of QMC calculations are summarized in Figure 49. As it can be seen, the data indicating that in TK91 a BKT topological order is stabilized in magnetic fields $5.95T \leq B \leq 6.5T$ with a maximum BKT transition temperature of about 50mK obtained in a field of 6.2T. The red symbols mark points where the transition into the BKT-phase take place and the red solid line is a guide for the eyes. For comparison, Figure 49 includes the positions of the χ_{ac} maxima as read off the data (green symbols), which define the range of stability of the 2D *collectively-coupled dimer state*.

Within the effective easy-plane *XXZ* model, the onset of the green region can be assigned to the crossover from the high-*T* isotropic to the low-*T XY* behaviour. This region also marks the onset of the formation of vortices and antivortices emerging in the effective spin configurations. As it can be seen in the phase diagram, the on- and offset fields of the crossover range merge with the corresponding fields that delimit the BKT topological order for $T \rightarrow 0K$. Therefore, it can be concluded that the novel field-induced state revealed by the susceptibility measurements at the lowest temperature is a direct manifestation of the BKT topological order.
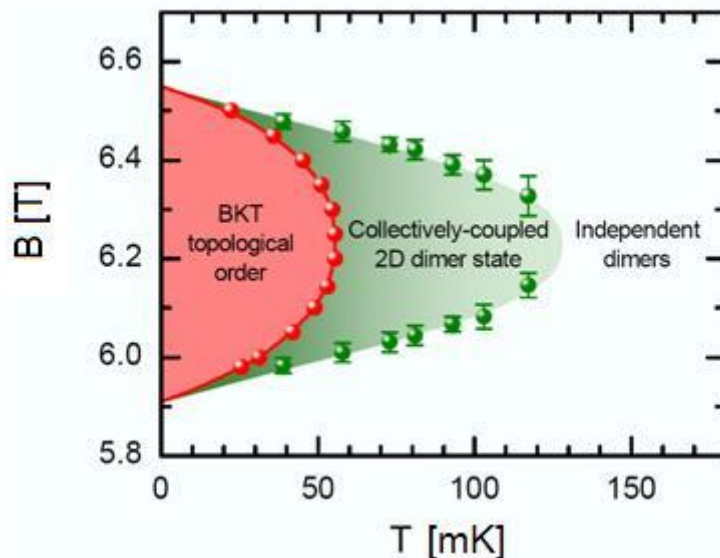
Figure 49: B-T Phase diagram of $C_{36}H_{48}Cu_2F_6N_8O_{12}S_2$ (TK91) at low temperatures.

According to the results of the previous analysis, the *ac* planes in TK91 appear to be essentially decoupled. The dimensional reduction of the magnetic behaviour in this system can be explained by the presence of effectively frustrated *inter*-plane interactions. Refined *ab-initio* analysis of all non-zero *inter*-plane interactions showed the existence of weak coupling terms $J_{\perp}^{'}$ of energies $0.02\,K < J_{\perp}^{'}/k_B < 0.1\,K$ frustrating the contribution of $J_{\perp}$.

4.2.10. Summary

A new family of low-dimensional quantum-spin systems based on hydroquinone-derived linkers connecting Cu^{2+} ions carrying a spin of $S = \frac{1}{2}$ was synthesized. It has been shown that by such an approach a moderate antiferromagnetic exchange interaction between the Cu^{2+} ions can be achieved. These linkers could be chemically modified to synthesize compounds with desired magnetic properties. The organic compound discussed here, $C_{36}H_{48}Cu_2F_6N_8O_{12}S_2$ (TK91), is a result of such a design strategy. As demonstrated in Figure 38, the Cu^{2+} ions have distorted octahedral coordination environment and are bridged by hydroquinone linkers to form dimer units. Neighboring dimers are connected via two long axial Cu-O bonds providing a potential path for *inter*-dimer magnetic exchange. The value of the *intra*-dimer coupling, from *dc*-susceptibility measurements, is found to be $9.4(2)K/k_B$. ESR measurements suggested that the magnetic anisotropy of this compound is negligible. Specific heat data in magnetic fields $B \geq 4T$ revealed marked deviations from isolated dimer behaviour and these observations have been attributed to the presence of a significant dimer-dimer interaction. Actually, clear indications for *inter*-dimer interactions were found in *ab initio* calculations yielding a ratio of *intra*- to *inter*-dimer couplings of 10:1, $J_d/k_B \sim 13.4K$, $J_1/k_B = 1.7K$ and $J_2/k_B = 1.4K$. The *ac*-susceptibility data showed that at $T \geq 0.2K$, a single

broadened peak around 6.2T appears. Upon cooling below 0.2K, the peak narrows significantly and two increasingly sharp features appear on its low- and high-field side. The positions of the sharp maxima in $\chi_{ac}(B)$ are assign as the lower and upper boundary of a new field-induced state. AC-susceptibility data together with QMC simulations show that a new field-induced ground state has developed in the field range 5.9 $T \leq B \leq$ 6.3T. Employing detailed QMC analysis for the *ac*-susceptibility data, it was shown that field-induced state has a distinct 2D character. Even more, it was shown that that this 2D state is actually the topological order predicted by Berezinskii, Kosterlitz and Thouless.

4.3. Oxalate-bridged Materials

As mentioned in the Introduction, metal-organic compounds usually consist of magnetic metal ions bridged by an organic molecule (such as CO_2 - carboxylate, C_2O_4 - oxalate, diamine etc.) and some side organic ligands such as betaine, aminopyridine, hidroquinone, isoquinoline etc. Metal-organic compounds with one-dimensional (1D) magnetic interactions are often chains of metals, bridged by carboxylate groups of organic molecules and contain additional large organic ligands as spacers to separate the chains. The bridging and spacer functions can be assumed by one entity as in the case of betaine molecules [151], where one has a carboxylate group and a large chemically inactive tail which plays the role of the spacer.
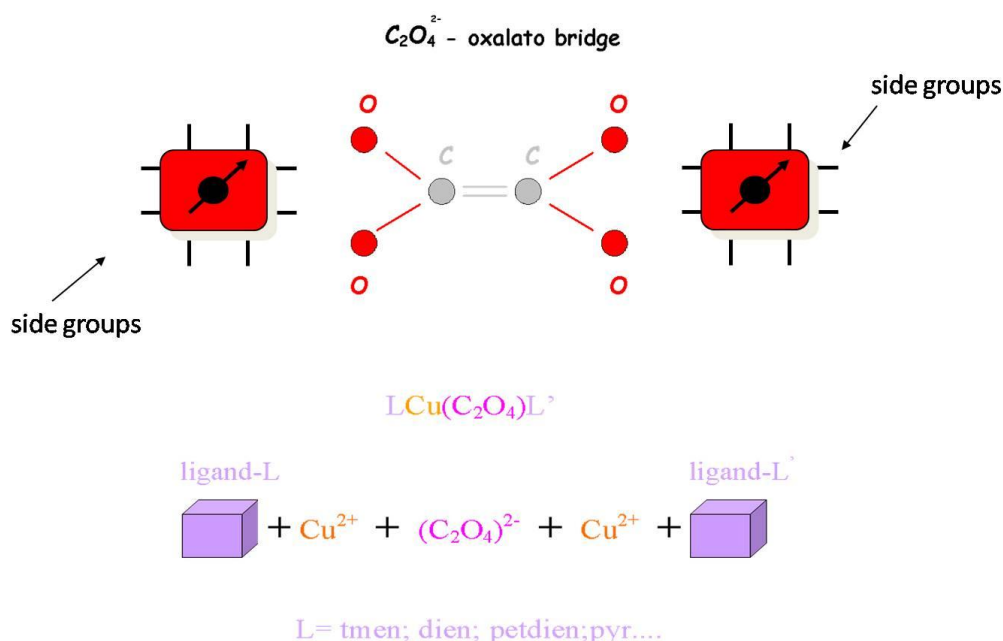
Figure 50: Oxalate bridging unit and building block scheme.

More flexibility in designing magnetic chain structures offers the combination of two different organic molecules, a large molecule as spacer (to separate the chains) and a small dicarboxylate or diamine molecule, for instance, to bridge the metal ions. The oxalate molecule turned out to be an especially suitable bridging unit for mediating the magnetic interactions. There are several compounds with oxalate metal chains known as one-dimensional ferro- or antiferromagnets at low temperatures. Most of them are of composition $[M(ox)L]_n$ with $M = Co^{2+}$, Ni^{2+}, Cu^{2+} and the ligand L = hydroxypyridine [178, 179],

isoquinoline [179], amino-pyridine [180, 181] or even just water [182] , for a building scheme see Figure 50.

In the theoretical studies [20, 183] correlations between the strength of magnetic interaction and the structural configuration of the magnetic ions were investigated and classified. According to Cano [20] there are basically four different configurations of the singly occupied molecular orbitals (SOMOs) realized experimentally: coplanar, perpendicular, parallel and trigonal-bipyramidal, see Figure 51. In the crystals cited above there are many examples of "parallel" configuration, but only two examples of "coplanar" configuration, one with Ni^{2+} and one with Co^{2+}.
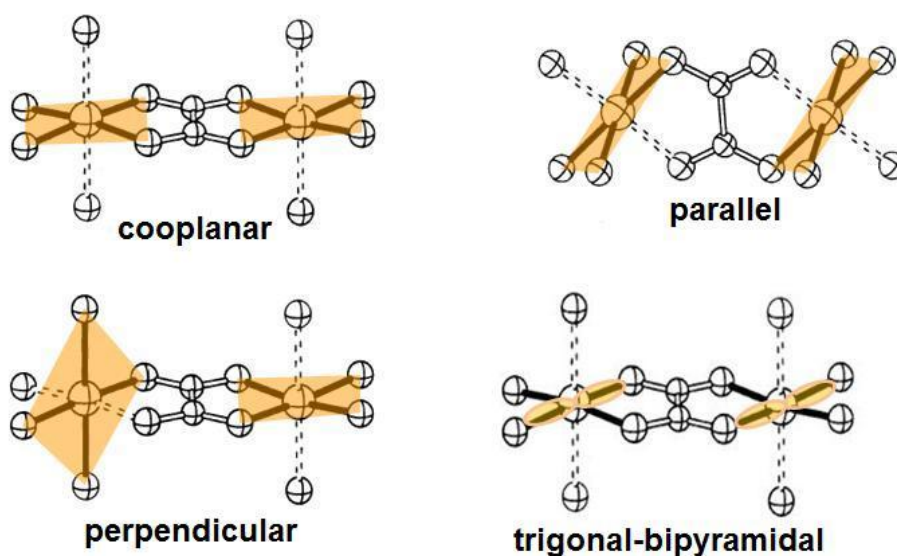
Figure 51: Different oxalate topologies according to the orientation of the SOMO's orbitals.

4.3.1. Alternating Heisenberg chain Cu(ox)(pyOH)·H₂O

4.3.1.1. Crystal Synthesis and Structure

Crystals of Cu(ox)(pyOH)·H₂O with ox-oxalate $(C_2O_4)^{2-}$ and pyOH-hydroxypyridine (C_5H_5NO) were grown by L. Wiehl from the Institute of Geosciences (Goethe University-Frankfurt), according to the recipe of Castillo *et al.* [178]. During the evaporation of the solvent, two different phases emerged, blue isometric crystals of Cu(ox)(pyOH)₂, which have already been described and light-green plates of Cu(ox)(pyOH)·H₂O, which proved to be a new phase, see Figure 52.
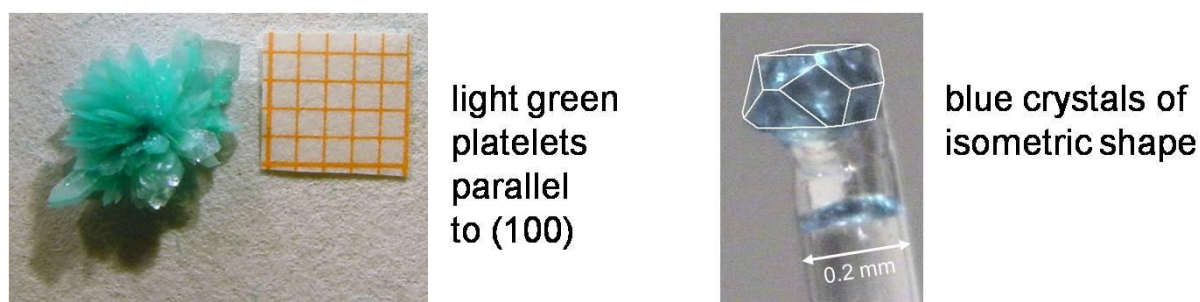
Figure 52: Single crystals of the two different phases, Cu(ox)(pyOH)·H₂O light-green plates and Cu(ox)(pyOH)₂ blue crystals.

The crystal structure of Cu(ox)(pyOH)·H₂O was determined by L. Wiehl, by single crystal X-ray diffraction, using a four-circle diffractometer from Oxford Diffraction with CCD detector. Experimental details and structure data have been published previously by L. Wiehl *et al.* [150].

The crystals of Cu*(ox)(*pyOH*)*·H₂O are monoclinic, space group $P2_1/c$ (No. 14), with lattice constants $a = 12.915$Å, $b = 9.162$Å , $c = 8.247$Å , $\beta = 98.49°$. The crystal structure is built up from oxalato-bridged copper ions, hydroxypyridine molecules and crystal water. Each Cu^{2+} ion has slightly distorted bipyramidal coordination, formed by the nitrogen atom from a hydroxypyridine molecule and five oxygen atoms from three different oxalate molecules, see Figure 53-55.

The basal plane of the bipyramid is formed by the nitrogen atom and three oxygen atoms (O1A, O2A and O1B) with copper-ligand distances in the range of 1.98-2.01Å. The apical positions are occupied by oxygen atoms (O2B, O2B') at larger distances of 2.35 and 2.41Å. Each of these apical oxygen atoms is shared by two Cu polyhedra, building a quasi-2D

structure, see Figure 53. The hydroxypyridine rings lie above and below the 2D layers, and the layers are separated by the length of the *a*-axis.
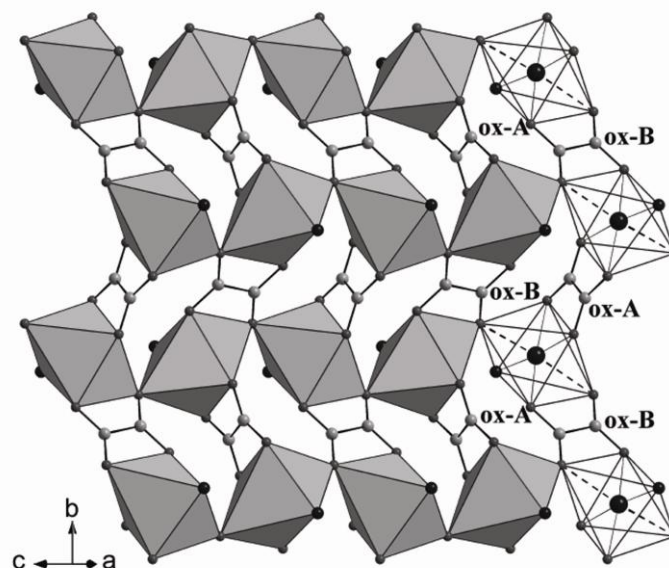

Figure 53: Two-dimensional network of oxalato-bridged Cu^{2+} ions in Cu*(ox)*(pyOH*)*·H₂O. The copper coordination sphere is a slightly distorted $CuNO_5$ octahedron. The dashed lines indicate the contacts of the copper ions with two apical oxygen atoms. ox-A and ox-B are two non-equivalent oxalate molecules. 3-hydroxypyridine and water molecules have been omitted for clarity.

There are direct bonds only between copper and the four atoms in the basal plane of the bipyramid, forming -Cu-oxalate-Cu-oxalate- chains along the *b*-axis, see Figure 53. Due to the lack of direct bonds perpendicular to the basal plane, the *inter*-chain coupling via the apical oxygen atoms along the *c*-axis is expected to be very small. The new and important structural feature of Cu*(ox)*(pyOH*)*·H₂O, manifests itself in the alternation of two centro-symmetric oxalate molecules ox-A and ox-B which are symmetrically non-equivalent. Both molecules bridge pairs of copper ions, but the oxalate molecule shows different orientations relative to the bipyramid basal plane. For ox-A, the bridging oxalate molecule joins corners of a bipyramid basal plane, leading to a configuration where the two basal planes of the Cu bipyramids and the ox-A molecule lie in a common plane, see Figure 54. This corresponds to the 'coplanar' configuration according to the classification given by Cano *et al.* [20].
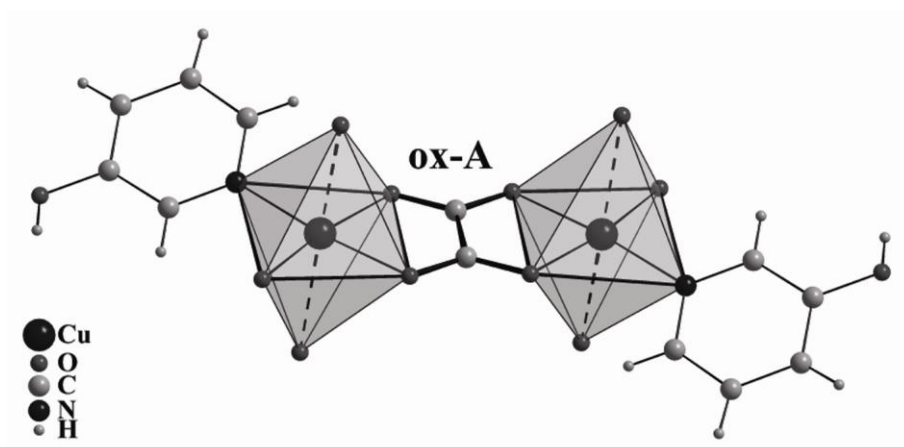
Figure 54: The Cu–oxalate–Cu bridge via ox-A, representing a 'coplanar' configuration.

On the other side, the ox-B molecule is oriented perpendicular to the two neighbouring copper basal planes and its carboxyl groups each connect a corner of a basal plane with its apex, see Figure 55. The two pyramidal bases are parallel to each other (as in the case of ox-A) but are in different planes, corresponding to the 'parallel' configuration.
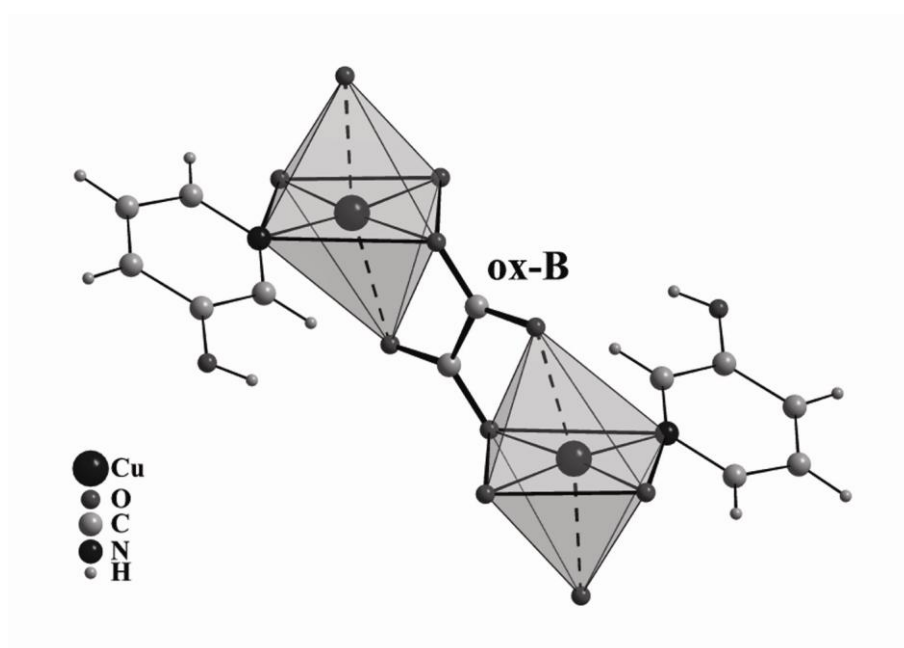

Figure 55: The Cu-oxalate-Cu bridge via ox-B, representing a 'parallel' configuration.

If the coordination of the central metal ion were to be ideally octahedral, then these two types of oxalate bridges would be indistinguishable as each square section of the octahedron could be taken as the basal plane. For the d^9 configuration of Cu^{2+}, however, the

energies of the d_{x2-y2} and the d^2_z orbitals are significantly different due to the Jahn–Teller effect. In an elongated octahedral ligand field, the single electron occupies the d_{x2-y2} orbital. Therefore, the terms 'coplanar', 'parallel' or 'perpendicular' characterize the relative orientations of the d_{x2-y2} orbitals of the bridged copper ions. Depending on the case, none (ox-A) or two (ox-B) of the oxygen atoms of the oxalate bridge are orientated towards the antibonding d^2_z orbital. This is the origin of the large differences in magnetic interaction strength found in oxalato-bridged binuclear copper complexes [20, 183], which is high for 'coplanar', intermediate for 'perpendicular' and low for 'parallel' complexes.

The previously discovered and studied crystals of Cu*(ox)*(pyOH)₂ reveal 1D ferromagnetic interactions with $J/k_B = -1.9$K [178]. In this material, all oxalate molecules, and hence all Cu-ox-Cu bridges, are equivalent and adopt the 'parallel' configuration consistent with the observed weak ferromagnetic interaction.

In contrast to the magnetic properties of Cu*(ox)*(pyOH)₂, the newly discovered phase of Cu*(ox)*(pyOH)·H₂O exhibits two different exchange paths alternating along the *b*-axis. This feature, along with the presumably very small *inter*-chain coupling along the *c*-axis, as described above, suggests a description of the magnetic properties in terms of an alternating-exchange spin-chain. Exchange anisotropy due to a Dzyaloshinskii–Moriya interaction between two neighbouring Cu²⁺ ions is not expected, because the two centrosymmetric oxalate molecules ox-A and ox-B both exhibit a centre of inversion symmetry. However, the existence of a staggered *g*-tensor along the *b*-axis cannot be excluded.

4.3.1.2. Magnetic properties

The magnetic measurements were performed on single crystalline Cu*(ox)*(pyOH)·H₂O, in the temperature range 2-300K and in fields of up to 5T. Single crystals of the Cu*(ox)*(pyOH)·H₂O were separated from other materials of different appearance, including the Cu*(ox)*(pyOH)₂ and a phase of unknown composition. A bundle of well-shaped single crystals with a total mass of 7.89mg was selected for the experiments. These crystallites, randomly oriented, were immersed in a small amount of paraffin inside the sample holder. Due to this procedure, the individual crystals were unable to move, leading to a significant increase of the signal-to-noise ratio.

The molar magnetic susceptibility χ_{mol} of Cu*(ox)*(pyOH)·H₂O in the temperature range $2K \leq T \leq 300K$ measured in a field of 1T is shown in Figure 56. These data are corrected for a temperature-independent diamagnetic contribution of paraffin and the diamagnetic core contributions of Cu*(ox)*(pyOH)·H₂O estimated according to [95].

At around 270 K, a broad maximum in $\chi_{mol}(T)$ is visible, characteristic for a low-D spin system, where $\chi_{mol}(T)$ is governed by short-range spin correlations. Below 270K, the susceptibility is continuously decreasing down to 60K. The steep increase at low temperatures is attributed to a Curie-contribution, resulting from uncoupled Cu²⁺-ions. This is corroborated

by plots of the inverse susceptibility of the data below 10K in the inset of Figure 56, which shows an approximate linear behaviour extrapolating to zero for $T \rightarrow 0$K. From the slope of the straight line, a concentration of the uncoupled Cu^{2+} ($S = ½$)-ions of (1.5 ± 0.2) % is estimated. This small value directly reflects the considerably high quality of the single crystals.
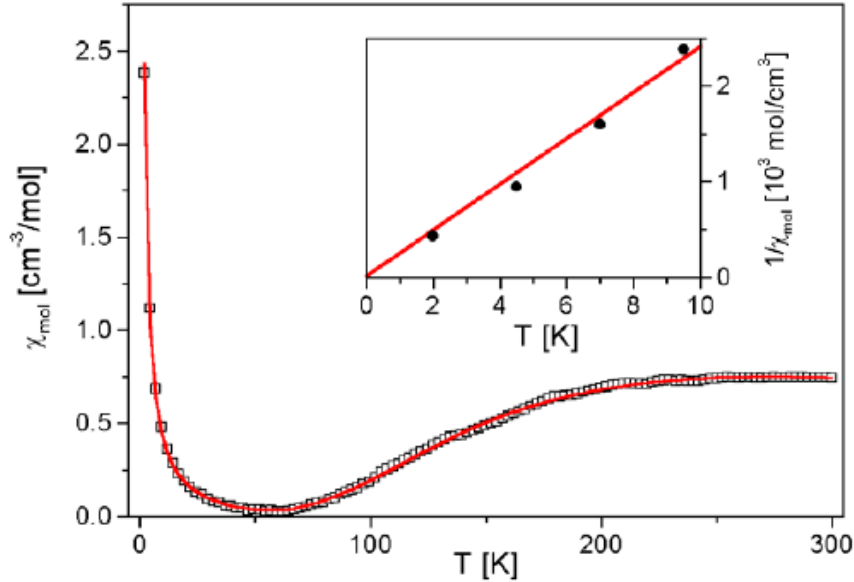

Figure 56: Temperature dependence of the molar magnetic susceptibility χ_{mol} of randomly oriented single crystals of Cu(ox)(pyOH)·H₂O in the temperature range 2-300K in a magnetic field of 1T. The solid line is a least-square fit according to [107]. Inset: inverse susceptibility in the low-temperature range.

For a quantitative analysis of the $\chi_{mol}(T)$ data, the theoretical results for an antiferromagnetic $S = ½$ Heisenberg spin chain with alternating exchange coupling constants J and $J' = \alpha J$ were applied [107]. For this model, the Hamiltonian in the form given by the Equation 38 is used. There J and $J' = \alpha J$ are the alternating Heisenberg exchange interactions between neighbouring spins along the chain. For the alternating Heisenberg chain, the position of the maximum in $\chi_{mol}(T)$ is determined by the dominant coupling constant J [107]. The maximum is located at $k_B T^{max} = 0.64J$, and is practically independent of the alternation parameter α. Performing a least-squares fit of the $\chi_{mol}(T)$ data, three adjustable parameters were used: the dominant magnetic exchange constant J, the alternation parameter α and the g-factor. A fourth parameter, associated with the Curie contribution of uncoupled $S = ½$ spins, was added. The result of this fitting procedure, shown as the straight line in Figure 56, nicely describes the experimental data. The following parameters have been derived: $J/k_B = -(442 \pm 5)$K, $\alpha = 0.13 \pm 0.06$, i.e. $J'/k_B = -(58 \pm 17)$K, and a g-factor of $g = (2.19 \pm 0.03)$. In addition, the fit yields a concentration of about 1.5% of uncoupled $S = ½$ impurities, consistent with the concentration determined from the slope of $1/\chi_{mol}(T)$ at $T \leq 10$K. The g-factor revealed from the fit is in accordance with the expectation for randomly

oriented single crystals containing Cu^{2+} ions in a distorted octahedral environment [184]. Employing Equation 39, the zero-field excitation gap is estimated to $\Delta = (410 \pm 20)$K.

In view of the structural properties and supported by relative bond strengths, it appears justified to model Cu*(ox)*(pyOH*)·*H₂O as a dimerized spin-chain. Along the *b*-axis of the crystal, one finds two distinct oxalate bridges, 'coplanar' ox-A and 'parallel' ox-B, which alternate from bond to bond, resulting in an alternating exchange spin $S = \frac{1}{2}$ chain. In [20], Cano *et al.* summarize various experimental and theoretical results found for dinuclear oxalato-bridged compounds. For the 'parallel' configuration, they obtained experimental values for the exchange coupling ranging from -2 to 53K, whereas they listed coupling constants for the 'coplanar' orientation from 430 to 575K. The same magnitude of the magnetic coupling constants was calculated using density functional theory (DFT) methods on selected oxalato-bridged model systems [20]. Although the material investigated here consist not from isolated dimers but from a dimerized spin chain (a much more complicated magnetic structure), the coupling constants of Cu*(ox)*(pyOH*)*H₂O, derived from susceptibility measurements, are comparable to the ones listed in [20].

For a dinuclear oxalato-bridged model compound, Cano *et al.* showed that despite the influence of the electronegativity of the terminal ligands and some other structural parameters, the most important effect governing the strength of the magnetic coupling constant *J* is the displacement h_M of the Cu atoms away from the basal plane of the coordination polyhedra. This displacement h_M is schematically displayed in Figure 57.
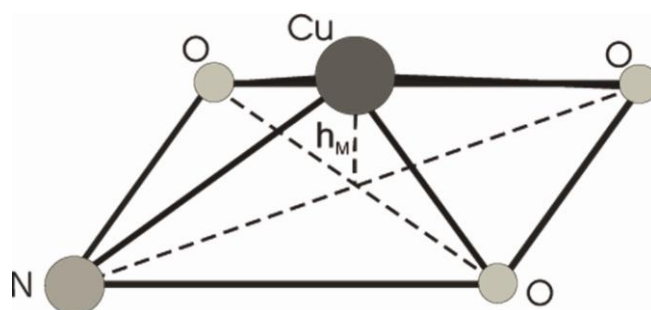

Figure 57: Sketch of the local Cu environment indicating the displacement h_M of the Cu atom away from the basal plane of the coordination polyhedra.

A basal plane was fitted with the four atoms (one nitrogen N, three oxygen O1A, O2A, O1B) forming the basal plane of the bipyramids. The given value for h_M is the distance of the Cu^{2+} ion to this plane. For the coplanar ox-A bridge in Cu*(ox)*(pyOH*)·*H₂O, a displacement out of the basal plane for the Cu^{2+} ion of $h_M = 0.035$Å was obtained. In comparison to some of the isolated dimer compounds, this is only a moderate displacement. Comparing this displacement with the experimental and theoretical results shown in Ref.[20], one expects for $h_M = 0.035$Å, $J_{theo}/k_B = -415$K and a $J_{exp}/k_B = -(570 \pm 40)$K. In fact, the dominant (*intra*-dimer)

coupling J/k_B = -(442 ± 5)K of the present dimerized spin-chain Cu(ox)(pyOH$)$·H₂O is close to these values, lying in between the theoretical and experimental values for the displacement h_M realized here. This observation suggests that, similar to isolated dimers, the strength of the magnetic couplings in oxalato-bridged coupled dimer systems is mainly determined by the displacement of the Cu^{2+} ion out of the octahedral plane.

4.3.1.3. Summary

A new low-dimensional quantum-spin system Cu(ox)(pyOH$)$·H₂O, based on oxalate linker connecting Cu^{2+} ions carrying a spin of S = ½, was synthesized. Each Cu^{2+} ion has slightly distorted octahedral coordination. The Cu^{2+} ions are bridged by oxalate molecules and form chains along the b-axis. The oxalate molecules have two different arrangements alternating along the chain. Among the polymeric oxalate chains reported up to now, the compound Cu(ox)(pyOH$)$·H₂O is the first example of a Cu^{2+} oxalate chain with an alternation of 'coplanar' and 'parallel' topologies along the chain. Due to these specific structural properties, magnetic properties were analyzed in the framework of an alternating-exchange spin-chain. Using the model of antiferromagnetic S = ½ alternating Heisenberg chain, an exchange coupling constant of J/k_B = -(442 ± 5)K and an alternation parameter α = 0.13 ± 0.06 were derived. Due to the presence of a 'coplanar' Cu-coordination, this is the first time that such a strong antiferromagnetic interaction has been found in a Cu^{2+}-based polymeric oxalate chain. Such a strong antiferromagnetic interaction classifies Cu(ox)(pyOH$)$·H₂O as a strongly dimerized spin-chain compound. In this strongly dimerized chain the magnetic behaviour is mainly determined by the displacement of the Cu^{2+}-ions with respect to the basal plane of the local environment.

4.3.2. Heisenberg chain [Cu(μ-C$_2$O$_4$)(4-aminopyridine)$_2$(H$_2$O)]$_n$

Metal-organic coordination polymers, containing a bridging oxalate ligand, have played a key role in the development of new concepts in molecular magnetism over the last two decades. The ability of this ligand to mediate electronic effects between paramagnetic metal ions separated by more than 5Å make this ligand very attractive in molecular magnetism. A plethora of oxalato-bridged dinuclear complexes has been well-characterized and intensive magneto-structural studies have been analyzed, from both experimental [185, 186] and theoretical [20, 187] viewpoints. Of particular interest have been the structural and electronic factors (orbital topology, coordination polyhedra, donor atoms, nature, and substituents of the periphedral ligands) that govern the value of the magnetic coupling through oxalate. Many of the one-dimensional oxalato-bridged systems [Cu(μ-ox)(L)$_x$] (L = nitrogen donor ligand or water molecule) have been described, showing that the coupling ranges from mediate [188, 189] to weak [190, 191] antiferromagnetic and even ferromagnetic [19, 192, 193, 194].

It has been shown, that with the oxalate anion, it is possible to construct two- [195] and three-dimensional [196] homo- and hetero- transition metal networks, which form molecular-based magnetic materials, exhibiting a great diversity of magnetic behaviours (ferro-, ferri-, or antiferromagnetic long-range ordering).

4.3.2.1. Crystal Synthesis and Structure

Single crystals of [Cu(μ-C$_2$O$_4$)(4-aminopyridine)$_2$(H$_2$O)]$_n$ typical size of 5×0.5×0.2 mm^3 (Fig. 58) were grown by A. V. Prokofiev from the Institute of Physics (Goethe University-Frankfurt), using the slow diffusion technique (details of the crystal growth are given in Ref. [197]). Most of the crystals have a form of needles with the shortest dimension in the crystallographic *a*-direction and the needle axis in *b*-direction.

Figure 58: Crystals of the polymer [Cu(*μ*-ox)(H$_2$O)(4-apy)$_2$]$_n$.

Single crystals of another habit grew alongside the plate-like and needle crystals of polymer [Cu(μ-ox)(H$_2$O)(4-apy)$_2$]$_n$. A structural study has shown the crystals to be a copper polymer which differs from polymer [Cu(μ-ox)(H$_2$O)(4-apy)$_2$]$_n$ by a bridging ligand: a carbonate group instead of oxalate ion [198].

The crystal structure of the polymer [Cu(μ-ox)(H$_2$O)(4-apy)$_2$]$_n$ was determined by Castillo *et al.* [181]. According to the structure analysis, C$_{12}$H$_{14}$CuN$_4$O$_5$ consists of polymeric neutral [Cu(μ-ox)(H$_2$O)(4-apy)$_2$] chains in which the metal atoms are bridged sequentially by oxalate anions, see Figure 59. The Cu^{2+} ion is placed on a 2-fold axis and has a distorted square-pyramidal environment, see Figure 61. The basal plane is formed by two symmetry-related oxygen atoms of two oxalato ligands [Cu-O: 2.004(3) Å] and the nitrogen atoms of two 4-apy ligands [Cu-N: 1.983(5) Å]. The 4 + 1 coordination sphere of the copper atom is completed by an apical oxygen atom from a water molecule with the Cu-O bond (2.315 Å) lying on a 2-fold axis. The copper atom is displaced from the mean basal plane towards the apical site by 0.08 Å. The polymeric chains run along the *c*-axis of the unit cell, and the basal plane is parallel with the *ac*-plane. The mean planes of the aromatic ligand and the oxalate are perpendicular to each other and with respect to the basal plane of the Cu^{2+} ion coordination pyramid.

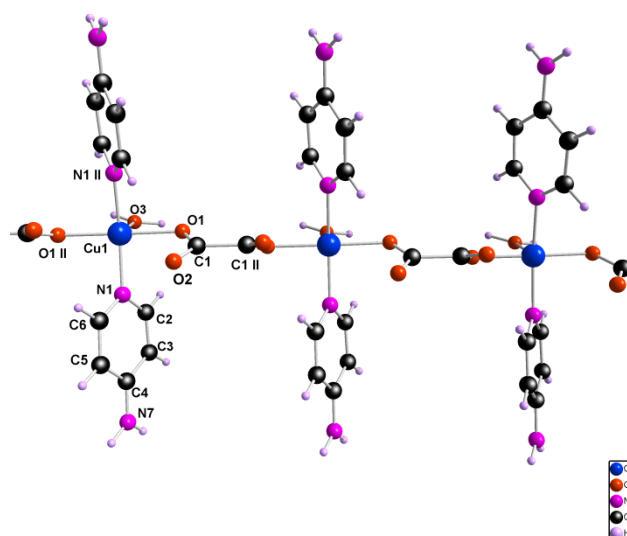Figure 59: Polymer chain of the Cu(μ-ox)(H$_2$O)(4-apy)$_2$].
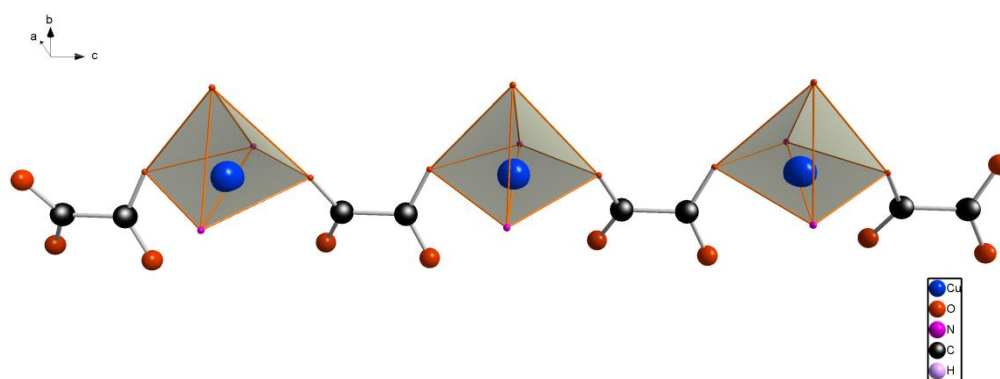
Figure 60: Coordination environment of the Cu^{2+} in a chain $[Cu(\mu\text{-ox})(H_2O)(4\text{-apy})_2]$.

The *intra*-chain Cu-Cu distance across the oxalato ligand is 6.752(1)Å, which is significantly longer than those published for dimeric and polynuclear complexes [< 6.0Å] [181], but within the range [6.5-8.1Å] found in other polymeric compounds with the oxalate bridge. The oxalato ligand is not planar and the two -CO$_2$ entities are twisted by 28° with respect to each other around the C-C bond. The bond C-O distance [1.272(6) Å] is only slightly longer than the C-O (free) one [1.235(7) Å] owing to the involvement of the free oxygen atoms in an extensive network of hydrogen bonds. Each water molecule forms two hydrogen bonds, related by a 2-fold axis, with two free oxygen atoms from the oxalato bridge belonging to a neighbouring chain, see Figure 61.
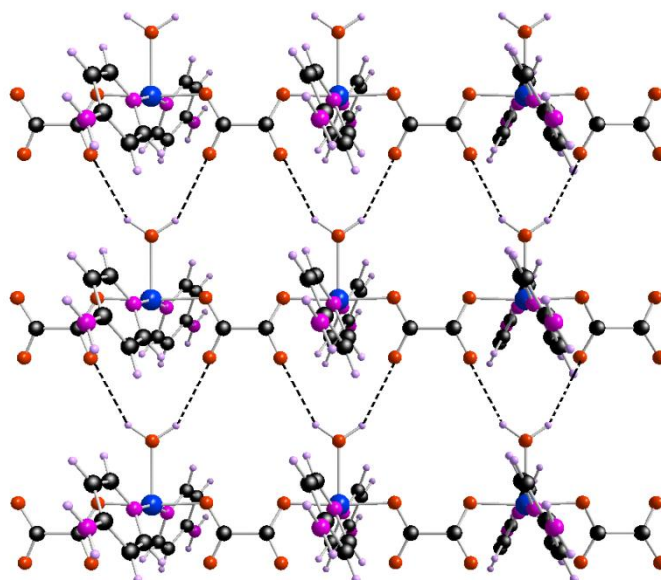

Figure 61: Sheets of chains $[Cu(\mu\text{-ox})(H_2O)(4\text{-apy})_2]$ formed by hydrogen-bonds (dashed lines) involving the coordinated water molecules.

The O_w-H-O interactions lead to the formation of hydrogen-bonded sheets parallel to the (100) plane. The shortest *inter*-chain Cu-Cu distance is 6.357(1)Å. No face-to-face π-π interactions between the aromatic rings have been found in the crystal structure.

4.3.2.2. DC susceptibility measurements

Magnetic susceptibility measurements were performed on the single crystals of $[Cu(\mu\text{-}C_2O_4)(4\text{-aminopyridine})_2(H_2O)]_n$ in the temperature range of 2-300K and in magnetic fields up to 1T. For temperatures $0.1K \leq T \leq 5.0K$, the susceptibility was determined by using an Oxford dilution refrigerator equipped with a SQUID magnetometer in a field of 0.002T. Ten single crystals of $[Cu(\mu\text{-}C_2O_4)(4\text{-aminopyridine})_2(H_2O)]_n$ with a total mass of 4.83mg were oriented and fixed on a sample holder with vacuum grease, see Figure 62. This arrangement was used for the experiments. The obtained data were corrected for the contribution of the sample holder $\chi_{holder} = 1.75 \cdot 10^{-4}$ cm³/mol and for the temperature-independent diamagnetic contribution χ_{diam} according to [95]. The samples had a needle-like shape with the *b*-axis along the needle direction.

Figure 62: Sample holder with the crystals oriented in the needle direction.

The magnetic susceptibility, per mol of the Cu^{2+} ions of $[Cu(\mu\text{-}C_2O_4)(4\text{-aminopyridine})_2(H_2O)]_n$ for the field along the needle direction (*b*-axis) and perpendicular to it, is shown in the main panel of Figure 63. The anisotropy of the magnetic susceptibility between both directions is consistent with the anisotropy of the *g*-values observed in the ESR measurements.
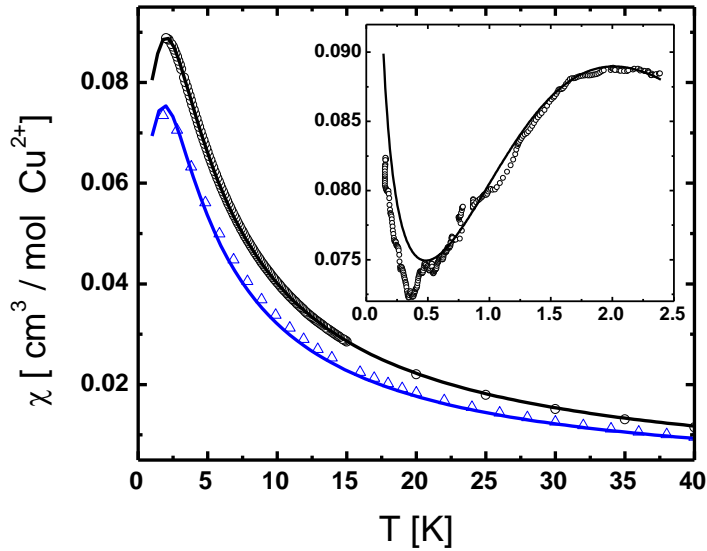
Figure 63: Temperature dependence of magnetic susceptibility χ_{mol} of $[Cu(\mu\text{-ox})(H_2O)(4\text{-apy})_2]_n$ for temperatures 2-40K in a magnetic field of 1T for two different orientations: parallel (circles) and perpendicular (triangles) to the *b*-axis. The solid lines correspond to the best fits for the model described in the text with an AF exchange coupling constant. The inset shows the low-temperature data together with the simulation with the parameters given in the text.

An incipient maximum is observed for both directions around 2K (see inset in Figure 63). The low-temperature data for the field parallel to the *b*-axis in the temperature range between 0.15K and 3K, shown in the inset of Figure 63, revealed the whole maximum. In addition, an increase of $\chi_{mol}(T)$ is observed below 0.4K. This low-temperature upturn can be attributed to paramagnetic moments resulting from a small amount of non-coupled spins in the sample. After subtraction of the paramagnetic Curie contribution from the experimental data, the $\chi_{mol}(T)$ shows the pronounced maximum around 2K and non-zero susceptibility as $T \rightarrow 0$. Such a magnetic behaviour indicates the existence of a weak antiferromagnetic (AF) interaction between the Cu^{2+} ions within the polymeric chain. The molar susceptibility, shown in Figure 63, is typical for a 1D spin system governed by short-range spin correlations. A model, where the system is composed of isolated AF Heisenberg chains, was used for the quantitative discussion of the susceptibility data. This model is consistent with the crystal structure. The observed temperature dependence of χ_{mol} is described as:

$$\chi_{mol}(T) = \chi_{chain}(T) + \chi_C(T) \tag{61}$$

where χ_{chain} is the susceptibility of the uniform Heisenberg spin chain, given by an empirical rational function according to [153] and $\chi_C = C/T$ is the Curie susceptibility arising from the non-coupled spins in the system. The Hamiltonian being used for the χ_{chain} is given in Equation 19. From a fit of the data for the temperature range 2-40K , see Figure 63, where the

intra-chain magnetic exchange coupling constant J between the Cu^{2+} ions and their concentration (1-n) as free parameters are used (with n denoting the percentage of uncoupled spins), a good description of the data is achieved with the following numbers: $J/k_B = (3.4 \pm 0.1)$K, $n = (0.7 \pm 0.3)$% for the field parallel to *b*-axis and $J/k_B = (3.2 \pm 0.1)$K, $n = (0.6 \pm 0.3)$ % for the field *B* normal to *b*-axis. The *g*-values were taken from the ESR experiments. For the external field normal to *b*-axis, an averaged value of g_a and g_c of 2.05 ± 0.01 was used. The small concentration n of uncoupled $S = \frac{1}{2}$ moments reflects the high quality of the present single crystals.

The inset of Figure 63 displays the low-temperature data for temperatures 0.1K $\leq T \leq 2.4$K (open circles), together with a calculation (solid line) according to Equation 61 using the magnetic coupling constant J and the concentration determined from the high-temperature data. Good agreement between the experimental data and the calculation is clearly visible.

4.3.2.3. ESR measurements

Single crystal ESR experiments of the $[Cu(\mu\text{-}C_2O_4)(4\text{-aminopyridine})_2(H_2O)]_n$ were performed with a specially designed spectrometer using a frequency of $v = 56.039 \text{GHz}$ at a temperature $T = 1.54K$ and in an applied field of up to 2.5T. In order to obtain information on a possible magnetic anisotropy of $[Cu(\mu\text{-}C_2O_4)(4\text{-aminopyridine})_2(H_2O)]_n$, the measurements were carried out at temperatures down to 1.5K and in an applied field of up to 2.5T with a different field orientation. The ESR measurements at a temperature $T = 1.54K$ detect one magnetic center of copper ion at any orientation of the sample with respect to the applied magnetic field; see Figure 64 and Figure 66.

Figure 64: Angular dependence of the ESR resonance line for a single crystal of $[Cu(\mu\text{-}ox)(H_2O)(4\text{-apy})_2]_n$ at 1.54K in a *bc*-plane in steps of 10°. Resonance lines are shifted vertically for clarity.

This magnetic center has an axial anisotropy in the *bc*-plane with the *g*-values in the range of 2.01 - 2.33 at $T = 1.54K$, see Figure 65.

Figure 65: Angular dependence within the *bc*-plane of the resonance field (left axis) and the corresponding *g*-tensor values (right scale).

The ESR spectrum for the *ba**-plane is displayed in Figure 66. The results show clear resonance absorption lines, and demonstrate that $[Cu(\mu\text{-}C_2O_4)(4\text{-aminopyridine})_2(H_2O)]_n$ has a negligible magnetic anisotropy.
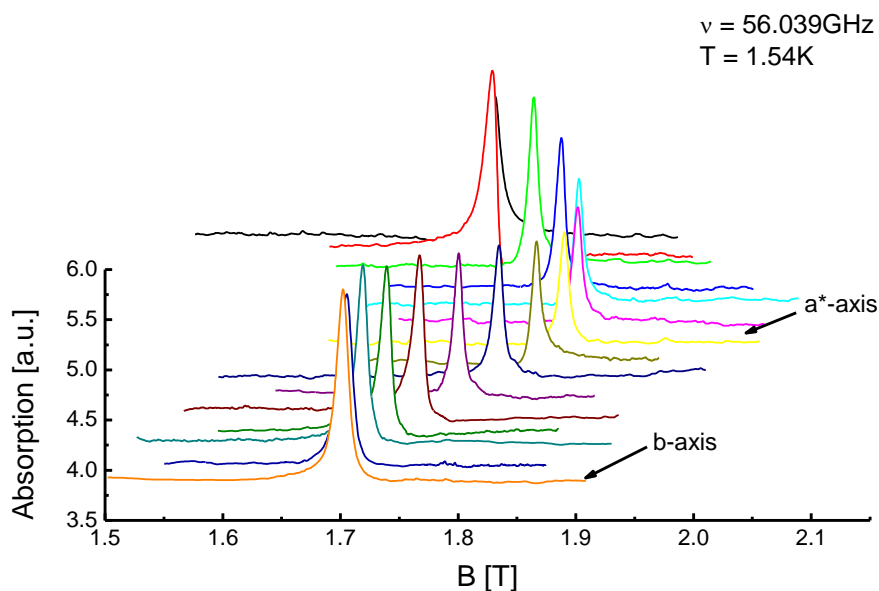
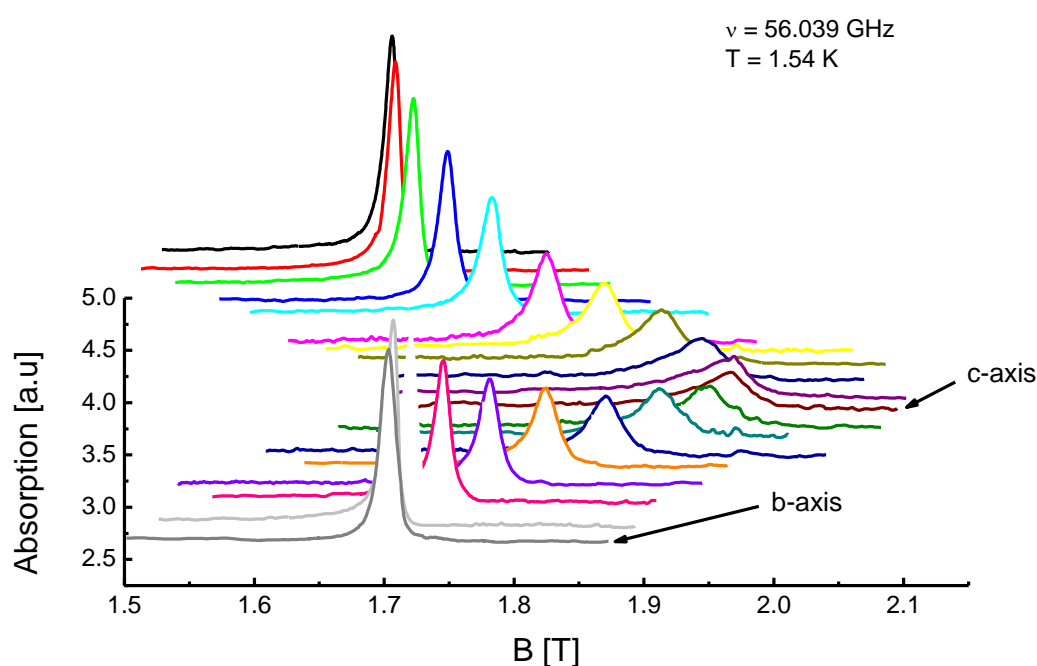Figure 66: Angular dependence of the ESR resonance line for a single crystal of $[Cu(\mu\text{-}ox)(H_2O)(4\text{-apy})_2]_n$ at 1.54K in a *ba**-plane in a steps of 10°. Resonance lines are shifted for clarity.

The axial anisotropy of the Cu^{2+} magnetic center in the *ba**-plane with the *g*-values in the range of 2.08 - 2.33 at $T = 1.54K$ is shown in Figure 67.
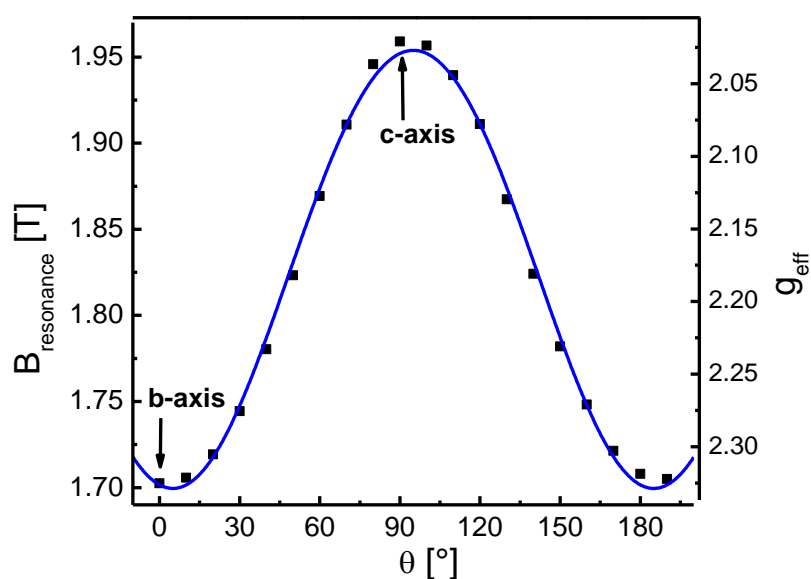

Figure 67: Angular dependence within the *ba**-plane of the resonance field (left axis) and the corresponding *g*-tensor values (right scale).

The local magnetic axes of Cu^{2+} are almost perpendicular to each other. The axial anisotropy is in accordance with the local environment of the $[Cu(\mu\text{-ox})(H_2O)(4\text{-apy})_2]_n$ compound determined by the X-ray crystal structure analysis.

4.3.2.4. AC susceptibility measurements

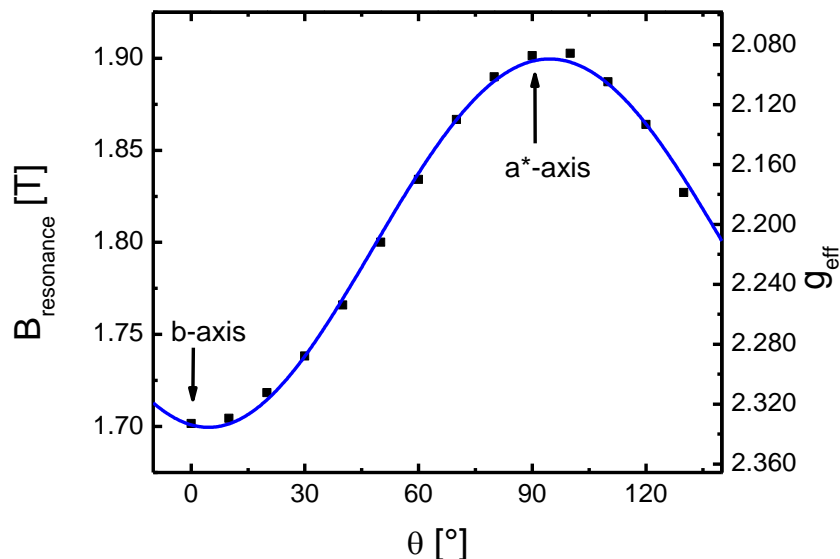The *ac*-susceptibility (χ_{ac}) of a single crystal of [Cu(μ-ox)(H$_2$O)(4-apy)$_2$]$_n$ was measured as a function of field $\chi_{ac}(B)$ and temperature $\chi_{ac}(T)$. The crystal was oriented such that the *b*-axis is parallel to the applied field. Measurements were performed by using a state-of-the-art compensated-coil susceptometer. Empty-coil measurements were performed as a direct measure of the sample-independent background. Selections of $\chi_{ac}(B)$ are shown in Figure 68.
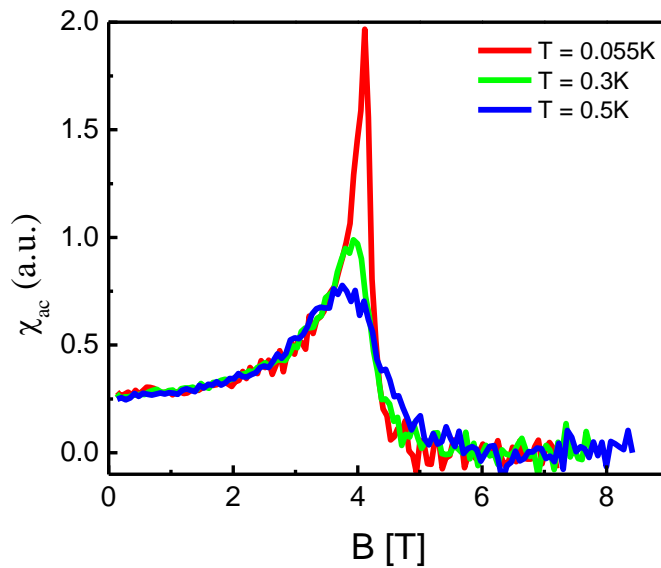

Figure 68: χ_{ac} as a function of applied field at different temperatures. The position of the sharp feature in χ_{ac} (*B*) becomes clearer with decreasing of temperature.

No hysteresis behaviour has been found upon increasing and decreasing the field. For temperatures below ~ 1K, $\chi_{ac}(B)$ has one field-induced feature. According to the theory [106], this field-induced structure indicates the field (B_s) where the system enters the fully polarized state. Upon cooling, the drop becomes sharper and tends to diverge. From these measurements, the critical field at 0K is estimated to be $B_s \approx 4.1$T. It should be noted that B_s deduced from $\chi_{ac}(B)$ is lower than the value predicted by the $S = \frac{1}{2}$ AFHC (4.3T). This difference is presumably due to the error bar in the value of the exchange interaction J/k_B, obtained from *dc*-susceptibility measurements. The isothermal magnetization (*M*), obtained by integrating the corresponding χ_{ac} data, together with the thermodynamic Bethe ansatz calculations [106], based on the exchange coupling constant $J/k_B = 3.2(1)$K and $g = 2.33$, are shown in Figure 69.
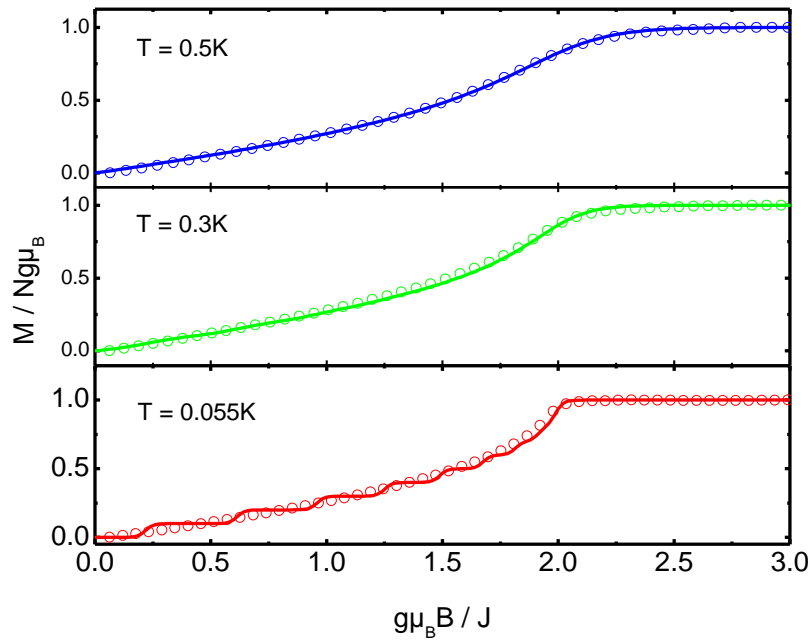
Figure 69: Field dependence of magnetization at $T = 0.5$K, $T = 0.3$K and $T = 0.055$K. Open circles are experimental data, solid curves are the thermodynamic Bethe ansatz calculations using $J/k_B = 3.2(1)$K and $g = 2.33$. Oscillations in the Bethe ansatz calculations at $T = 0.055$K are due to finite-size effects.

The good agreement between the experimental data and the calculations suggest that the system represents an excellent model system for a uniform $S = \frac{1}{2}$ AFHC.

According to theory, the magnetic susceptibility for $T < 0.32$K should be dominated by the logarithmic correction, see Equation 26. A rapid decrease of the susceptibility is expected to occur below 0.03K, considering the J/k_B value 3.2(1)K. Comparison between the experimental data and the Bethe ansatz calculation for $J/k_B = 3.2(1)$K and $T_0 \approx 7.7$ J/k_B is shown in Figure 70. The experimental $\chi(T)$ shows a steep decrease at around 0.15K with a minimum value 6.8×10^{-2} emu/mol, whereas the Bethe ansatz calculation shows a rapid decrease at 0.03K and reaches 7.1×10^{-2} emu/mol for $T \rightarrow 0$K. Considering the qualitative similarities, the isotropic drop in $\chi(T)$ at low temperature might indicate the asymptotic $(\ln T)^{-1}$ term revealed by the Bethe ansatz. As can be seen, the experimental and theoretical results coincide very well in the temperature range above ~ 0.1K. In the lowest temperature range, the coincidence is not as good. The reason for the rapid drop of χ_{ac} at low temperatures is unclear at present and requires further investigations.

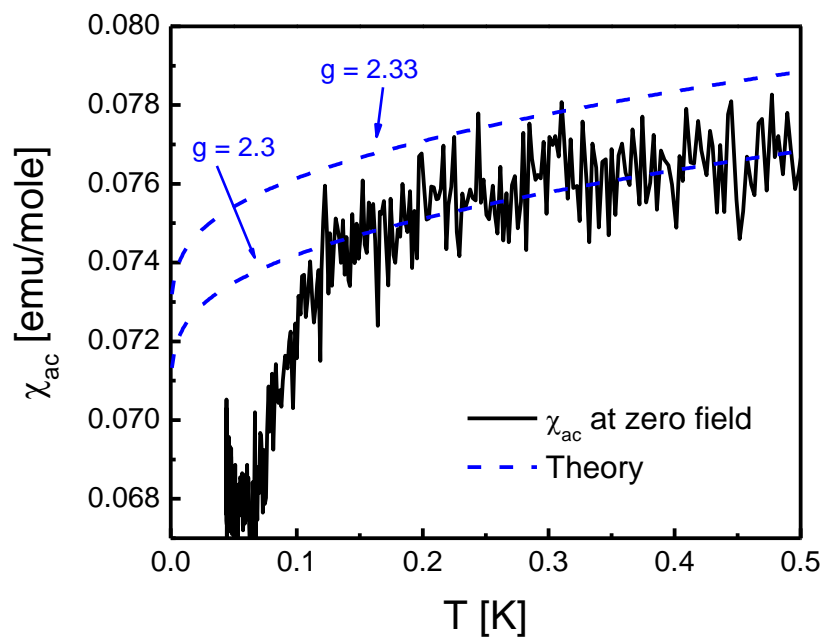Figure 70: $\chi(T)$ for [Cu(μ-ox)(H$_2$O)(4-apy)$_2$]$_n$ (solid line) compared to theoretical calculations by $2J\pi^2\chi(T) = 1 + 1/[2\ln(15.4J/T)]$ with $J/k_B = 3.2(1)$K and $g = 2.3$ and $g = 2.33$ (dash line) in the temperature range below 0.5K.

4.3.2.5. Specific heat measurements

The specific heat measurements were performed by G. Donath from the Max-Planck-Institute for Chemical Physics of Solids (Dresden). The sample was composed of several single crystals, the *ac*-planes of which were aligned parallel to the applied field, and a total mass of 36.3 mg.

The temperature dependence of the specific heat in zero magnetic field in the full temperature range 0.2-4K, see Figure 71, can be well described as a sum of the magnetic contribution to the specific heat of the uniform $S = ½$ AFHC, $C_{magnetic}$, derived from the thermodynamic Bethe ansatz calculations [106], and the low-temperature phonon contribution - a term proportional to T^3:

$$C(T) = C_{magnetic} + C_{phonon} \tag{62}$$

$$C_{magnetic} = C_{theory}$$

$$C_{phonon} = B \cdot T^3$$

with $C_{magnetic}$ calculated for $g = 2.33$ and $J/k_B = 3.2(1)$K, and $B = 0.003$ Jmol^{-1}K^{-3} derived from a least-squares fit to the data at 0.15T. The phonon contribution was subtracted from all the data, and Figure 72 shows the resulting magnetic contribution to the specific heat in $B = 0.15$T in the low-temperature range. The linear dispersion relation of the fermionic spinons at low energy implies that the low-temperature specific heat of the $S = ½$ AFHC should be linear in T. It is given by Equation 28. The linear T-behaviour of the magnetic specific heat observed in zero field for $k_B T / J < 0.08$, is accompanied with the slope 0.64(1). Discrepancy between the theoretical value 0.7 given by Equation 27 [107] and experiment may be the consequence of the Dzyaloshinskii-Moriya interaction in the system (a fact which has yet to be investigated) or the error bar of the exchange interaction.
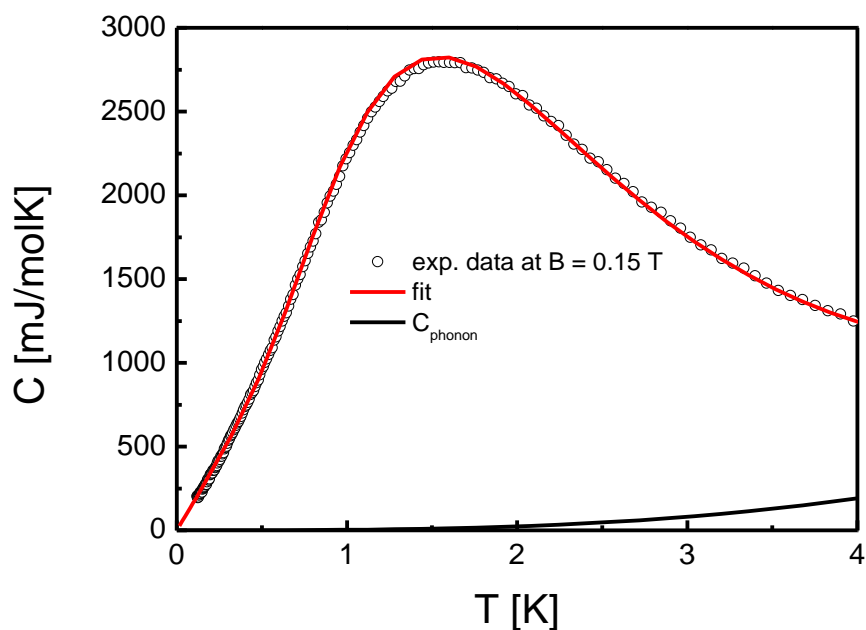
Figure 71: Specific heat of $[Cu(\mu\text{-ox})(H_2O)(4\text{-apy})_2]_n$ vs. T at constant magnetic field $B = 0.15T$, the solid red line is a fit to an exact diagonalization model as described in the text. The solid black line is the phonon contribution determined from the fit.
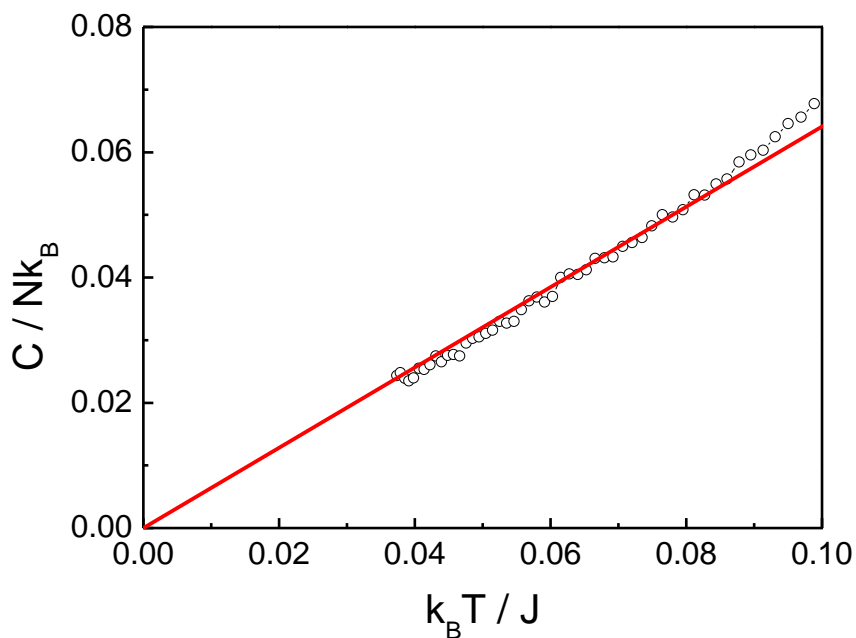
Figure 72: Magnetic heat capacity C of $[Cu(\mu\text{-ox})(H_2O)(4\text{-apy})_2]_n$ vs. T in $B = 0.15T$ (after subtraction of phonon contribution), the red solid line is a linear fit as described in the text.

The temperature dependence of the total specific heat of $[Cu(\mu\text{-ox})(H_2O)(4\text{-apy})_2]_n$ for a number of magnetic fields B is shown in Figure 73. As the magnetic field B is increased, the broad maximum observed in zero field is suppressed, and gradually shifts to lower T. The solid lines are the results of a calculations based on the thermodynamic Bethe ansatz calculations [106], as described below with the phonon contribution used as a fit parameter. The dashed line is the phonon contribution determined from the fit.

The theory curves were provided by A. Honecker from the Institute for the Theoretical Physics (Georg-August-University, Göttingen), based on Bethe ansatz calculations in [106]. All experimental data shown on Figure 73 were fit simultaneously to the expression:

$$C(T) = C_{magnetic} + C_{phonon} = AC_{theory}(J,T) + BT^3 \tag{63}$$
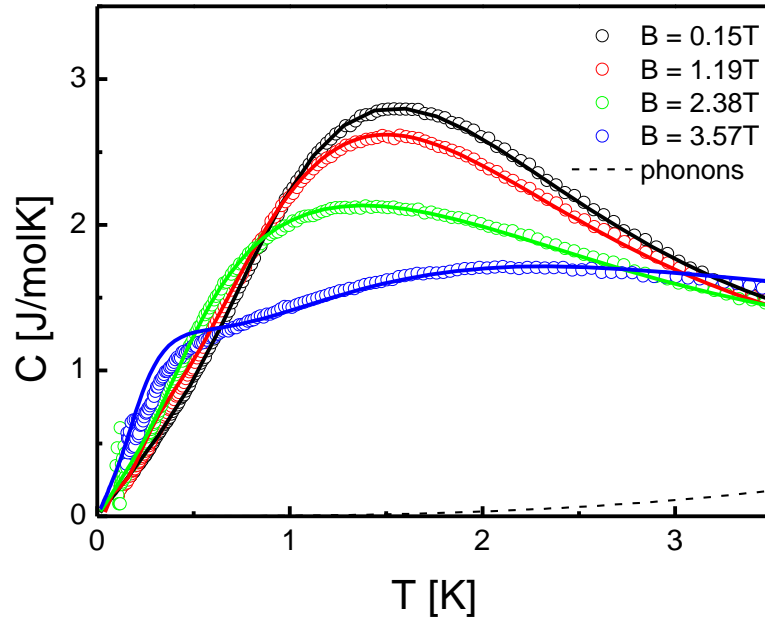
Figure 73: Specific heat of $[Cu(\mu\text{-ox})(H_2O)(4\text{-apy})_2]_n$ vs. T at constant magnetic field 0.15T, 1.19T, 2.38T and 3.57T. Solid lines are a fit to an exact numerical and analytical model as described in the text. The dashed line is the phonon contribution determined from the fit.

The $S = \frac{1}{2}$ AFHC model accounts for the data very well, with $A = 0.96(1)$, $J/k_B = 3.2(1)$K, and $B = 4.1(1)$ mJ/molK^4. The deviation of A from 1 can be assigned to a systematic error in the normalization of specific heat data.

An expanded view of the experimental data in Figure 73 for $T < 0.55$K and fields $B \leq 2.38$T is shown in Figure 74, plotted as C/T vs. T^2. Predominantly linear behaviour of the specific heat in T including the small positive slope is observed. The positive slope is caused by the field-induced shift of spectral weight to lower temperature. An increase of the slope with field is also visible.
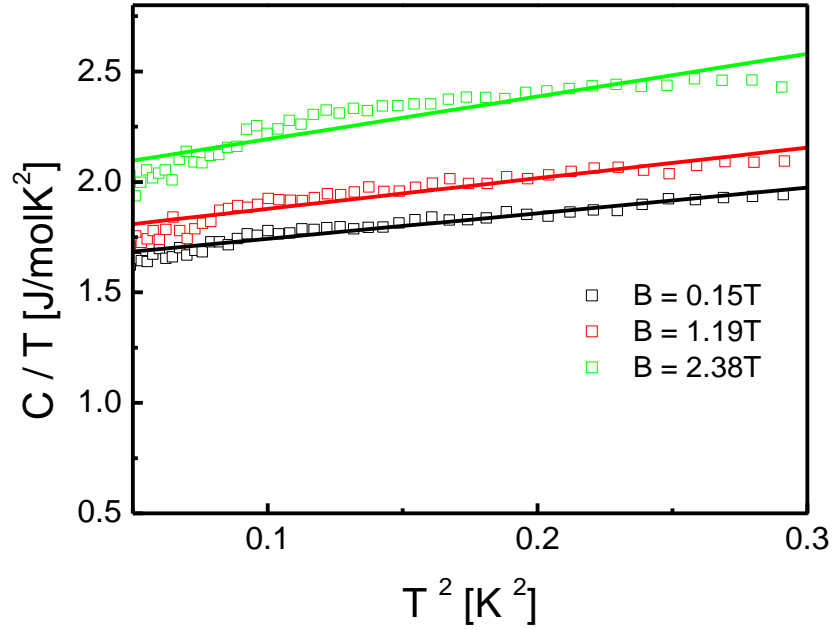
Figure 74: Specific heat of [Cu(μ-ox)(H$_2$O)(4-apy)$_2$]$_n$ below $T < 0.55$ K, plotted as C/T vs. T^2 for constant magnetic field 0.15T, 1.19 T and 2.38 T.

As mentioned in Chapter 2.3.1, the low-temperature specific heat of the $S = \frac{1}{2}$ AFHC is linear in T and is given by Equation 28. There, $v_s(B)$ is the field-dependent spinon velocity, which in zero field takes the form $v_s = \frac{\pi J}{2}$. Correspondingly the specific heat can be described by Equation 27, a result which has been confirmed experimentally [199, 200]. According to the theory, $v_s(B)$ decreases with the field and goes to zero as the system approaches the critical field. On the other side, the Sommerfeld constant γ_B, given by $\gamma_B = \frac{\pi}{3} R \frac{k_B}{v_S(B)}$, increase with the field. This means that the slope of the linear T dependence of the specific heat also increases with the field. Figure 74 shows exactly such a behaviour and provides direct experimental evidence of the spin velocity behaviour in the $S = \frac{1}{2}$ AFHC and indicates a renormalization of the spinon velocity with field.

In the case of the existence of a field-induced gap $\Delta(B)$ in the system, one should observe a suppression of C below its zero-field value in finite fields and at low temperatures $T << \Delta/k_B$. Such a signature was not observed in the experiment (*ac*-susceptibility) down to $T = 50$mK. It is possible that the field-induced gap exists but its value would be smaller than 50mK.

As described in Chapter 2.3.1, some qualitative aspects of the specific heat in finite external field can be understood in the picture of spinon excitations. The external magnetic field acts like a chemical potential for the spinons (for which there are particle-hole like excitations). At zero field, the bands of the particle- and hole-like excitations are identical,

and for a sufficiently strong field B, the band widths are considerably different resulting in two maxima in the specific heat at different temperatures (see the theory curves at the Figure 75). For fields stronger than the saturation field $B > B_s$, an energy gap opens in the ferromagnetically polarized state.
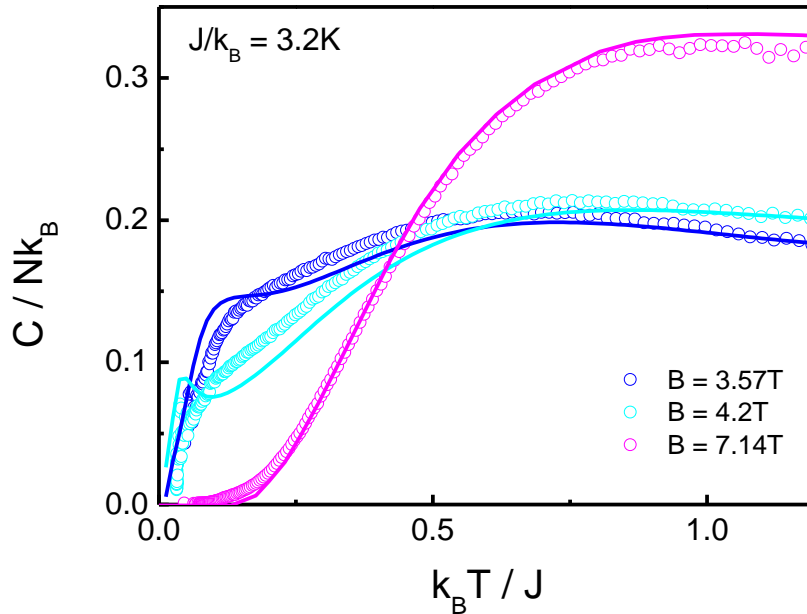
Figure 75: Temperature dependence of the specific heat of $[Cu(\mu\text{-ox})(H_2O)(4\text{-apy})_2]_n$ for different values of the external field. The solid curves are the thermodynamic Bethe ansatz calculations [106].

The agreement between the experiment and theory is reasonably good for fields lower than the saturation field at low temperatures as well as in the high-temperature region. The in-T linear behaviour of C for fields lower than the saturation field is obvious. The discrepancy between the experiment and theory is explicit for the field $B = 3.57T$ close to the saturation field and for the field higher than the saturation field $B = 4.2T$, especially in the low-temperature region, see Figure 75. The high-temperature region for the latter two field values overlaps quite well with the theoretical predictions. However, the low-temperature maximum, expected by theory, is not well pronounced. Here, one can observe only a shoulder in the specific heat data. Part of this discrepancy can be related to the arbitrary orientation within the ac-plane of the crystals with respect to the field, giving rise to a smearing of the maximum. Above the saturation field, the overlap between the theoretical prediction and experimental data is very good. Such a good agreement between the C data and theory gives

further credibility to the conclusion that [Cu(μ-ox)(H$_2$O)(4-apy)$_2$]$_n$ is a very good realization of a uniform $S = \frac{1}{2}$ AFHC.

4.3.2.6. Magnetocaloric effect measurements

The magnetocaloric effect measurements were performed by Y. Tsui from the Institute of Physics (Goethe University-Frankfurt). Measurements of the MCE were performed on several single crystals attached to the calorimeter by first applying a small amount of Apiezon N-grease. The calorimeter consists of a sapphire plate ($5\times5\times0.3$ mm^3) and a RuO_2 resistor, which served as a thermometer. The external field was parallel to the b-axis of each crystal. First, the standard MCE measurements on a single-crystalline sample were performed by monitoring the change of the sample temperature T while sweeping the external magnetic field continuously at the rate 0.1T/min. The field dependence of T for the up-sweep data is plotted in Figure 76. In general, $T(B)$ decreases slowly as B initially rises. Then it reaches a minimum at $B \sim 4.1$T and starts to increase much more rapidly when B goes up further. The minimum becomes sharper and moves to a higher field as the temperature drops. These results are consistent with the theoretical calculations [122].
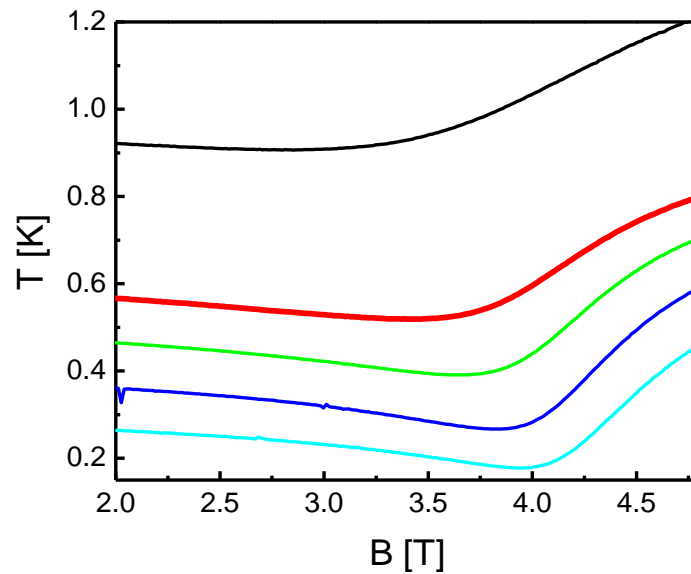
Figure 76: Change of the sample temperature T as the external magnetic field was increasing. The initial temperature of the sample was $T = 0.9$K (black line), $T = 0.59$K (red line), $T = 0.45$K (green line), $T = 0.33$K (blue line) and $T = 0.3$K (cyan line).

As discussed in Chapter 3.2.3., the thermal relaxation time constant (τ) of the calorimeter to the bath temperature is about 1000s at low temperatures. Therefore, the time (t_{sweep}) required to accomplish a field sweep shown in Figure 76 is about 2τ. Hence, the curves displayed in Figure 76 do not represent the real MCE, requiring the experimental condition $t_{sweep} \ll \tau$, which makes a quantitative comparison with the theory difficult. In order to measure the MCE of the sample as accurately as possible, a modified technique was used. At

a fixed bath temperature T_b and the sample initially in thermal equilibrium with the bath, the field was swept in small steps of $\Delta B \leq 20$mT and the corresponding variation of the sample temperature, ΔT, was recorded, see Figure 77.
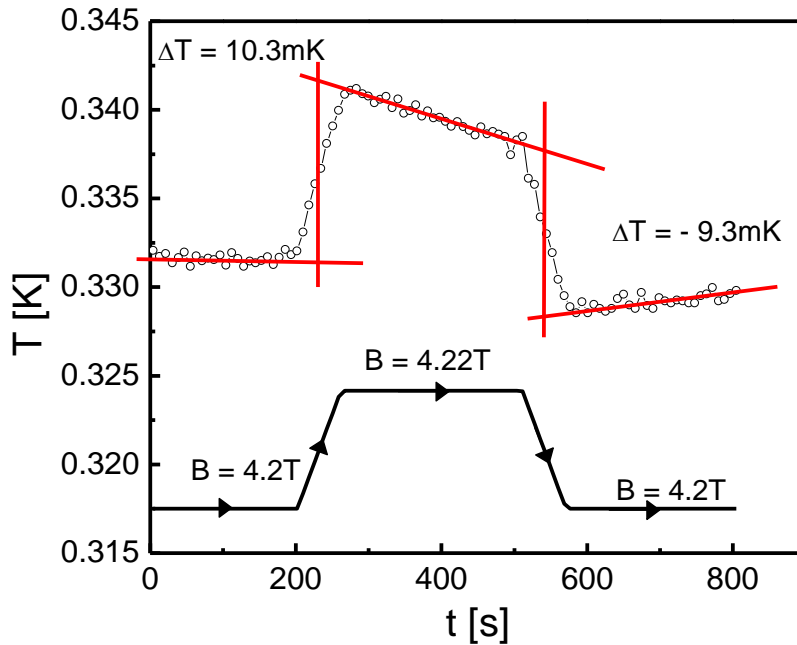
Figure 77: An example of a temperature-profile for a single MCE measurement with reduced signal-to-noise ratio (at an early stage of the experiment development). The sample was at thermal equilibrium with the bath and at $B = 4.2$T. The field was then swept to 4.22T in 60s. After roughly 200s, the field was swept back to 4.2T within 60s.

The sweep time for the change of ΔB was kept within 60s, which was small enough to ensure quasi-adiabatic conditions and big enough to give a measurable ΔT. The effect from eddy-current heating in the metallic part of the calorimeter was eliminated by sweeping the field up and down and taking the average value of the corresponding ΔT. An example of such a sequence of field sweeps is plotted in Figure 77. As shown in the figure, there is a sign change in ΔT as the direction of the field sweep reverses and ΔT for the up-sweep and down-sweep data are very close. This shows that heating, due to other processes, such as eddy current heating, was not significant during the measurements. It is worth noting that T relaxed very slowly towards the bath temperature after the change of the external field. Hence, the temperature change caused by the relaxation to the bath was much less than that due to the MCE during the field sweeps. Therefore, we can conclude that the measured ΔT was mostly caused by the MCE. By improving the experimental setup a rigorous comparison between experimental results and theoretical calculations on a uniform $S = \frac{1}{2}$ AFHC now has become possible. The MCE (Γ_B) was calculated according to Equation 43 and plotted in Figure 78.

As can be seen upon increasing the field, the MCE shows a characteristic sign change close to the saturation field. The sign change of Γ_B reflects a maximum in the finite-temperature entropy in the vicinity of the saturation field. As already discussed in Chapter 2.4., an accumulation of entropy is expected near a QCP since, directly at the QCP, the system is frustrated due to the competing ground states. The solid lines in Figure 78 are the result of quantum Monte Carlo calculations and exact diagonalization for the $S = ½$ AFHC for $J/k_B = 3.2$K and the appropriate g-factor. The agreement between experimental data and theory is quite good. The small deviations between experiment data and theory, which grow with increasing field, might indicate an opening of a small B-induced gap. The field-induced gap may result from a finite Dzyaloshinskii-Moriya interaction (a fact which has not been proved until now), permitted by the lack of a center of inversion symmetry in its crystal structure. The existence of a field-induced gap would tune the system progressively away from quantum criticality (entropy is shifted to higher fields). This behaviour is consistent with the experimental observations.
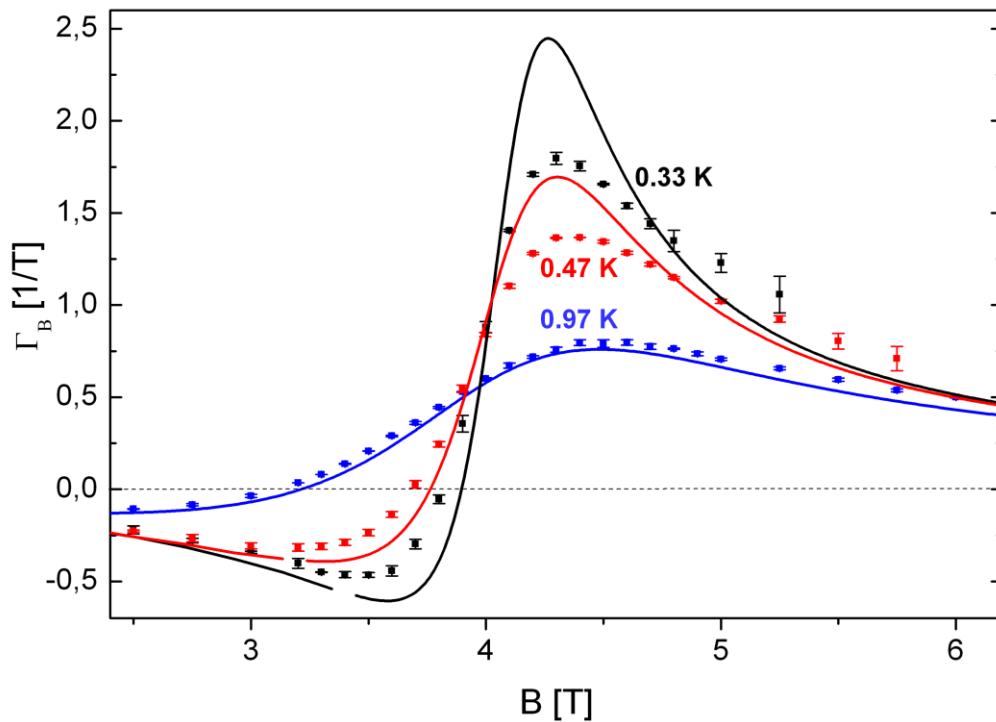

Figure 78: Magnetocaloric effect-Γ_B as a function of field at different temperatures. Data were taken with an improved experimental setup. Solid lines are the results of quantum Monte Carlo simulations and exact diagonalization from A. Honecker [122].

4.3.2.7. Summary

Single crystals of the polymer $[Cu(\mu\text{-}ox)(H_2O)(4\text{-}apy)_2]_n$ have been grown using a slow-diffusion technique with a monoammine copper complex and a ligand mixture solutions. The size of the crystals is typically $5\times0.5\times0.2$ mm^3. As is demonstrated in Figure 65, Cu^{2+} ions have a distorted square-pyramidal environment and are bridged by an oxalate linker to form chains along the c-axis of the unit cell. The *intra*-chain Cu-Cu distance across the oxalate bridge is significantly longer than those described and published for dimeric and polynuclear complexes with oxalate bridges, but within the range found in polymeric compounds in which the oxalate bridge is bound to the two metal centers by two oxygen atoms. The oxalate bridge is not planar and the two -CO$_2$ entities are twisted by 28° with respect to each other around the C-C bond. Such an unusual configuration of the oxalate bridge in the $[Cu(\mu\text{-}ox)(H_2O)(4\text{-}apy)_2]_n$ polymer enables the formation of a moderate antiferromagnetic exchange interaction between the Cu^{2+} ions within the chain. The hydrogen bonds between the chains help to enable the formation of the 2D structure in the (100) plane but, considering the path of the *inter*-chain interaction, this should be weaker than the *intra*-chain one. From the structural point of view, the $[Cu(\mu\text{-}ox)(H_2O)(4\text{-}apy)_2]_n$ compound should behave in the same way as a $S = \frac{1}{2}$ Heisenberg chain.

Magnetic measurements (DC susceptibility measurements) confirm the applicability of the model of the AF Heisenberg chain and enable the value of the *intra*-chain exchange coupling to be determined to $J/k_B = 3.2(1)$K.

ESR measurements suggest a negligible magnetic anisotropy around the Cu^{2+} ion with g-tensor values $g_b = 2.33$, $g_c = 2.01$, $g_{a*} = 2.08$ and $<g> = 2.14$, this value indicates a $d_{(x2\text{-}y2)}$ ground state and is in accordance with the square-pyramidal geometry of the Cu^{2+} ion.

AC susceptibility measurements taken at temperatures down to 0.055K and a magnetic field up to 8.5 T revealed that the saturation field of the system is around 4.1T. When compared with the theoretical calculations, the magnetization data showed good agreement and confirmed the magnetic exchange interaction between nearest-neighbour spins to be $J/k_B = 3.2(1)$K, indicating that the magnetic system $[Cu(\mu\text{-}ox)(H_2O)(4\text{-}apy)_2]_n$ is an excellent model system for a uniform $S = \frac{1}{2}$ AFHC.

Specific heat data in magnetic field show that the data qualitatively agree very well with the rigorous numerical calculations, for the magnetic exchange interaction between nearest-neighbour spins of $J/k_B = 3.2(1)$K and g-factor values $g = 2.33$. The excellent agreement between the specific heat data and theory gives further credibility to the conclusion that $[Cu(\mu\text{-}ox)(H_2O)(4\text{-}apy)_2]_n$ is a very good realization of a uniform $S = \frac{1}{2}$ AFHC.

The measurements of the magnetocaloric effect presented in this work provide the first experimental demonstration of the critical behaviour of the MCE of a uniform $S = \frac{1}{2}$ AFHC when the external field is swept across the saturation field. Measurements of the magnetocaloric effect at low temperatures across the saturation field yield a very large MCE response with a characteristic sign change close to the quantum critical point. The data are in

good agreement with the quantum critical behaviour calculated on the basis of exact diagonalization and quantum Monte Carlo simulations for $J/k_B = 3.2$K and $g = 2.33$. The MCE measurements demonstrated that $[Cu(\mu\text{-ox})(H_2O)(4\text{-apy})_2]_n$ is an ideal model system for a uniform $S = \frac{1}{2}$ AFHC.

5. Conclusion and Outlook

Low-dimensional quantum spin systems have been intensively studied theoretically and experimentally in the last decades due to the wealth of exciting phenomena originating from reduced dimensionality. From the theoretical point of view, the great interest, increasing during recent decades, entered on the understanding of magnetic phenomena on the qualitative level, and developing models which are exactly solvable, providing insight into quantum many-body effects. On the experimental side, the major interests in the low-dimensional spin systems stem from the discovery of the high-temperature superconductor in the mid-eighties. High-temperature superconductivity in the cuprates raises the question of the link between the superconductivity and spin fluctuations and magnetic order in one- and two-dimensional spin- ½ antiferromagnets, and in order to get better insight of the problematic, a wealth of the magnetic systems with reduced dimensionality has been created. The new magnetic materials, on their own, have exhibited a wealth of new quantum phenomena such as Luttinger liquid behavior in one-dimensional systems, and a wealth of new states of matter such as valence bond solids, magnetic plateaux, spin-liquid states or spin-Pearls states, etc. In all these new low-dimensional magnetic materials interplay of low dimensionality, competing interactions and strong quantum fluctuations generate exotic and exciting magnetic phenomena. An example of high current interest is the realization of a Bose-Einstein condensation (BEC) of magnetic excitations in three-dimensionally (3D) and two-dimensionally (2D) coupled spin-dimer systems. Other examples are quantum critical phenomena observed in systems such as heavy fermion materials, two-dimensional electron gases and magnetic insulators. In these systems, the presence of zero-temperature quantum critical point (QCPs) holds the key to the unusual behavior found in the systems. The extraordinarily interesting quantum critical system is the spin $S = ½$ antiferromagnetic Heisenberg chain, which is inherently quantum critical. Fine-tuning of the magnetic field drives the system to a QCP which gives rise to unusual behaviour in the thermodynamics of the system. Particularly interesting is the proposed divergence of the magnetocaloric effect (MCE) at such a *B*-induced QCP.

In this thesis, low-dimensional spin systems $((CH_3)_3NCH_2COO)_3MnMCl_4$ with $M = Mn^{2+}$, Co^{2+}, Zn^{2+}, $((CH_3)_3NCH_2COO)_2 \cdot 3CuCl2 \cdot 2H_2O$, $C_{36}H_{48}Cu_2F_6N_8O_{12}S_2 - TK91$, $Cu(ox)(pyOH) \cdot H_2O$ and $[Cu(\mu-C_2O_4)(4\text{-aminopyridine})_2(H_2O)]_n$, have been investigated and discussed. All systems are metal-organic compounds consisting of magnetic transition metal ions bridged by organic molecules (CO_2 - carboxylate, C_2O_4 - oxalate) and side organic ligand (betaine, aminopyridine, hidroquinone) in low-dimensional structures.

$((CH_3)_3NCH_2COO)_3MnMCl_4$ with $M = Mn^{2+}$, Co^{2+}, Zn^{2+}

The three isomorphous compounds $3b \cdot MnCl_2 \cdot MCl_2$ with $M = Mn^{2+}$, Co^{2+}, Zn^{2+} (BMM, BMC and BMZ) have three different cation sites, two in octahedral and one in tetrahedral coordination. Isomorphic replacement takes place on the tetrahedral site leaving

the octahedral chains occupied by manganese in all three compounds. The common feature of all three compounds is the chain of carboxylate-bridged Mn^{2+} ions ($S = 5/2$), which are coupled antiferromagnetically. The Mn-Zn compound (BMZ) is the only one where the magnetic properties of the chains are seen in pure form. In BMM and BMC, on the other hand, the chain contribution could be seen after subtracting the paramagnetic contribution of the isolated spins in the $MnCl_4$ tetrahedra. The magnetic properties of all three compounds BMZ, BMM and BMC are well described by an independent Heisenberg spin chains model, where the chains are formed by octahedrally coordinated Mn^{2+} ions with $S = 5/2$. The weak antiferromagnetic *intra*-chain coupling of $J/k_B = -3K$, for all three compounds, is provided by the π-electron system of the carboxylate groups at the ends of the betaine molecules. The metal ions on the tetrahedral positions are magnetically isolated and have no impact on the magnetic properties of the spin chains.

$((CH_3)_3NCH_2COO)_2 \cdot 3CuCl_2 \cdot 2H_2O$ or $2b \cdot 3CuCl_2 \cdot 2H_2O$

$2b \cdot 3CuCl_2 \cdot 2H_2O$ is a trinuclear copper compound which presents the realization of the layered quasi-2D system. The layered structure is built from magnetic Cu^{2+} ions connected via a strong network of O-H⋯Cl hydrogen bonds. The magnetic susceptibility and isothermal magnetization showed the low-dimensional magnetic character of the spin system. Using a theoretical model of 2D coupled trimers, the antiferromagnetic *intra*-trimer coupling constant $J/k_B = -15K$ and the *inter*-trimer coupling constants $J_{a,b}/k_B = -4K$ were extracted. For Cu^{2+} ions linked by the carboxylate in a nearly planar coordination, this antiferromagnetic *intra*-trimer coupling constant appears surprisingly small, when it is known that the Cu coordination planes are tilted against each other, so significant reduction of the magnetic coupling constant would be expected. On the other hand, the antiferromagnetic *inter*-trimer coupling constant has an unexpectedly large value, which can be understood when one takes into consideration that hydrogen bonds may serve not only as a linker between the spin carriers but as a magnetic bridge. The lowest-order perturbation theory showed that the resulting effective *inter*-trimer coupling J_{eff} becomes ferromagnetic if $J_b < J_a/2$. The model suggested that for certain ranges of the ratio J_b/J_a, non-trivial four-spin exchange processes dominate over the usual next-neighbor exchange interactions.

It remains to be seen to which extent the ratio J_b/J_a in $2b \cdot 3CuCl_2 \cdot 2H_2O$ can be influenced by chemical substitution and/or hydrostatic pressure to a point where magnetic ring-exchange processes become relevant.

$C_{36}H_{48}Cu_2F_6N_8O_{12}S_2$ - TK91

$C_{36}H_{48}Cu_2F_6N_8O_{12}S_2$ - TK91 presents a good realization of a 2D coupled spin-dimer system. TK91 is a metal organic compound where the Cu^{2+} ions in distorted octahedral

coordination geometry are bridged by the hydroquinone linker to form dimers. The dimer is connected by hydrogen bonds with the neighboring dimer. DC magnetic susceptibility data point out an *intra*-dimer interaction of $J/k_B = 9.4(2)$K. The isothermal magnetization showed that this spin system cannot be properly described with the isolated dimer model. Concomitantly theoretical *ab inito* calculations reveal that TK91 is a 2D-coupled dimer system with *intra*-dimer interaction $J_1/k_B \sim 13.4$K and weak *inter*-dimer interactions of $J_1/k_B = 1.7$K and $J_2/k_B = 1.4$K. At the same time the low-temperature specific heat measurements in magnetic fields $B \geq 4$T revealed significant deviations from isolated-dimer behaviour. In order to check whether TK91 undergoes a field-induced transition at all, the *ac*-magnetic susceptibility was measured as a function of field at various temperatures down to 0.05K. No hysteresis was found upon increasing and decreasing the field, at $T \geq 0.2$K. The data reveal a single broad peak around $B = 6.2$T. For $T \leq 0.2$K the peak narrows and two sharp features appear on its low- and high-field side. These maxima were assigned to the lower and upper boundary of a new field-induced state. The lower-field feature indicates the field (B_{c1}) where the spin gap closes, while the high-field feature marks the field (B_{c2}) where the system enters the fully polarized state. From these data the critical fields at 0K are estimated to be $B_{c1} = 5.9$T and $B_{c2} = 6.5$T, respectively.

Quantum Monte Carlo calculations reveal that the system can be well described with the 2D Heisenberg model of weakly interacting dimers. The low-temperature phase diagram of TK91, in the 50mK $< T <$ 120mK indicates that the new state of the system can be described as a collectively-coupled 2D dimer state, a state where vortices and antivortices start to emerge. Below 50mK the system enters into a state of Berezinskii-Kosterlitz-Thouless topological order, a state where the vortices-antivortices pairs are formed. To our knowledge TK91 is the first bulk magnetic material showing the evidence for a BKT-transition.

These discoveries need to be confirmed with other experimental methods. To achieve this goal, the next steps would be high-resolution specific heat measurements as well as the magnetocaloric effect (MCE) measurements in the low-temperature region $T < 150$mK.

Cu(ox)(pyOH)·H₂O

To the best of our knowledge Cu(ox)(pyOH)·H_2O is the first example of a metal-oxalate chain with an alternating arrangement of oxalate bridge molecules, 'coplanar' and 'parallel' topologies along the chain. Due to such specific structural properties, Cu(ox)(pyOH)·H_2O belongs to the group of strongly dimerized spin-chain compounds or alternating spin chain compounds with $J_1 = (442 \pm 5)$K and $\alpha = 0.13 \pm 0.06$. To our knowledge this compound is the first Cu^{2+}-based polymeric oxalate chain with such a strong antiferromagnetic interaction.

[Cu(μ-C$_2$O$_4$)(4-aminopyridine)$_2$(H$_2$O)]$_n$

[Cu(μ-C$_2$O$_4$)(4-aminopyridine)$_2$(H$_2$O)]$_n$ is a good realization of the uniform $S = \frac{1}{2}$ AFHC. This 1D compound is the first example of a transition metal polymeric structure in which the oxalate molecule bridges the metal ions through one oxygen atom only while the second one remains free. Due to such an unusual configuration of the oxalate bridge in the [Cu(μ-ox)(H$_2$O)(4-apy)$_2$]$_n$ polymer formation, the moderate antiferromagnetic exchange interaction $J/k_B = 3.2(1)$K between the Cu^{2+} ions within the chain was enabled. A moderate saturation field of $B_s = 4.1$T enabled the study of the quantum critical behavior of the spin $S = \frac{1}{2}$ antiferromagnetic Heisenberg chain. Using the magnetic field as an external tuning parameter, the system was driven to a quantum critical point (QCP) and the proposed divergence of the magnetocaloric effect (MCE) at the B-induced QCP was observed. This was the first experimental demonstration of the critical behaviour of the MCE of uniform $S = \frac{1}{2}$ AFHC. The MCE measurements, together with all previous studies (*dc*-susceptibility, *ac*-susceptibility, isothermal magnetization, ESR and specific heat), demonstrated that [Cu(*μ*-ox)(H$_2$O)(4-apy)$_2$]$_n$ is a good model system for a uniform $S = \frac{1}{2}$ AFHC.

It remains to be seen by high-resolution *ac*-susceptibility measurements in zero field whether or not the logarithmic singularity can be resolved for T $\rightarrow$ 0K. The existence of Dzyaloshinskii-Moriya interaction remains to be proven as well.

References

[1]   Edward P.Furlani, *Permanent Magnet and Electromechanical Devices: Materials, Analysis and Applications*, (Academic Press, 2001, pp. ISBN 0-12-269951-3).

[2]   David J.Griffiths, *Introduction to Electrodynamics*, (Prentice Hall, 1998, pp. ISBN 0-13-805326-X).

[3]   Helmut Kronmüller, *Handbook of Magnetism and Advanced Magnetic Materials*, (John Wiley & Sons., 2007, ISBN 978-0-470-02217-7).

[4]   A. Einstein, On the Electrodynamics of Moving Bodies, June 30, 1905.

[5]   J.S. Miller and A. J. Epstein, *Molecule-Based Magnets Materials*, MRS Bulletin, November 2000.

[6]   M. Tamura, Y. Nakazawa, D. Shiomi, K. Nozawa, Y. Hosokoshi, M. Ishikawa, M.Takahshi, M. Kinoshita, Chem. Phys. Lett . **186**, 401 (1991).

[7]   A. Caneschi, D. Gatteschi, R. Sessoli, P. Rey, Acc. Chem. Res. **22**, 392 (1989).

[8]   S. Ferlay, T. Mallah, R. Ouahès, P. Veillet, M. Verdaguer, Nature **378**, 701 (1995).

[9]   J. S. Miller, A. J. Epstein. W. M. Reiff, Chem. Rev. **88**, 201 (1988).

[10]   H. H. Wickman, A. M. Trozzolo, H. J. Williams, G. W. Hull, F. R. Merritt, Phys. Rev. **155**, 563 (1967).

[11]   H. H. Wickman, A. M. Trozzolo, H. J. Williams, G. W. Hull, F. R. Merritt, Phys. Rev. **163**, 526 (1967).

[12]   K. A. Müller, J. G. Bednorz, Z. Phys. B **64**, 189 (1986).

[13]   P. G. de Gennes, *Superconductivity of metals and alloys*, Addison-Wesley, 1989.

[14]   P. Day and A. E. Underhill, Phil. Trans. R. Soc. Lond. A **357**, 2851 (1999).

[15]   P. M. Lahti, *Magnetic Properties of Organic Materials*, Dekker New York, 1999.

[16]   J.S. Miller and M. Drillon M, *Magnetism: Molecules to Materials*, Wiley-VCH Weinheim vol. 1-3, 2001.

[17]   B. Wolf, A. Brühl, V. Pashchenko, K. Remović-Langer, T. Kretz, G. Margraf, H.-W. Lerner, M.Wagner, A.Salguero, T. Saha-Dasgupta, B. Rahaman, R. Valenti, and M. Lang, Comptes Rendus Chimie **10**, 109 (2007).

[18]   T. Kretz, J. W. Bats, S. Losi, B. Wolf, H.-W. Lerner, M. Lang, P. Zanello and M. Wagner, Dalton Trans., 4914 (2006).

References

[19] W. Fitzgerald, J. Foley, D. McSweeney, N. Ray, D. Sheahan, S. Tyagi, J. Chem. Soc., Dalton Trans. 1117 (1982).

[20] J. Cano, P. Alemany, S. Alvarez, M. Verdaguer, E. Ruiz, Chem. Eur. J. **4**, 476 (1998).

[21] M.-Y. Chow, Z.-Y. Zhou and T. C. W. Mak, Inorg. Chem. **31**, 4900 (1992).

[22] J. Schreuer and S. Haussühl, Z. Kristallogr. **205**, 313 (1993).

[23] Y.-X. Tong, X.-M. Chen, S. W. Ng, Polyhedron **16**, 3363 (1997).

[24] Y. R. Wu , L. S. Long , R. B. Huang , L. S. Zheng and S. W. Ng, Acta Crystallogr. E **59,** 390 (2003).

[25] G. Q. Bian, T. Kuroda-Sowa, S. Sugimoto, M. Maekawa and M. Munakata, Acta Crystallogr. C **61**, 144 (2005).

[26] I. A. Zaliznyak, C. Broholm, M. Kibune, M. Nohara, H. Takagi, Phys. Rev. Lett. **83**, 5370 (1999).

[27] N. Motoyama, N. Eisaki, S. Uchida, Phys. Rev. Lett. **76**, 3212 (1996).

[28] M. Takigawa, N. Motoyama, H. Eisaki, S. Uchida, Phys. Rev. Lett. **76**, 4612 (1996).

[29] S. E. Nagler, D. A. Tennant, R. A. Cowley, T. G. Perring, S. K. Satija, Phys. Rev. B **44**, 12361 (1991).

[30] D. A. Tennant, R. A. Cowley, S. E. Nagler, A. M. Tsvelik, Phys. Rev. B **52**, 13368 (1995).

[31] B. Lake, D. A. Tennant, S. E. Nagler, Phys. Rev. Lett. **85**, 832 (2000).

[32] R. Coldea, D. A. Tennant, R. A. Cowley, D. F. McMorrow, B. Dorner, Z. Tylczynski, Phys. Rev. Lett. **79**, 151 (1997).

[33] P. R. Hammar, M. B. Stone, D. H. Reich, C. Broholm, P. J. Gibson, M. M. Turnball, C. P. Landee, M. Oshikawa, Phys. Rev. B **59**, 1008 (1999).

[34] D. C. Dender, D. Davidovic, D. H. Reich, C. Broholm, K. Lefmann, G. Aeppli, Phys. Rev. B **53**, 2583 (1996).

[35] M. B. Stone, D. H. Reich, C. Broholm, K. Lefmann, C. Rischel, C. P. Landee, M. M. Turnbull, Phys. Rev. Lett. **91**, 037205 (2003).

[36] G. Müller, H. Thomas, H. Beck, J. C. Bonner, Phys. Rev. B **24**, 1429 (1981).

[37] T. Andrews, Phil. Trans. R. Soc. **159**, 575 (1869).

[38] P. Curie, Ann. Chim. Phys. **5**, 289 (1895).

[39] L. D. Landau, Phys. Z. Sowjetunion **11**, 26 (1937).

R e f e r e n c e s

[40]   L. Onsager, Phys. Rev. **65**, 117 (1944).

[41]   E. A. Guggenheim, J. Chem. Phys. **13**, 253 (1945).

[42]   M. E. Fisher, J. Math. Phys. **4**, 278 (1963).

[43]   L. P. Kadanoff, Physics **2**, 263 (1966).

[44]   K. G. Wilson, Phys. Rev. B **4**, 3174 (1971).

[45]   K. G. Wilson, Phys. Rev. B **4**, 3184 (1971).

[46]   K. G. Wilson, J. Kogut, Phys. Rep. **12**, 77 (1974).

[47]   S. Sachdev, Nature Physics **4,** 173 (2008).

[48]   T. Giamarchi,C. Rüegg, and O. Tchernyshyov, Nature Physics **4,** 198 (2008).

[49]   S. E. Sebastian, N. Harrison, C. D. Batista, L. Balicas, M. Jaime, P. A. Sharma, N. Kawashima, I. R. Fisher, Nature **441**, 617 (2006).

[50]   K. Kodama, M. Takigawa, M. Horvatic, C. Berthier, H. Kagayama, Y. Ueda, S.Miyahara, F. Becca, F. Mila, Science **298**, 395 (2002).

[51]   T. Matsubara, H, Matsuda, Prog. Theor. Phys. **16**, 569 (1956).

[52]   I. Affleck, Phys. Rev. B **43**, 3215 (1991).

[53]   T. Giarmarchi, A.M. Tsvelik, Phys. Rev. B **59**, 11398 (1999).

[54]   T. Nikuni, M. Oshikawa, A. Oosawa, H. Tanaka, Phys. Rev. Lett. 84, 5868 (2000).

[55]   M. Jaime, V. F. Correa, N. Harrison, C. D. Batista, N. Kawashima, Y. Kazuma, G. A. Jorge, R. Stern, I. Heinmaa, S. A. Zvyagin, Y. Sasago, K. Uchinokura, Rev. Lett. **93**, 87203 (2004).

[56]   S. E. Sebastian, P. A. Sharma, M. Jaime, N. Harrison, V. F. Correa, L. Balicas, N. Kawashima, C. D. Batista, I. R. Fisher, Phys. Rev. B **72**, 100404(R) (2005).

[57]   R. Coldea, D. A. Tennant, K. Habicht, P. Smeibidl, C. Wolters, Z. Tylczynski, Phys. Rev. Lett. **88**, 137203 (2002).

[58]   T. Radu, H. Wilhelm, V. Yushankhai, D. Kovrizhin, R. Coldea, Z. Tylczynski, T. Lühmann, F. Steglich, Phys. Rev. Lett. **95**, 127202 (2005).

[59]   T. Ono, H. Tanaka, H. Aruga Katori, F. Ishikawa, H. Mitamura, T. Goto, Phys. Rev. B **67**, 104431 (2003).

[60]   N. D. Mermin and H. Wagner, Phys. Rev. Lett. **17**, 1133 (1966).

[61]   V. L. Berezinskii, Sov. Phys. JETP **34**, 610 (1972).

[62]   J. M. Kosterlitz, D. J. Thouless, J. Phys. C: Solid State Phys. **5**, L124 (1972).

References

[63] J. M. Kosterlitz, D. J. Thouless, J. Phys. C: Solid State Phys. **6,** 1181 (1973).

[64] D. J. Bishop, J. D. Reppy, Phys. Rev. Lett. **40,** 1727 (1978).

[65] D. J. Resnick, J. C. Garland, J. T. Boyd, S. Shoemaker, R. S. Newrock, Phys. Rev. Lett. **47**, 1542 (1981).

[66] A. I. Safonov, S. A. Vasilyev, I. S. Yasnikov, I. I. Lukashevich, S. Jaakkola, Phys. Rev. Lett. **81,** 4545 (1998).

[67] K. Zahn, R. Lenke, G. Maret, Phys. Rev. Lett. **82**, 2721 (1999).

[68] N. Reyren, S. Thiel, A. D. Caviglia, L. Fitting Kourkoutis, G. Hammerl, C. Richter, C. W. Schneider, T. Kopp, A.-S. Rüetschi, D. Jaccard, M. Gabay, D. A. Muller, J.-M. Triscone, J. Mannhart, Science **317,** 1196 (2007).

[69] Z. Hadzibabic, P. Krüger, M. Cheneau, B. Battelier, J. Dalibard, Nature **441,** 1118 (2006).

[70] A. Cuccoli, T. Roscilde, R. Vaia, P. Verrucchi, Phys. Rev. Lett. **90,** 167205 (2003).

[71] M. Heinrich, H.-A. Krug von Nidda, A. Loidl, N. Rogado, R. J. Cava, Phys. Rev. Lett. **91,** 137601 (2003).

[72] P. Day, Science **261**, 431 (1993).

[73] B. Bleany, K. D. Bowers, Proc. R. Soc. London Ser. A 214, (1952).

[74] T. Holstein and H. Primakoff. Phys. Rev. **58**, 1098 (1940).

[75] F. J. Dyson. Phys. Rev. **102**, 1217 (1956).

[76] S. Coleman in New Phenomena in Subnuclear Physics, Proc. 13th International School of Subnuclear Physics, Erice, ed. A. Zichichi (Plenum Press, NY, 1977) 297.

[77] J. Kosterlitz, J. Phys. C **7**, 1046 (1974).

[78] K. Harada and N. Kawashima, Phys. Rev. B **55,** R11949 (1997).

[79] M. Troyer and S. Sachdev, Phys. Rev. Lett. **81**, 5418 (1998).

[80] G. Schmid, S. Todo, M. Troyer, and A. Dorneich, Phys. Rev. Lett. **88**, 167208 (2002).

[81] L. J. De Jongh, A. R. Miedema, Adv. Phys. **23**, 1 (1974).

[82] A. Cuccoli, T. Roscilde, R. Vaia, P. Verrucchi, Phys. Rev. B **68,** 060402(R) (2003).

[83] D. R. Nelson and J. Kosterlitz, Phys. Rev. Lett. **39**, 1201 (1977).

[84] E. L. Pollock and D. M. Ceperley, Phys. Rev. B **36**, 8343 (1987).

[85] K. Harada and N. Kawashima, Phys. Rev. B **55,** R11949 (1997).

[86] H. T. Diep, *Magnetic System with Competing Interactions*, (World Scientific, Singapore, 1994).

125

References

[87] H. Kawamura, M.S. Li, Phys. Rev. Lett. **78**, 1556 (1997).

[88] B. Müller, J. Reinhardt, M. T. Strickland, *Neural Networks*, (Springer-Verlag, Berlin, 1995).

[89] A. Honecker, J. Schulenburg, J. Richter, J. Phys.: Condens. Matter **16**, S749 (2004).

[90] K. Maisinger, U. Schollwöck, Phys. Rev. Lett. **81**, 445 (1998).

[91] P. Schiffer, Comments Con. Mat. Phys. **18**, 21 (1996).

[92] J. Villain, J. Phys. C **10**, 1717 (1977).

[93] J. Vannimenus, G. Toulouse, J. Phys. C **10**, L537 (1977).

[94] E. W. Hartfield, W. E. Estes, W. E. Marsh, M. W. Pickens, L. W. Ter Haar, R. R. Weller, *Extended Linear Chain Compounds*, (Plenum Press, New York, 1983).

[95] O. Kahn, *Molecular Magnetism*, (VCH Publishers, New York, 1993).

[96] H. A. Bethe, Z. Physik. **71**, 205 (1931).

[97] J. C. Bonner, M. E. Fisher, Phys. Rev. A **135**, 640 (1964).

[98] C. Y. Weng, PhD Thesis, Carnegie-Mellon University, U.S.A., (1968).

[99] H. W. Blöte. Physica B **79**, 427 (1975).

[100] W. Duffy, K. P. Barr, Phys.Rev. **165**, 647 (1968).

[101] M. Takahashi, Prog. Theor. Phys. **46**, 401 (1971).

[102] M. Takahashi, Prog. Theor. Phys. **50**, 1519 (1973).

[103] M. Suzuki, M. Inoue, Prog. Theor. Phys. **78**, 787 (1987).

[104] S. Eggert, I. Affleck, M. Takahashi, Phys. Rev. Lett. **73**, 332 (1994).

[105] S. Lukyanov, Nucl. Phys. B **522**, 533 (1998).

[106] A. Klümper, Eur. Phys. J. B **5**, 677 (1998).

[107] D. C. Johnston, R. K. Kremer, M. Troyer, X. Wang, A. Klümper, S. L. Bud'ko, A. F. Panchula, P. C. Canfield, Phys. Rev. B **61**, 9558 (2000).

[108] Anja U. B. Wolter, PhD Thesis, Braunschweig, Germany, (2005).

[109] R. Feyerherm, S. Abens, D. Günther, T. Ishida, M. Meißner, M. Meschke, T. Nogami, M. Steiner, J. Phys.: Condens. Matter **12**, 8495 (2000).

[110] H. W. J. Blöte, J. L. Cardy, M. P. Nightingale, Phys. Rev. Lett. **56**, 742 (1986).

[111] I. Affleck, Phys. Rev. Lett. **56**, 746 (1986).

References

[112] P. R. Hammar, M. B. Stone, Daniel H. Reich, C. Broholm, P. J. Gibson, M. M. Turnbull, C. P. Landee, M. Oshikawa, Phys. Rev. B **59**, 1008 (1999).

[113] A. Klümper, D.C. Johnston, Phys. Rev. Lett. **84**, 4701 (2000).

[114] M. Cyrot, *Magnetism of Metals and Alloys*, (Amsterdam, 1982).

[115] A. M. Tishin, *Magnetocaloric effect in the vicinity of phase transitions*, (Elsevier, Amsterdam, 1999).

[116] M. E. Zhitomirsky. Phys. Rev. B **67**, 104421 (2003).

[117] L. Zhu, M. Garst, A. Rosch, Q. Si, Phys. Rev. Lett. **91**, 066404 (2003).

[118] M. Garst, A. Rosch, Phys. Rev. B **72**, 205129 (2005).

[119] O. V. Lounasmaa, *Experimental Principles and Methods Below 1 K*, (Academic, London, 1974).

[120] V. K. Pecharsky, K. A. Gschneidner. Phys. Rev. Lett. **78**, 4494 (1997).

[121] O. Tegus, E. Brück,K. H. J. Buschow, F. R. de Boer, Nature **415**, 150 (2002).

[122] M. E. Zhitomirsky, A. Honecker. J. Stat. Mech.: Theor. Exp. P07012 (2003).

[123] M. Takahashi, *Thermodynamics of One-dimensional Solvable Models*, (University Press, Cambridge, 1999).

[124] G. I. Dzhaparidze, A. A. Nersesyan, JETP Lett. **27**, 334 (1978).

[125] V. L. Pokrovsky, A. L. Talapov. Phys. Rev. Lett. **42**, 65 (1979).

[126] S. Sachdev, T. Senthil, R. Shankar, Phys. Rev. B **50**, 258 (1994).

[127] T. Barnes, J. Riera and D. A. Tennant, Phys. Rev. B **59**, 11384 (1999).

[128] S. Sachdev, *Quantum Phase Transitions*, (Cambridge University Press, Cambridge, 1999).

[129] D. Bitko, T. F. Rosenbaum, G. Aeppli, Phys. Rev. Lett. **77**. 940 (1996).

[130] P. Coleman, Physica B **259–261**, 353 (1999).

[131] H. von Löhneysen, J. Phys. Condens. Matter **8**, 9689 (1996).

[132] E. Dagotto, Rev. Mod. Phys. **66**, 763 (1994).

[133] S. Sachdev, Science **288**, 475 (2000).

[134] S. V. Kravchenko, W. E. Mason, G. E. Bowker, J. E. Furneaux, V. M. Pudalov and M. D'Iorio, Phys. Rev. B **51**, 7038, (1995).

[135] N. F. Mott, *Metal–Insulator Transitions*, (Taylor and Francis, London, 1990).

References

[136] MPMS XL Options Manual (1999).

[137] P. Gegenwart, Dipl. Thesis, TH Darmstadt, Germany, (1994).

[138] P. Hinze, PhD Thesis, TH Darmstadt, Germany, (2002).

[139] P. Hinze, Diplom Thesis, TH Darmstadt, Germany, (1998).

[140] G. R. Stewart, Rev. Sci. Instrum. **54**, 1 (1983).

[141] S. Schmidt, PhD Thesis, J. W. Goethe-Universität, Frankfurt am Main, Germany, (2001).

[142] Keith J. Laider, *The World of Physical Chemistry*, (Oxford University Press, Oxford, 1993).

[143] H. Wilhelm, T. Lühmann, T. Rus, F. A. Steglich, Rev. Sci. Instrum. **75**, 2700-2705 (2004).

[144] M. Ramos Silva, J. A. Paixao, A. Matos Beja, L. Alte da Veiga, J. Martın-Gil, J. Chem. Crystallogr. **31**, 167 (2001).

[145] J. Albers, A. Klöpperpieper, H. J. Rother and K. H. Ehses, Phys. Status Solidi (a) **74**, 553 (1982).

[146] H.-G. Unruh, F. Hero, V. Dvorak, Solid State Communic. **70**, 403 (1989).

[147] M. R. Chaves, A. Almeida, J. C. Toledano, J. Schneck, J. M. Kiat, W. Schwarz, J. L. Ribeiro, A. Klöpperpieper, J. Albers, H. E. Müser, Phys. Rev. B **48**, 13318 (1993).

[148] X.-M. Chen and Th. C. W. Mak. Inorg. Chim. Acta **189**, 3 (1991).

[149] J. Schreuer and S. Haussühl, Z. Kristallogr. **205**, 309 (1993).

[150] L. Wiehl, J. Schreuer, E. Haussühl, Z. Kristallogr. NCS **221**, 77 (2006).

[151] L. Wiehl, J. Schreuer, E. Haussühl, B. Winkler, K. Remović-Langer, B. Wolf, M. Lang, V. Milman, J. Phys.: Condens. Matter. **18**, 11067 (2006).

[152] A. F. Wells, *Structural Inorganic Chemistry*, (Oxford, 1984).

[153] W. Hiller, J. Strähle, A. Datz, M. Hanack, W. E. Hartfield, P. Gütlich, J. Am. Chem. Soc. **106**, 329 (1984).

[154] J. S. Smart, *Effective Field Theories of Magnetism*, (Saunders, Philadelphia, 1966).

[155] T. Oguchi, Phys. Rev. **133**, A1098 (1964).

[156] H. Lueken, *Magnetochemie*, (Teubner Verlag, Stuttgart/Leipzig, 1999).

[157] S. Mukhopadhyay, D. Mandal, P. B. Chatterjee, C. Desplanches, J. P. Sutter, R. J. Butcher, M. Chauhdury, Inorg. Chem. **43**, 8501 (2004).

References

[158] M. R. Bond, R. D. Willett, R. S. Rubins, P. Zhou, C. E. Zaspel, S. L. Hutton, J. E. Drumheller, Phys. Rev. B **42**, 10280 (1990).

[159] C. E. Zaspel, G. V. Rubenacker, S. L. Hutton, J. E. Drumheller, R. S. Rubins, R. D. Willett and M. R. Bond, J. Appl. Phys. **63**, 3028 (1988).

[160] V. Pashchenko, B. Brendel, B. Wolf, M. Lang, K. Lyssenko, O. Shchegolikhina, Y. Molodtsova, L. Zherlitsyna, N. Auner, F. Schütz, M. Kollar, P. Kopietz and N. Harrison, Eur. J. Inorg. Chem. **4617** (2005).

[161] K. Remović-Langer, L. Wiehl, B. Wolf, N. Hasselmann, F. Sauli, P. Kopietz, M. Lang, J. Phys.: Condensed Matter **21**, 185013 (2009).

[162] H. J. Schmidt, Y. Kuramoto, Physica C **167**, 263 (1990).

[163] A. Chubukov, E. Gagliano, C. Balseiro, Phys. Rev. B **45**, 7889 (1992).

[164] F. Romero, R. Ziessel, M. Bonnet, Y. Pontillou, E. Ressouche, J. Schweizer, B. Delley, A. Grand, C. Paulsen, J. Am. Chem. Soc. **122**, 1298 (2000).

[165] C. Rancurel, N. Daro, O. B. Borobia, E. Herdtweck, J. P. Sutter, Eur. J. Org. Chem. 167 (2003).

[166] A. Oosawa, M. Ishii, H. Tanaka, J. Phys. Condens. Matter **11**, 265 (1999).

[167] G. Margraf, T. Kretz, F. Fabrizi de Biani, F. Laschi, S. Losi, P. Zanello, J.W. Bats, B. Wolf, K. Remović-Langer, M. Lang, A. Prokofev, W. Assmus, H.-W. Lerner, and M. Wagner, Inorg.Chem. **45**, 1277 (2006).

[168] Y. Tsui, A. Brühl, K. Remović-Langer, V. Pashchenko, B. Wolf, T. Kretz, G. Margraf, H.-W. Lerner, M. Wagner, A. Salguero, T. Saha-Dasgupta, B. Rahaman, R. Valenti, M. Lang, J. Magn. Magn. Mat. **310**, 1319 (2007).

[169] O. K. Andersen. Phys. Rev. Lett. **12**, 3060 (1975).

[170] O. K. Andersen, T. Saha-Dasgupta, Phys. Rev. B **62**, R16219 (2000).

[171] U. Tutsch, B. Wolf, Y. Tsui, S. Wessel, H. Jeschke, T. Saha-Dasgupta, R. Valenti, A. Brühl, K. Remović-Langer, T. Kretz, H.-W. Lerner, M. Wagner and M. Lang, submitted to Nature Materials 2009.

[172] J. H. Van Vleck, Phys. Rev. **74**, 1168 (1948).

[173] O. Nohadani, S. Wessel and S. Haas, Phys. Rev. B **72**, 024440 (2005).

[174] K. Goto, M. Fujisawa, T. Ono, H. Tanaka, Y. Uwatoko, J. Phys. Soc. Japan **73**, 3254 (2004).

[175] Sengupta, P. *et al.*, Phys. Rev. B **79,** 060409(R) (2009).

[176] M. Tachiki, T. Yamada. J. Phys. Soc. Jpn. **28**, 1413 (1970).

References

[177] H. Weber, P. Minnhagen, Phys. Rev. B **37,** 5986–5989 (1987).

[178] O. Castillo, A. Luque, M. Julve, F. Lloret, P. Roman, Inorg. Chim. Acta **315**, 9 (2001).

[179] O. Castillo, A. Luque, F. Lloret and P. Roman, Inorganica Chimica Acta **324**, 141 (2001).

[180] O. Castillo, A. Luque, P. Roman, F. Lloret and M. Julve, Inorg. Chem. **40**, 5526 (2001).

[181] O. Castillo, A. Luque, J. Sertucha, P. Roman, F. Lloret, Inorg. Chem. **39**, 6142 (2000).

[182] U. Garcia-Couceiro, O. Castillo, A. Luque, G. Beobide, P. Roman, Inorg. Chim. Acta **357**, 339 (2004).

[183] J. Cabrero, N. Ben Amor, C. de Graaf, F. Illas, R. Caballol, J. Phys. Chem. A **104**, 9983 (2000).

[184] M. F. Ottavianim, F. Montalti, N. J. Turro and D. A. Tomalia, Phys. Chem. B **101**, 158 (1997).

[185] M. Julve, M. Verdaguer, O. Kahn, A. Gleizes, O. Philoche-Levisalles, Inorg. Chem. **23**, 3808 (1984).

[186] J. Glerup, P. A. Goodson, D. J. Hodgson, K. Michelsen, Inorg. Chem. **34**, 6255 (1995).

[187] P. Roman, C. Guzman-Miralles, A. Luque, J. I. Beitia, J. Cano, F. Loret, M. Julve, S. Alvarez, Inorg. Chem. **35**, 3741 (1996).

[188] A. Michalowicz, J. J. Gired, J. Goulson, Inorg. Chem. **18**, 3004 (1979).

[189] L. Cavalca, A. Chiesi-Villa, A. Manfredotti, A. Mangia, A. A. G. Tomlinson, J. Chem. Soc., Dalton Trans. 391 (1972).

[190] J. J. Girerd, O. Khan, M. Verdaguer, Inorg. Chem. **19**, 274 (1980).

[191] S. Kitagawa, T. Okubo, S. Kawata, M. Kondo, M. Katada, H. Kobayashi, Inorg. Chem. **34**, 4790 (1995).

[192] H. Oshio, U. Nagashima, Inorg. Chem. **31**, 3295 (1992).

[193] J. Suarez-Varela, J. M. Domınguez-Vera, E. Colacio, J. C. Avila-Roson, M. A. Hidalgo, D. Martın-Ramos, J. Chem. Soc., Dalton Trans. 2143 (1995).

[194] U. Geiser, B. L. Ramakrishna, R. D. Willett, F. B. Hulsbergen, J. Reedijk, Inorg. Chem. **26**, 3750 (1987).

[195] R. Andres, M. Gruselle, B. Malezieux, M. Verdaguer, J. Vaissermann, Inorg. Chem. **38**, 4637 (1999).

References

[196] M. Hernandez-Molina, F. Lloret, C. Ruiz-Perez, M. Julve, Inorg. Chem. **37**, 4131 (1998).

[197] A. V. Prokofiev, W. Assmus, K. Remović-Langer, V. Pashchenko, Y. Tsui, B. Wolf, M. Lang, Cryst. Res. Technol. **42**, No. 4, 394 (2007).

[198] J. Sertucha, A. Lugue, O. Castillo, P. Román, F. Lloret, M. Julve, Inorg. Chem. Commun. **2**, 14 (1999).

[199] D. C. Dender, D. Davidovic, D. H. Reich, C. Broholm and G. Aeppli, Phys. Rev. Lett. **79**, 1750 (1997).

[200] G. Mennenga, L. J. de Jongh, W. J. Huiskamp and J. Reedijk, J. Magn. Magn. Mater. **44**, 89 (1984).

List of Publications originating from this PhD thesis:

1. Y. Tsui, B. Wolf, D. Jaiswal-Nagar, U. Tutsch, A. Honecker, K. Remović-Langer, G.Hofmann, A. Prokofiev, W. Assmus, G. Donath, and M. Lang, **Supplementary Information for "Magnetocaloric effect and magnetic cooling near a field-induced quantum-critical point"**, (submitted to Nature Physics 2009).

2. M. Lang, Y. Tsui, B. Wolf, D. Jaiswal-Nagar, U. Tutsch, A. Honeker, K. Remović-Langer, A. Prokofiev, W. Assmus, G. Donath, **Large magnetocaloric effect at the saturation field of an S = ½ antiferromagnetic Heisenberg chain**, J. Low Temp Phys **159**, 88-91 (2010).

3. B. Wolf, P.T. Cong, K. Remović-Langer, Y.D. Borozdina, E. Mostovich, M. Baumgarten, M. Lang, **Coupled spin S = ½ dimer systems based on nitronyl-nitroxide biradicals**, (submitted to ICM 2009).

4. P.T. Cong, B. Wolf, U. Tutsch, K. Remović-Langer, J. Schreuer, S. Süllow, M. Lang, **Ultrasonic Investigation on the Distorted Diamond Chain Compound Azurite**, (submitted to ICM 2009).

5. U. Tutsch, B. Wolf, Y. Tsui, S. Wessel, H. Jeschke, T. Saha-Dasgupta, R. Valenti, A. Brühl, K. Remović-Langer, T. Kretz, H.-W. Lerner, M. Wagner, M. Lang, **Field-induced Berezinskii-Kosterlitz-Thouless transition in a 2-dimensional spin-dimer system**, (submitted to Nature Materials 2009).

6. K. Remović-Langer, L. Wiehl, B. Wolf, N. Hasselmann, F. Sauli, P. Kopietz, M. Lang, **Magnetic properties of a novel quasi-2D Cu(II)-trimer system**, J. Phys.: Condensed Matter **21** (2009), 185013.

7. K. Remović-Langer, L. Wiehl, V. Pashchenko, B. Wolf, M. Lang, **Cu(ox)(pyOH)•H2O – magnetostructural correlations of the new dimerized spin chain**, J Phys.: Condens. Matter. **20** (2008), 015221.

8. A.V. Prokofiev, W. Assmus, K. Remović-Langer, V. Pashchenko, Y. Tsui, B. Wolf, M. Lang, **Crystal growth and magnetic properties of the copper coordination polymer $[Cu(\mu -C_2O_4)(4\text{-aminopyridine})_2(H_2O)]_n$**, Cryst. Res. Technol. **42** (2007), 394.

9. B. Wolf, A. Brühl, V. Pashchenko, K. Remović-Langer, T. Kretz, J.W. Bats, H.-W. Lerner, M. Wagner, A. Salguero, T. Saha-Dasgupta, B. Rahaman, R. Valenti and M. Lang, **Modified 1,4-hydroquinone ligands bridging Cu(II) ions – Building blocks for a new class of quantum magnets**, Comptes Rendus Chimie **10** (2007), 109.

10. Y. Tsui, A. Brühl, K. Remović-Langer, V. Pashchenko, B. Wolf, G. Donath, A. Pikul, T. Kretz, H.-W. Lerner, M. Wagner, A. Salguero, T. Saha-Dasgupta, B. Rahaman, R. Valenti, M. Lang, **Field-Induced Phase Transition in a Metalorganic Spin-Dimer System – a Potential Model System to Study Bose – Einstein Condensation of Magnons**, J. Mag. Mag. Mat. **310** (2007), 1319.

11. G. Margraf, T. Kretz, F. Fabrizi de Biani, F. Laschi, S. Losi, P. Zanello, J. W. Bats, B. Wolf, K. Remović-Langer, M. Lang , A. Prokofiev, W. Aßmus, H.W. Lerner and M. Wagner, **Mono-, Di-, and Oligonuclear Complexes of Cu(II) Ions and p-Hydroquinone Ligands: Syntheses, Electrochemical Properties and Magnetic Behavior**, Inorg. Chem. **45** (2006), 1277.

12. L. Wiehl, J. Schreuer, E. Haussühl, B. Winkler, K. Remović-Langer, B. Wolf, M. Lang and V. Milman, **Structural and magnetic properties of betaine adducts with transition metals: I. ((CH$_3$)$_3$NCH$_2$COO)$_3$MnMCl$_4$ with M = Mn^{2+}, Co^{2+}, Zn^{2+}**, J. Phys.: Condens. Matter. **18** (2006), 11067.

13. M. Lang, A. Brühl, V. Pashchenko, K. Remović-Langer, Y. Tsui, U. Tutsch, B. Wolf, T. Kretz, W. Lerner, M. Wagner, J. Schreuer, **Exploring antiferromagnetic S = 1/2 dimer systems in high magnetic fields**, J. Phys.: Conference Series **51** (2006), 1.

Talks:

1. Katarina Remović-Langer: **Molecule-based realization of an S = ½ antiferromagnetic Heisenberg chain**, DPG Frühjahrstagung Festkörperphysik, 26.02.2008, Berlin.

2. Katarina Remović-Langer: **Carboxylate bridged 3d-metal chains with Betaine and Oxalate: Structural and Magnetic Properties**, Max-Planck-Institut für Chemische Physik fester Stoffe, Invited Talk 2006, Dresden.

3. Katarina Remović-Langer: **New class of the multifunctional molecular system k-BETS$_2$ FeBr$_4$**, Forschergruppe Projekt 402, 2004, Johann Wolfgang Goethe-Universität.

Acknowledgments

At this place, it is customary, and I will do it from the bottom of my heart, to thank and acknowledge all of you who have, in any and various ways, contributed finishing this thesis. As it is usually the case with the thesis of this type, this is not the work of just one person, but the result of the entire group and a team of people. This thesis is the result of a whole bunch of people eager to new discoveries and pushing back the boundaries of existing science. Certainly it will happen to forget to mention someone, please do not take me for evil, it was not intentionally!

I would like to thank the person deserved for the existence of this thesis, my mentor Prof. Dr. Michael Lang. I want to thank you for the decision and readiness to a woman with a child give the opportunity to make a thesis and work in science at all! Thank You for Your endless patience you have had for correcting my 'scientific' texts. And most of the thanksgiving goes to scientific discussions related to quantum-mechanical phenomena at low-temperature, thanks to its my understanding of low temperature physics and the bunch of interesting quantum phenomena, had got another dimension.

Naturally, special thanks I owe to people who have teach me the main principles of functioning and running of He^3-He^4 dilution cryostat, Dr. Yeekin Tsui, PD Dr. Bernd Wolf and Dr. Peter Hinze. Hey guys, thank you for the patience that you have connected with all my 'bright' questions about the machine and experimental methods. Especially I would like to thank my long-time roommate Yeekin for the patience (staying power) he had for my mood, as well as on interesting scientific discussions related to the BEC and MCE. I would like also to thanks to Dr. Ulrich Tutsch who allowed me to take part on susceptibility measurements of TK91 on top-loading dilution cryostat, as well as on useful discussions connected to BKT transition.

For excellent training on working with SQUID, as well as for all my understanding of the magnetic susceptibility all my thanks going to PD Dr. Bernd Wolf and Dr. Volodymir Pashchenko.

I would like to thank Prof. Dr. Philipp Gegenwart for allowing the specific heat measurements of SP in his group in Dresden and special thanks to the person responsible for the realization of experiments, Guido Donath.

What would be experimental results without an appropriate theoretical background, probably just a bunch of some interesting curves and dots? Thanks to PD Dr. Andreas Honecker and Prof. Dr. Nils Hasselmann calculations and simulations, some of my results obtained confirmation of the validity within the frame of existing theories. Thanks for supplying me so fast with necessary theory.

When finished writing such a text, it is certainly needed to find the eye of an independent observer, who will find and correct all the mistakes that had crept by chance. Here my thoughts lead me to Carolyne Agnew. Apart from this, I thank you for small-talks in break time, on your good mood and cooking and supplying me with the coffee.

Acknowledgments

It would be wrong to forget all technicians and people from workshop. Thanks for giving the necessary support when it was needed.

Without fail I want to thank the rest of group members Christian Strack, Dr. Andreas Brühl, Chemin Akinci, Mehmet Bilgetekin, Dr. V. Pereira Mariano de Souza, Dr. Deepshikha Jaiswal-Nagar, Thanh Cong Pham, Rudra Sekhar Manna without which the life and work in the laboratory over the time would became boring and tiring. Special thanks going to the only one woman in the group Deepshikha.

Many thanks to my friends Ina, Zeljka, Sanja, Buba and Bogdan who had to stand never-ending stories about this work, even if they didn't understand it all. Thank you for being there.

Finally, I would like to thank my family who were all the time with me and supported me during all these years of work, they give me confidence in the moments when everything seemed desperate and pointless, and motivated me to bring this work to an end. Thank you for your warmth and love you gave and have it for me, without it will not be possible to finish this work!

A special thank goes to my husband, who is with full understanding and love endured all horribly tumultuous changes in mood, present during the preparation of this work. Thank you for all your love!

Katarina Remović-Langer, Frankfurt am Main, August 2010

Curriculum Vitae

Personal Data

Name:	Katarina Remović-Langer
Date of birth:	23.10.1970
Place of birth:	Belgrade, Serbia
Nationality:	Serbian

Education and Academics Degrees

1977 – 1985	Primary School Vasa Pelagić, Belgrade
1985 – 1989	High school 3. Belgrade Gymnasium, Belgrade School Leaving certificate (*Abitur*, 1989)
1989 – 1997	Physics Faculty, University of Belgrade, Belgrade Degree in Physics (*Diplom*, 1997) Subject of Diploma Thesis: *„Isostatic Polypropylene Recrystallisation of Different Morphologies"* Supervisor: Prof. Dr. Dušan Kostovski

---

1997 – 2000	Physics Faculty, University of Belgrade, Belgrade
	Degree in Physics (*Master*, 2000)
	Subject of Master Thesis:
	„Atomic Interface Mixing in Ta/Si Bilayers Induced with Ar Ions"
	Supervisor: Dr. Nataša Bibić

Current Positions

1997 – 2000	Research assistant at Institute of Nuclear Sciences - Vinča, Department of Atomic Physics, Belgrade, Serbia
06/2000 – 12/2000	Fellowship at Hahn-Meitner Institute, Department of Magnetism, Berlin, Germany
2000 – 2003	Research assistant at Hahn-Meitner Institute, Department of Magnetism, Berlin, Germany During this time research stays at SSRL/Stanford, Hasylab/Hamburg, Maxlab/Lund, Bessy/Berlin (2 – 4 weeks)
2003 – 2008	Research assistant at Institute of Physics, University Frankfurt, Department of Strongly Correlated Electrons and Spins, Frankfurt am Main, Germany Preparation of the Ph. D. thesis Thesis subject: *„Magnetic characteristics of metal organic low-dimensional quantum spin systems at low temperatures"* Supervisor: Prof. Dr. Michael Lang, University Frankfurt
2009 – 2010	Teacher at High School Carl-Schurz-Schule, Frankfurt am Main, Germany